공학박사 학위논문

# Synthesis of Heteroatom-Modified Carbon Nanomaterials for their Applications to Water Oxidation and Supercapacitor

물 산화 반응 및 슈퍼캐퍼시터 응용을 위한 이종원자로 개질된 탄소 나노물질의 합성

**2018년 8월**

서울대학교 대학원

화학생물공학부

비 나 약

# 인준

## Abstract

# Synthesis of Heteroatom-Modified Carbon Nanomaterials for their Applications to Water Oxidation and Supercapacitor

Vinayak Swamirao Kale

School of Chemical and Biological Engineering

The Graduate School

Seoul National University

Due to their cheap availability, ease in the synthesis and environment benign nature, carbon materials have become a relatively popular research topic compared to metal or metal oxides. Carbon materials with

a variety of different sizes, shapes, and dimensions can be obtained depending on the synthesis conditions. Further, carbon nanomaterials with heteroatoms such as nitrogen, phosphorus, sulfur, and/or boron show significantly enhanced properties and new functionality, charge re-distribution, and/or formation of new energy states. This modification can be achieved either by the process of doping or substitution of heteroatoms in carbon nanomaterials. Moreover, the modification of carbon with more than one heteroatom results in synergistic effects and enhanced properties compared to doping with a single heteroatom. The heteroatom-modified carbon nanomaterials show excellent performance compared to well established metal/metal oxides in many applications. Various synthetic strategies that are developed for heteroatom-modification in carbon nanomaterials are discussed in Introduction, Chapter-1.

Following the Introduction chapter, Chapter-2 describes the synthesis of sulfur-modified graphitic carbon nitride nanostructures. Inspired by natural geodes, unique melamine nanogeodes are synthesized by a hydrothermal process. The *in-situ* mixing and pyrolysis of sulfur with melamine nanogeodes produced sulfur-modified graphitic carbon nitride

(S-modified g-$CN_x$) nanostructures. When applied as a water oxidation electrocatalysts, S-modified g-$CN_x$ has excellent oxygen evolution reaction (OER) activity showing one of the best performance among carbon-based systems, comparable to reported metal/metal oxide, and well-established electrocatalysts. The sulfur modification in the g-$CN_x$ structure lowers the overpotential due to minimization of the activation energy for OER.

In Chapter-3, a wrap-bake-sublime approach for gram-scale synthesis of N, P co-doped hollow carbon nanostructures (NPHC) is presented. Zinc containing zeolitic-imidazole-framework (ZIF-8) nanoparticles are used as a core to be wrapped by N, P containing oligomer of oligo(cyclotriphosphazene-*co*-hexahydroxytriphenylene) (OCHT). Pyrolysis of these ZIF-8@OCHT nanoparticles leads to the sublimation of zinc and introduces porosity in the synthesized NPHC. The microporosity in the NPHC can be finely tuned by changing the thickness of the OCHT shell during the synthesis of ZIF-8@OCHT nanoparticles. These micropore size dependent NPHCs were used as an electrode in supercapacitor and an excellent correlation between the electrochemical performance and the microporosity of NPHCs was

observed. Additionally, the electrochemical performance is correlated with the ratio between the heteroatoms used to dope NPHCs. Finally, a symmetric and flexible all-solid-state-supercapacitor device is assembled and it demonstrated high energy density, power density, and good long-term stability for 20,000 cycles with 75% capacitance retention.

**Keywords: heteroatom, modification, doping, graphitic carbon nitride nanostructures, carbon nanocages, water oxidation, supercapacitor**

**Student number: 2012-31295**

# Contents

# List of Tables



# List of Figures

# Chapter 1. Introduction: Synthesis of Heteroatom-Modified Nanostructured Carbons for Water Oxidation and Supercapacitor Application

## 1.1 Introduction

There is a deep understanding and knowledge of metal and metal oxide syntheses. Hence they are used in a wide range of applications and they became an inevitable part of human life. Although the human population is increasing linearly over time, the metal and metal oxide deposits in the Earth are finite. The increasing demand of metal and metal oxide materials cannot be fulfilled in the near future, so there is strong necessity to find alternative to these systems. Due to their cheap cost, availability, ease in synthesis and environmental benign nature, carbon materials are considered to be a valid alternative to metal and metal oxides.[1-12] Synthesizing carbon materials at nanoscale tremendously modulates their properties.[13-46] Several breakthroughs have been achieved in carbon materials since the discovery of one-dimensional carbon nanotubes by Sumio Iijima in 1991,[47] and the re-discovery of two-dimensional graphene by Andre Geim and Konstantin Novoselov in

2004.[14] Nowadays, the synthesis of carbon nanomaterials is an established practice and is applied in a variety of fields.

Depending on the application, carbon nanomaterials are used either independently or as a composite with other metal/metal.[15,48-51] The intrinsic limitations of carbon nanomaterials in terms of their applications can be solved in many ways, such as increasing the number of active sites by increasing the surface area, choosing proper dimensions, modifying the carbon nanomaterials with other heteroatoms, etc. Incorporating heteroatoms in carbon nanomaterials can be achieved by doping, substitution, alteration or incorporation of nitrogen,[26,30,32,46,52-58] phosphorus,[6,35,46,53,54,59-63] sulfur,[7,36,64-66] boron,[18,63,67-70] oxygen,[26,30] fluorine,[46,68] or iodine.[71,72] In particular, doping of heteroatoms in carbon nanomaterials is widely known and studied. The modification of carbon with heteroatoms significantly can enhances properties due to many reasons such as introduction of new functionality, charge re-distribution and/or formation of new energy state.[32,36,53] These heteroatom-modified carbon nanomaterials show excellent performance compared to well established metal and metal oxides in many applications and are considered to be a potential alternative candidate. Recent important developments of carbon-based catalysts are shown in

Figure 1.1.[32,52,73-84]

As a simple and model system, N-doped carbon nanomaterials have been studied widely and investigated for many applications.[85] There are mainly three kinds of N-containing molecular structures present in N-doped carbon materials: pyrrolic N, pyridinic N, and quaternary N (Figure 1.2a).[84,85] Five-membered heterocyclic rings form pyrrolic N, while six membered cyclic rings form pyridinic N by substitution of a carbon atom. Nitrogen atoms doped inside the graphitic carbon plane form the quaternary N. The positions of quaternary N can be at the edge and/or within the graphene layers while the pyridinic and pyrrolic N can be found at the edge of the graphitic carbon plane. The elevated temperatures during thermal treatment significantly changes the environment of N species and tend to convert pyridinic N to pyrrolic N and quaternary N, which is thermally the most stable. Some reports showed that the contributions of each type of N species is important in many applications and can be controlled during synthesis of carbon nanomaterials.[84,85]

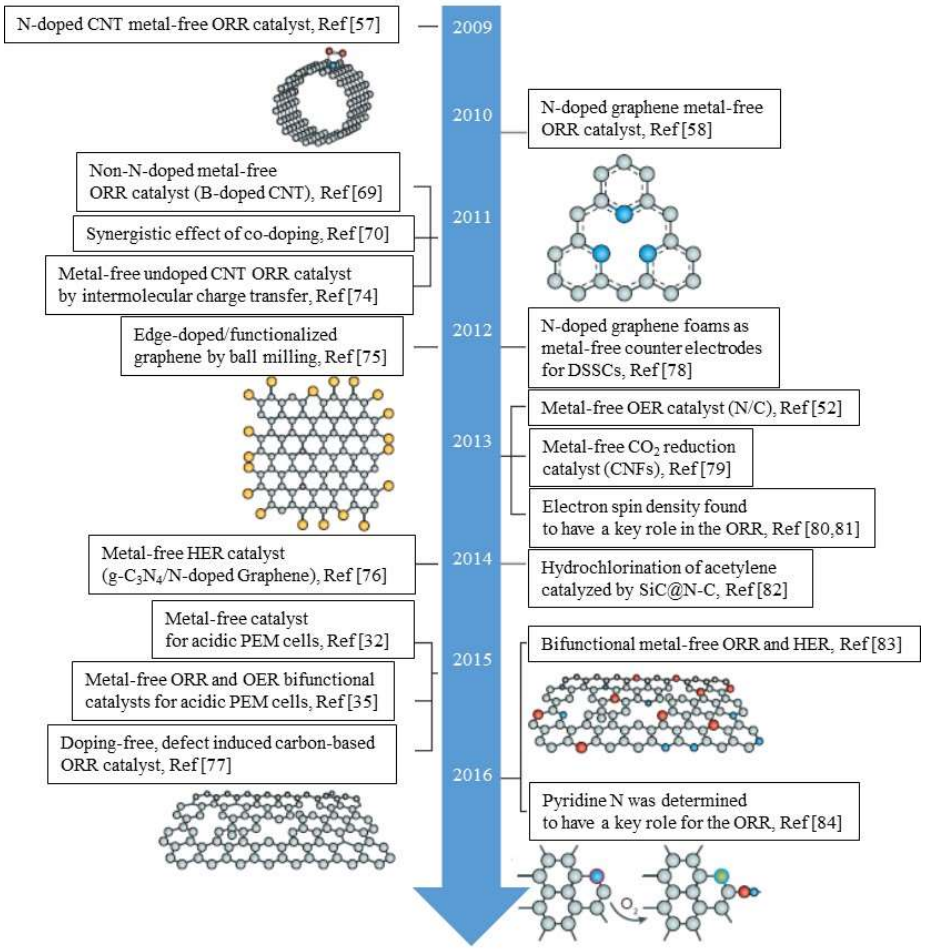


**Figure 1.1** Recent important developments on carbon-based catalysts. The figure is reproduced with permission from Ref. [73], © 2016 The Nature Publishing Group.

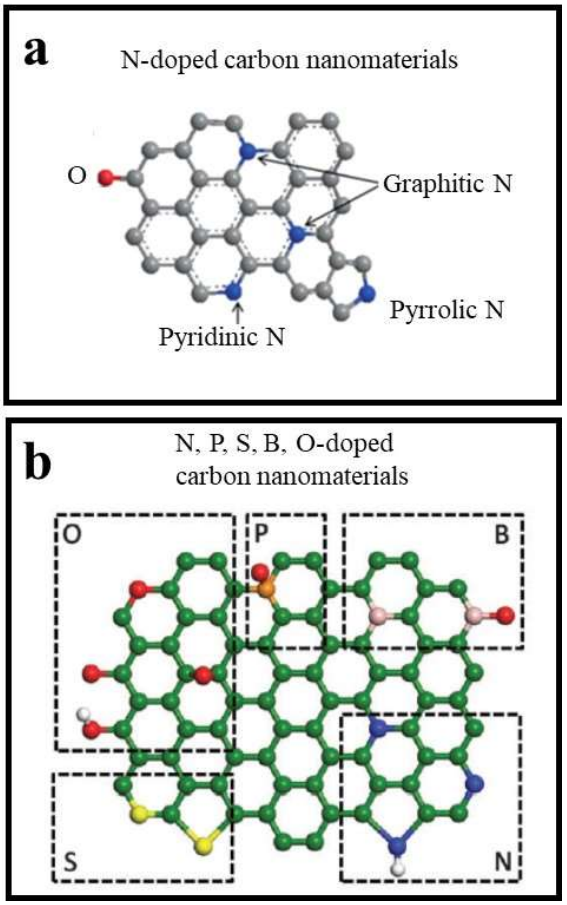


**Figure 1.2** Schematic representation of heteroatom doping sites in carbon. (a) Type of N present in the doped carbon. (b) Typical atomic configuration of N, P, S, B, O at different doping sites in the carbon. These figures are reproduced with permission (a) from Ref. [85], © 2015 Wiley-VCH and (b) from Ref. [86], © 2015 The Royal Society of Chemistry.

Along with N, other heteroatoms such as P, S, B or O are also investigated as dopants in carbon nanomaterials. Typical atomic configuration of N, P, S, B, O at different doping sites in the carbon are shown in Figure 1.2b.[86] These doped heteroatoms have shown similar enhancement in the properties of carbon nanomaterials. Furthermore, incorporating more than one heteroatom in carbon nanomaterials leads to synergistic effects, resulting in carbon with improved properties compared to singularly doped carbon. Some examples of multi-heteroatom modification in carbon nanomaterials include N/P, N/S, N/B, N/P/S, N/S/B, N/P/S/B, P/S, P/B, P/S/B, S/B.[5,46,63] The synthesis of single or more than one heteroatom-modified carbon nanomaterials is still in its infancy and it's of yet unknown whether they can successfully replace traditional metal or metal oxides.

This chapter focuses on the research background and recent advances in the synthesis of heteroatom-modified carbon nanomaterials. In particular, synthesis strategies of N, P, S, or B-modified carbon nanomaterials will be discussed in detail.

## 1.2 Strategies for the Synthesis of Heteroatom-Modified Carbon Nanomaterials in Energy Applications: Research Background

Depending on the synthetic procedures to obtain heteroatom-modified carbon nanomaterials, it can be roughly categorized into three types. The first one, high surface area heteroatom-modified carbon nanomaterials, can be achieved by using hard or soft templates with heteroatom containing precursors.[4,87-89] The high surface area and porosity increases the number of active sites in the carbon. In the second process, pyrolysis of carbon nanomaterials is used, as most of the carbon nanomaterials used in energy applications require enhanced electronic properties. Pyrolysis is a step in which heteroatom(s) can be introduced by making a composite or by combining the carbon precursor with heteroatom source(s).[35,90-92] In the third process, pre-synthesized carbon nanomaterials are subjected to further modification by a number of ways with heteroatom containing precursors.[35] Other synthesis strategies of carbon based catalysts are shown in Figure 1.3.[73] The particular synthetic methods, based on their dimensions and morphology, type of sources, common structural features, etc are as follows.

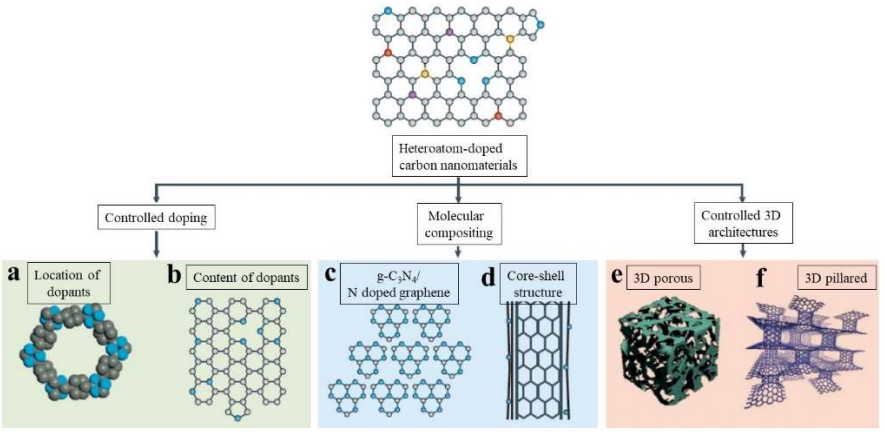


**Figure 1.3** Various synthetic strategies of carbon based catalysts. The figure is reproduced with permission from Ref. [73], © 2016 The Nature Publishing Group.

### 1.2.1 Synthesis of Heteroatom-modified Carbon Nanomaterials with Various Dimensions (0D, 1D, 2D, 3D)

The carbon materials can show morphologies in either zero dimension (graphene quantum dots, fullerene), one dimension (carbon nanotubes), two dimension (graphene oxide, graphene), and three dimension (foams, carbon assemblies like polymer hydrogels). The properties of the carbon nanomaterials are strongly dependent on its dimesions. For example, the zero dimensional (0D) graphene quantum dots (GQDs)[36] show fluorescence properties due to the quantum confinement effect, the one dimensional (1D) carbon nanotubes (CNTs)[26] have excellent electronic conductivity, the two dimensional (2D) graphene[44] has wonderful stability, whereas the three dimensional (3D) carbon assemblies show high surface area with increased electrochemical properties.[35] The properties of the various dimensional carbon nanomaterials can be enhanced by the additional heteroatom-modification depending on the requirements of the particular application. The schematic representation in Figure 1.4 shows single and multi heteroatom doping in carbon nanomaterials with various dimensions.

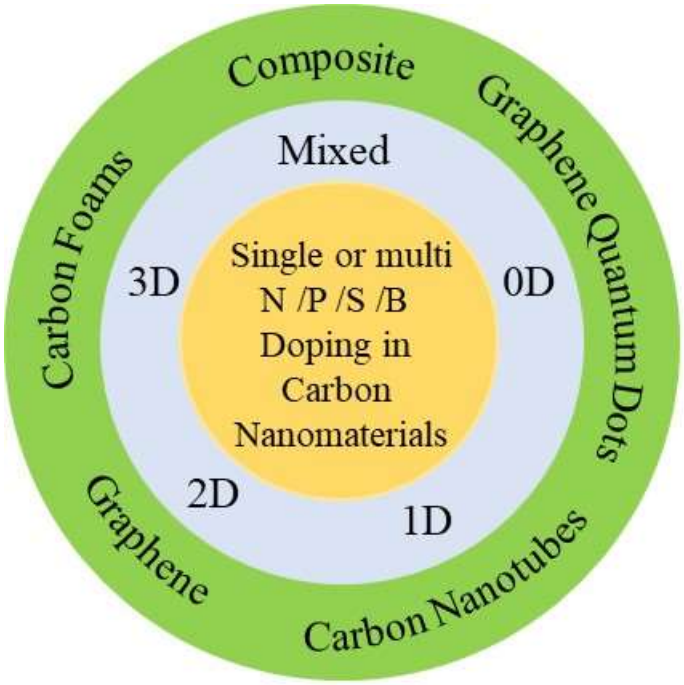


**Figure 1.4** Schematic representation of single or multi heteroatom doping in various dimensions of carbon nanomaterials.

For example, doping of N in 0D carbon nanomaterials produce N-doped GQDs, in 1D carbon nanomaterials produce N-doped CNTs, in 2D carbon nanomaterials produce N-doped graphenes, and in 3D carbon nanomaterials produce N-doped carbon networks, etc. The N-doping significantly alters the properties of these carbon nanomaterials and opens a vast area of research in this field with a lot more interesting applications still to be discovered. Doping with other single or multi heteroatoms of P, S, B has also been studied and found to have a significant role in the enhancement of properties of carbon nanomaterials with different dimensions.

### 1.2.2 Synthesis of Heteroatom Containing Conducting Polymer Gels

Conducting polymer gels (CPGs) are an assembly of conductive polymers with excellent electrical condutivity. These CPGs are easy to synthesize and have flexibility in processing. Due to these reasons, CPGs are excellent candidates for academic study as well as industrial applications.[93] Conducting polymers such as polyaniline (PANI),[35,46,59] polypyrrole (PPy),[94] polythiophene (PTh),[95] polyfuran (PF)[96] are rich sources of heteroatoms such as N, S, O, etc which are used to prepare cross-linked networks and hierarchial porous 3D nanostructures (Figure

1.5).[93] The electrical conductivity in these CPGs is related to the π-conjugated chains, chemical structures, and amount of heteroatom-doping. Because of their tunable chemical and physical properties, CPGs have a wide range of applications, particularly in energy storage and conversion. The polymerization or gelation process for the synthesis of CPGs can be used to achieve doping with more than one heteroatom in the carbon nanomaterials by introducting an other heteroatom source followed by pyrolysis. For example, Liming Dai *et al* synthesized a three-dimensional PANI hydrogel crosslinked with phytic acids to achieve N, P co-doped mesoporous nanocarbons (Figure 1.6).[35]

### 1.2.3 Synthesis of Heteroatom-Modified Graphitic Carbon Nitride Nanomaterials

Graphitic carbon nitride (g-$C_3N_4$),[19,20,29,33,36,50,67,97-109] another interesting class of nitrogen containing carbon materials, has been well studied since its first successful demonstration as a photocatalyst by Markus Antonietti *et al*.[110] The presense of four N atoms in a molecule of g-$C_3N_4$ makes it a rich source of N. The synthesize of g-$C_3N_4$ is usually achieved by two-step carbonization from molecular sources like

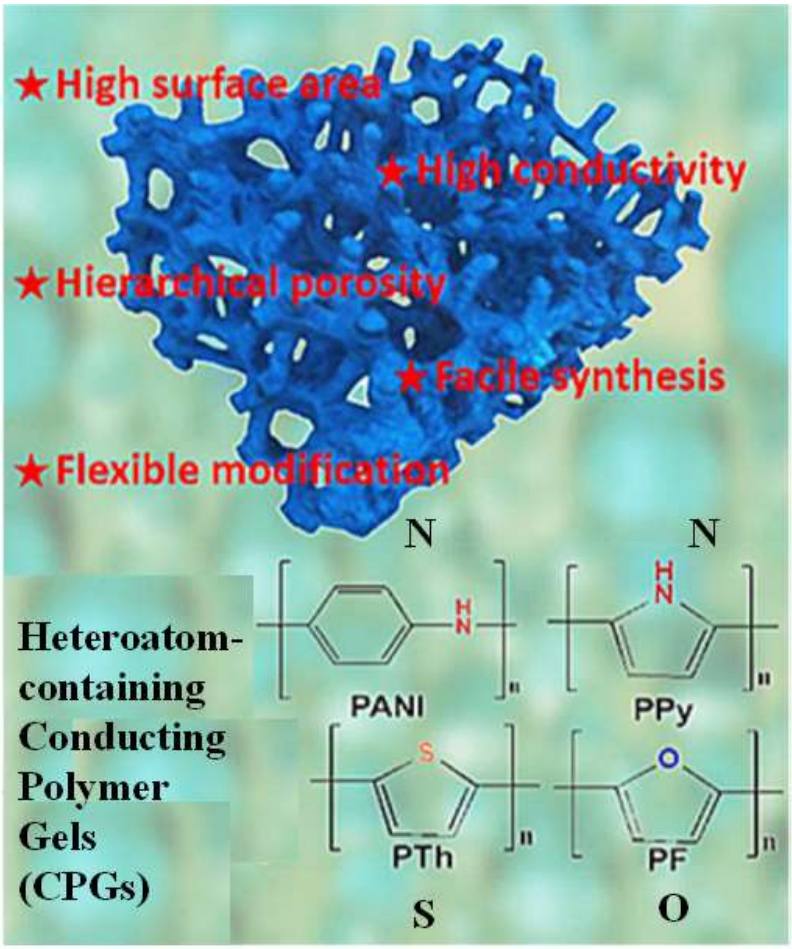


**Figure 1.5** Schematic representation for heteroatom-containing conducting polymer gels with their chemical structures for polyaniline (PANI), polypyrrole (PPy), polythiophene (PTh), polyfuran (PF). The figure is reproduced with permission from Ref. [93], © 2016 The American Chemical Society.

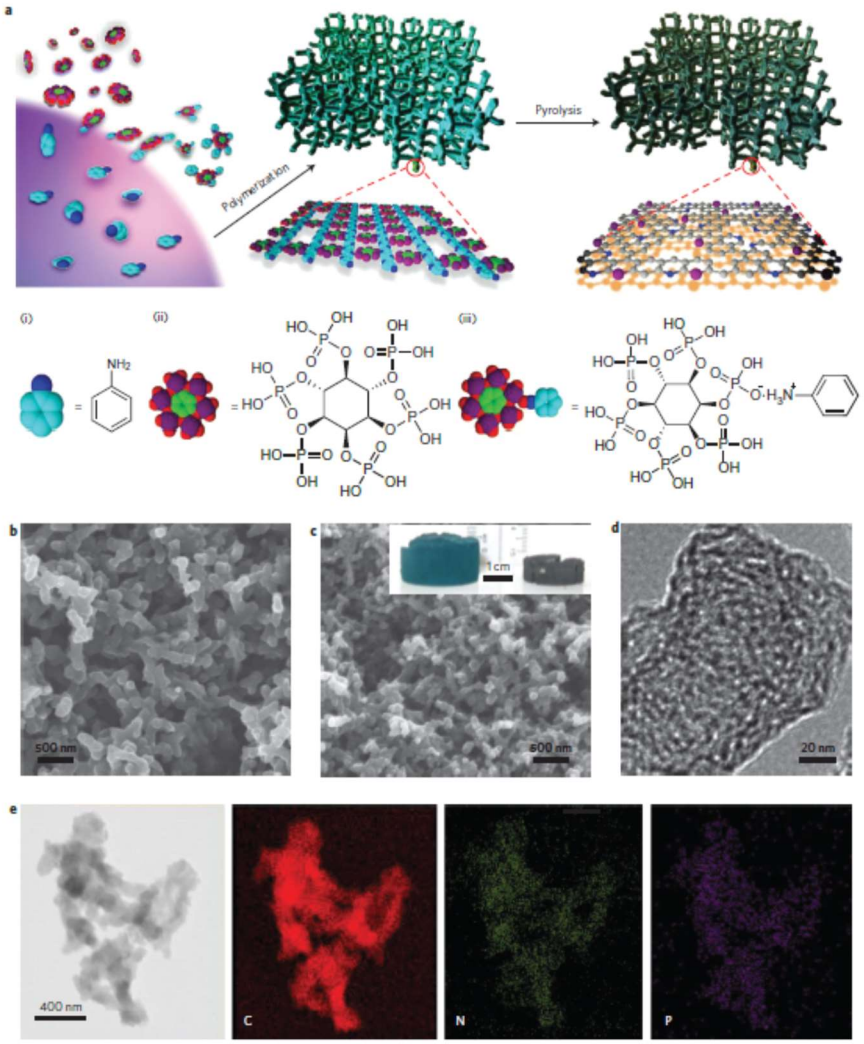


**Figure 1.6** Synthesis and morphological images of N, P co-doped mesoporous carbon foam. (a) Preparation of N and P containing foams. (b, c) SEM and (d, e) TEM images followed by elemental mapping for C, N, and P. The figure set is reproduced with permission from Ref. [125], © 2015 The Nature Publishing Group.

melamine, cyanamide or diacyanamide at ~600 °C. Further increasing the temperature above 600 °C causes destruction of g-$C_3N_4$ structures resulting into N-doped carbon. To increase the surface area and the number of active sites in g-$C_3N_4$, hard templates like silica nanoparticles or mesoporous silica are used.

The modification of g-$C_3N_4$ by doping, alteration or substitution with other heteroatoms like P, S, B, I, etc have been successfully achieved by making composites out of precursors of g-$C_3N_4$ like melamine, cyanamide or diacyanamide with desired sources of other heteroatoms followed by carbonization. Another way is to use a gaseous source of heteroatoms as a doping agent during carbonization of g-$C_3N_4$ precursors.[64] As synthesized g-$C_3N_4$ nanomaterials and P,[62] S,[7] B[68] modified g-$C_3N_4$, are used in photocatalysis. The high temperature annealed products of N-doped carbon nanomaterials, N and P/S/B-doped carbon nanomaterials are used as electrocatalysts, batteries, in the bio-medical field, etc.

### 1.2.4 MOFs as a Precursor/Template for the Synthesis of Heteroatom-Modified Carbon Nanomaterials

Metal-organic-frameworks (MOFs)[4,8,9,88,89,91,111-120] are a class of regular arragements of metal ions and its organic linkers forming a micro/mesoporous structure with high surface. Use of N containing organic linkers (e.g. 2-methyl imidazole) along with metal ions, makes it an attractive candidate to synthesize N-doped carbon nanomateials by pyrolysis of these MOFs. Most of the times, zinc containing zeolitic-imidazole-frameworks (ZIFs)[1,3,5,8,53,87] are used as precursors to synthesize N-doped carbon nanomaterials, as zinc can be easily sublimed during pyrolysis at high temperatures. In particular, ZIF-8 is widely used due to room temperature, easy and scalable synthesis. When other metal containing ZIFs are used, unwanted metal species in the pyrolyzed products can be easily etched away which results in increased porosity in the derived N-doped carbon nanomaterials. Furthermore, MOFs are being used as sacrificial templates to be coated with other heteroatoms containing carbon precursors to synthesize heteroatom-doped carbon nanomaterials after pyrolysis. By properly choosing the heteroatom containing carbon precursors, more than one heteroatom(s) such as N, P, S, or B can be easily doped in the pyrolyzed carbon nanomaterials. More interestingly, the use of MOFs as a sacrificial template can increase the surface area and porosity. Furthermore, the N present in the organic

linkers contributes to increase the amount of N doped in the pyrolyzed carbon nanomaterials. Due to these unique properties, MOFs are used as a precursor and/or sacrificial template to synthesize heteroatom-doped carbon nanomaterials with a wide range of possible applications, especially in the energy field.

## 1.3 Water Oxidation Applications as an Electrocatalyst

### 1.3.1 Fundamentals of Water Oxidation

Use of renewable sources is the only option to replace the diminishing fossil fuels. Splitting of water can result in clean molecular oxygen gas and hydrogen as a fuel. This process involves an important electrochemical process, i.e. water oxidation reaction. The water oxidation is the process of generating oxygen gas from water, so called oxygen evolution reaction (OER).[10,45,56,121,122] Along with oxygen reduction reaction (ORR) and/or hydrogen evolution reaction (HER), OER is part of the electrochemical process used in fuel cells and metal-air batteries also.

The overall water splitting reaction is given by

$$2H_2O \rightarrow 2H_2 + O_2 \qquad (1.1)$$

which is a combination of the two half-reactions of HER and OER, and can be performed in basic, acidic or neutral solutions as follows.

In acidic medium:

$$\text{HER} \quad : 2H^+ + 2e^- \rightarrow H_2 \qquad (1.2)$$

$$\text{OER} \quad : 2H_2O \rightarrow 4H^+ + O_2 + 4e^- \qquad (1.3)$$

In basic medium:

HER : $2H_2O + 2e^- \rightarrow H_2 + 2OH^-$ (1.4)

OER : $4OH^- \rightarrow 2H_2O + O_2 + 4e^-$ (1.5)

A typical polarization curve relating to electrochemical energy storage and conversion is shown in Figure 1.7. OER is a highly pH dependent electrochemical process so it is important to choose the electrolyte, which significantly influences the performance of the electrode material. Usually a basic electrolyte is more favorable than neutral or acidic electrolytes. The OER proceeds via formation of the reaction intermediates like (HO*, O*, and HOO*). The binding affinity of the electrode surface with these reaction intermediates determines the efficiency of OER electrocatalysts. Therefore, it is very important to choose a proper electrocatalyst. Metals or metal oxides such as $IrO_2$, $RuO_2$ based electrocatalysts are well established and already commercialized. To enhance the diffusion and penetration of the electrolyte, 3D electrodes of metal (Ni, Cu, Fe) foam, carbon paper or cloth, graphene foam are preferred over flat electrodes like metal (Ni, Cu) foil, glassy carbon, indium-doped tin oxide (ITO), etc.

Usually the performance between electrocatalysts is determined by

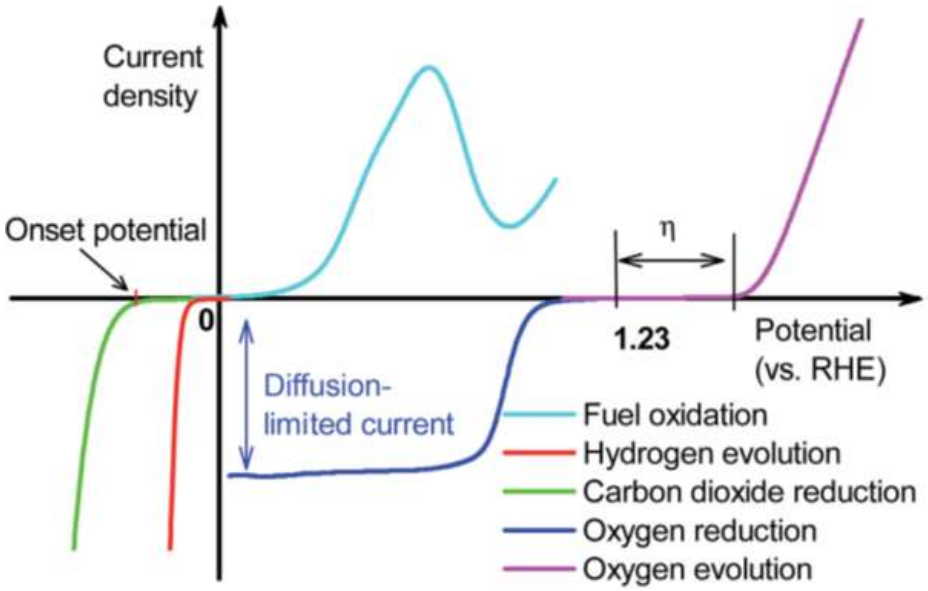


**Figure 1.7** The important electrochemical reactions plotted as a polarization curves. The figure is reproduced with permission from Ref. [2], © 2016 The Royal Society of Chemistry.

comparing their activities, faradic efficiencies and stability. The most common way to measure the activity of the electrocatalyst for OER is to measure the overpotential, $\eta$ (i.e. the additional potential required over the thermodynamic potential of water splitting, i.e. 1.23 V) to achieve a current density of 10 mA $cm^{-2}$ per geometrical area, which is near 10% efficient solar-to-fuels conversion device. To save the loss of electrical energy, the overpotential should be minimized.

The tafel slope in Tafel analysis is important for comparing the catalytic activity of various electrocatalysts and to understand the reaction mechanism, kinetics, and rate-determining step (RDS).

$$\eta = b.log\left(\frac{j}{j_0}\right) \qquad (1.6)$$

where $\eta, b, j, j_0$ are overpotential, Tafel slope, the current density, and the exchange current density respectively. The high current density with low Tafel slope is necessary to perform as a good OER electrocatalyst.

The durability or stability test is checked by measuring a device for a long period. Also, the activity of OER electrocatalysts is decided by the quality of an electrocatalyst i.e., faradic efficiency of an OER catalyst which is the quantification of the amount of generated $O_2$ divided by the

amount of theoretically expected amount of $O_2$ based on the charge passed during electrolysis. Other parameters such as turnover frequency (TOF) and mass activity are calculated as follows:

$$\text{TOF} = (j \times A) / (4nf) \quad (1.7)$$

where, $j$, $A$, $n$, and $f$ are the current density at overpotential, the area of working electrode, number of moles of active materials and Faraday constant (96,500 C $mol^{-1}$), respectively.

$$\text{Mass activity} = j / m \quad (1.8)$$

where $j$ and $m$ are the current density at given overpotential and mass loading on the working electrode.

In short, the critical parameters of a good OER electrocatalyst for real industry applications are as follows. It should have a minimal overpotential ($\eta$) and Tafel slope to minimize the energy loss during the reactions. Long-term durability with high TOF and mass activity is needed for the efficient use of the electrocatalyst. Finally, the electrocatalyst should be environmentally friendly, cheap, easy to be synthesized for large-scale production.

### 1.3.2 Heteroatom-Modified Carbon Nanomaterials based OER Electrocatalyst

As discussed above, it is important that OER electrocatalysts have good parameters to perform well in real industrial applications. Thomas Jaramillo *et al.* summarized the development of metal or metal oxide based OER electrocatalysts in a review.[123] The high cost and scarcity of metal-based electrocatalysts hampers their use in practical applications. Until now, the only alternative to them is carbon-based electrocatalysts which showed comparable performances with traditional metal-based electrocatalysts. Scientists found many ways to further improve the performance of these carbon-based electrocatalysts such as nanostructuring, increasing the number of active sites by increasing surface area and porosity, making composites with other conducting materials, modification by heteroatom(s) in carbon nanomaterials (Figure 1.8). These efforts significantly improved the OER performance of carbon nanomaterials compared to metal-based systems.

As already discussed, graphitic carbon nitride (g-$C_3N_4$) is a rich source of N, which consists of electrochemically active sites such as pyridinic and pyrrolic N species. The conductivity of g-$C_3N_4$ is improved by

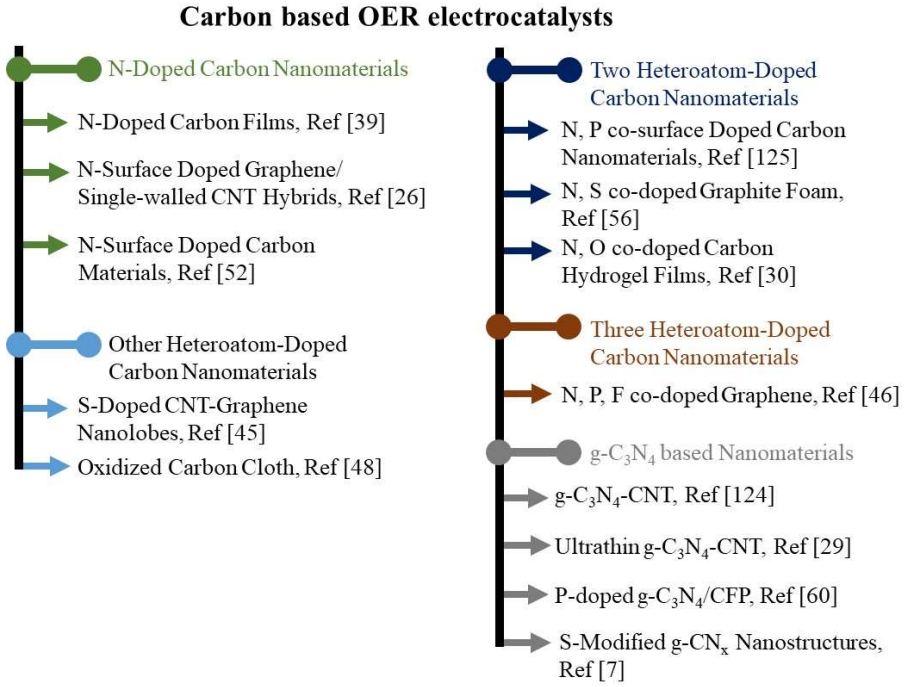


**Figure 1.8** Recent reports on the carbon-based OER electrocatalysts.

making composites with graphene and/or CNTs to form g-$C_3N_4$/graphene[29] and g-$C_3N_4$/CNTs[124] and application of these nanomaterials as an OER electrocatalysts show overpotential of $\eta$ = 539 and 370 mV respectively. The direct use of carbon paper as an electrode doped with N show $\eta$ = 414.5 mV due to better access of the electrolyte ions in the 3D carbon networks.[39] While N-surface doped graphene coupled with SWCNTs[26] show $\eta$ = 400 mV, and N-surface doped carbon materials[52] show $\eta$ = 420 mV.

P-doping in carbon nanomaterials has similar enhancement effects. P-doped g-$C_3N_4$ with carbon fiber paper[60] show $\eta$ = 400 mV. S-doping significantly reduces overpotential, as predicted by first principle calculations. S-doped CNT-graphene nanolobes hybrid[45] shows $\eta$ = 350 mV and our study of S-modified g-$CN_x$ nanostructures[7] shows $\eta$ = 290 mV, which is the best performance in carbon-based electrocatalysts for OER. Additionally, O-doping of carbon cloth[48] shows $\eta$ = 477 mV. Synergistic effects can be achieved by doping of more than one heteroatom in carbon nanomaterials. Recently, N, P co-surface doped carbon materials[125] show bifunctional electrocatalyst for OER with $\eta$ = 725 mV and ORR. N, S co-doped graphite foam[56] show $\eta$ = 380 mV and N, O co-doped carbon hydrogel films[30] show $\eta$ = 516 mV.

Heteroatom-doping of graphene with N, P, F[46] shows $\eta$ = 570 mV. The summary of recent reports is given in table 1.1. Some of the carbon based electrocatalysts showed a much higher performances compared to metal or metal oxide based electrocatalysts. Indeed, in the near future carbon-based nanomaterials will totally replace the traditional metal and metal oxide based electrocatalysts.

| **Sr. No.** | **Sample** | **V at 10 mA cm$^{-2}$ (V vs. RHE) *(overpotential, η)*** | **References** |
|---|---|---|---|
| 1 | N-doped C films | 1.644, pH 13 *(η = 414.5 mV)* | *Adv. Sci.* **2015**, *2,* 1400015, Ref [39] |
| 2 | N-surface doped graphene/single-walled CNT hybrids | 1.63, pH 13 (*η = 400 mV)* | *Small* **2014***, 10,* 2251, Ref [26] |
| 3 | N-surface doped carbon materials | 1.65, pH 13 *(η = 420 mV)* | *Nat. Commun.* **2013,**, *4,* 2390, Ref [52] |
| 4 | S-doped CNT-graphene nanolobes | 1.58, pH 14 *(η = 350 mV)* | *Adv. Energy Mater.***2016***, 6,* 1501966, Ref [45] |
| 5 | Oxidised-C cloth | 1.707, pH 13 *(η = 477 mV)* | *Chem. Commun.* **2015**, *51,* 1616, Ref [48] |
| 6 | N, P co-surface doped carbon materials | 1.95, pH 13 *(η = 725 mV)* | *Nat. Nanotech.* **2015***, 10,*444, Ref [125] |
| 7 | N, S co-doped graphite foam | 1.51, pH 13 *(η = 380 mV)* | *Adv. Energy Mater.* **2016***, 6,* 1501492, Ref [56] |
| 8 | N, O co-doped C | 1.746, pH 13 | *Adv. Mater.* **2014**, |

| | | | |
|---|---|---|---|
| | hydrogel films | *(η = 516 mV)* | *26,* 2925, Ref [30] |
| 9 | N, P, F co-doped graphene | 1.80, pH 13 *(η = 570 mV)* | *Angew. Chem. Int. Ed.* **2016**, *55,* 13296, Ref [46] |
| 10 | g-$C_3N_4$/CNT | 1.60, pH 14 *(η = 370 mV)* | *Angew. Chem. Int. Ed.* **2014**, *53,* 7281, Ref [124] |
| 11 | Ultrathin g-$C_3N_4$/graphene | 1.769, pH 13 *(η = 539 mV)* | *ChemSusChem.* **2014**, *7,* 2125, Ref [29] |
| 12 | P-doped g-$C_3N_4$/CFP | 1.63, pH 13 *(η = 400 mV)* | *Angew. Chem. Int. Ed.* **2015**, *54,* 4646, Ref [60] |
| 13 | S-modified g-$CN_x$ nanostructures | 1.52, pH 14 *(η = 290 mV)* | *Small* **2017**, *13,* 1603893, Ref [7] |

**Table 1.1** Comparison table of recent reports on the carbon-based OER electrocatalysts.

## 1.4 Applications in Supercapacitor Electrodes

### 1.4.1 Fundamentals of Supercapacitors

Nowadays, ultra-high-power energy resources are required because of the demand for hybrid electric vehicles and portable electronic devices. Batteries provide high energy density for various daily life applications due to huge amount of energy stored in it. However, batteries have intrinsic limitations to its specific high power demands as seen in Ragone plot (Figure 1.9a). As an alternative, electrochemical capacitors show fast charge/discharge processes, a long cycle life (~1000000) and high specific power (10 kW $kg^{-1}$) and are also known as supercapacitors or ultracapacitors. The increasing number of publications every year as shown in Figure 1.9b, is an indication of the huge amount of ongoing research in supercapacitor applications. Depending on the charge storage mechanism between the electrolyte ions and electrodes, it can be classified into three categories (Figure 1.10). First, the electrical double layer capacitor (EDLC) uses pure electrostatic attraction between ions and the charged surface of an electrode such as carbon based electrodes. Second, pseudocapacitors are based on Faradaic charge transfer reactions of the electro-active species on the surface of the electrode or

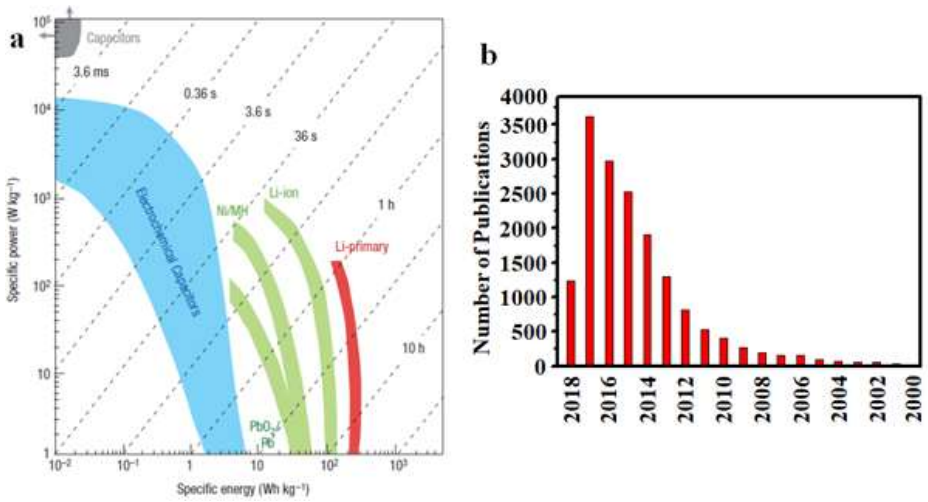


**Figure 1.9** (a) Ragone plot. If a supercapacitor is used in an electric vehicle, the specific power shows how fast one can go, and the specific energy shows how far one can go on a single charge. Times shown are the time constants of the devices, obtained by dividing the energy density by the power. (b) Number of publications on supercapacitors (data obtained from Web of Science on April 26, 2018).The figure (a) is reproduced with permission from Ref. [55], © 2008 The Nature Publishing Group.

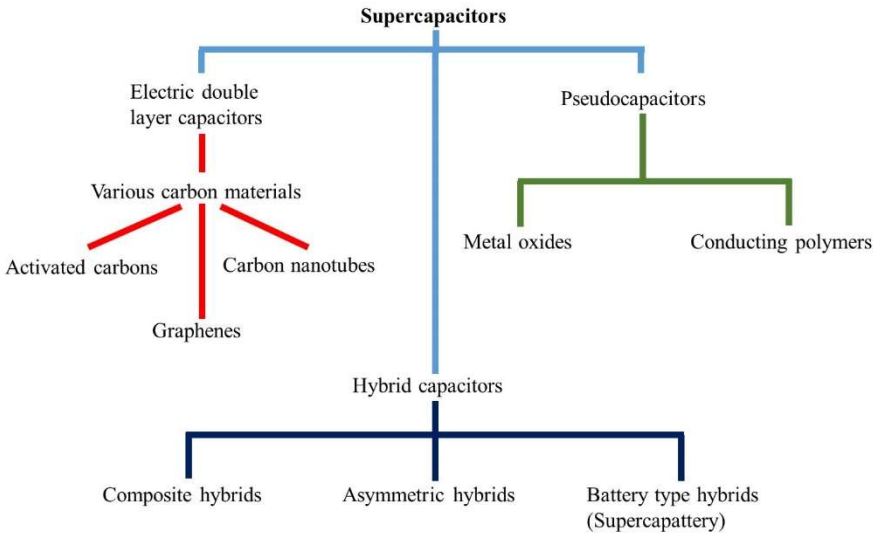


**Figure 1.10** Tree diagram of supercapacitors and its types.

fast and reversible oxidation/reduction (redox) such as conducting polymers and transition metals/metal oxides electrodes. Third is the combination of both EDLC and pseudocapacitance behavior known as hybrid capacitors.

### 1.4.2 The Energy Storage Mechanism in EDLCs

Due to the limited charge storage area between the two charged plates, conventional capacitors store only little energy. On the other hand, supercapacitors store much more energy due to its high surface area.[51,126] In the 19th century, von Helmholtz presented the electric double layer (EDL) concept for the distribution of opposite charges at the interface of colloidal particles assuming that two layers of opposite charge formed at the electrode/electrolyte interface which are spaced at an atomic distance, similar to that of two-plate conventional capacitors. Gouy and Chapman modified Helmholtz' theory and considered and included the diffusion layer, a continuous distribution of cations and anions in the electrolyte solution driven by thermal motion (Figure 1.11a).[51] This work was further modified by Stern, considering two regions of ion distribution-the inner region called the compact layer or Stern layer and the other regions known as the diffuse layer (Figure

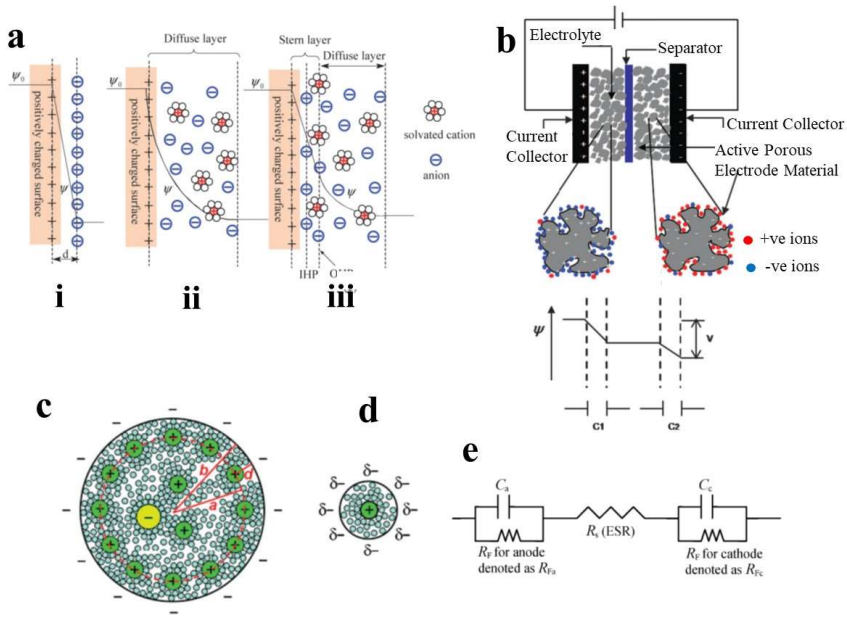


**Figure 1.11** Basic understanding of supercapacitors. Schematic representation for (a) Models of the electrical double layer (i) The Helmholtz model, (ii) The Gouy-Chapman model, and (iii) The Stern model, with the inner Helmholtz plane (IHP) and outer Helmholtz plane (OHP). (b) EDLC model for porous electrode, (c) Electric double-cylinder capacitor (EDCC) model, (d) Electric wire-in-cylinder capacitor (EWCC) model and (e) RC equivalent circuit of a single-cell supercapacitor. Figures (a), (b) and (e) are reproduced with permission from Ref. [51], © 2009 The Royal Society of Chemistry; and (c), (d) from Ref. [129], © 2008 Wiley-VCH.

1.11a).[51] The mostly hydrated ions in the compact layer are adsorbed by the electrode. The compact layer is comprised of specifically adsorbed ions and non-specifically adsorbed counter-ions. The two types of adsorbed ions are the inner Helmholtz plane (IHP) and outer Helmholtz plane (OHP). A combination of the Stern-compact double layer capacitance ($C_H$) and the diffusion region capacitance ($C_{diff}$) is $C_{dl}$ (capacitance of EDL)

$$\frac{1}{C_{\mathrm{dl}}} = \frac{1}{C_{\mathrm{H}}} + \frac{1}{C_{\mathrm{diff}}} \qquad (1.6)$$

The EDL performance at a planar electrode surface depends on (1) the types of electrolyte ions, (2) the solvent, (3) the chemical affinity between the adsorbed ions and the surface of the electrode, and (4) the electrical field across the electrode.

But for porous material with a high specific surface area, the EDL behavior is more complicated than planar electrode material due to (1) slow ion transportation in a confined system affected by the tortuous mass transfer path, (2) the space constraint inside the pores, (3) the ohmic resistance of the electrolyte, and (4) the wetting behavior of the pore surface by the electrolyte. A schematic illustration of an EDLC with porous carbon electrode is shown in Figure 1.11b.[51]

The capacitance of an EDLC is usually considered to be a parallel-plate capacitor:

$$C = \frac{\varepsilon_r \varepsilon_0}{d} A \qquad (1.7)$$

where $\mathcal{E}_r$, $\mathcal{E}_0$, $A$, and $d$ are the electrolyte dielectric constant, the permittivity of a vacuum, the specific surface area of the electrode, and the thickness of the EDL respectively. It can be seen from this equation that the capacitance (C) is directly proportional to the specific surface area (A). But recently some experiments have shown a non-linear relationship. Raymundo-Pinero *et al.* observed that for the overall capacitance, micropores have a critical role and suggested that partial desolvation of hydrated ions leads to an enhanced capacitance.[127] Work by Simon and Gogotsi *et al.* showed that there is an anomalous capacitance increase with pores smaller than 1 nm and observed that when the electrode pore size was very close to the ion size, maximum capacitance has been achieved.[128] In addition, Jingsong Huang and co-workers considered the pore curvature in a nanoporous carbon-based supercapacitors and different capacitive behavior was proposed depending on the size of the pore.[129] An electric wire-in-cylinder capacitor (EWCC) model is proposed for describing microporous carbon

electrodes, while an electric double-cylinder capacitor (EDCC) model is considered for describing mesoporous carbon electrodes, as shown in Figure 1.11c and d.[129] This theory is not valid for the bigger pores. The capacitance can be calculated by following equations (1.8) and (1.9) for the EDCC model and the EWCC model, respectively:

$$C = \frac{\varepsilon_r \varepsilon_0}{b\,1\ \ [b/(b-d)]} A \qquad (1.8)$$

$$C = \frac{\varepsilon_r \varepsilon_0}{b \ln[b/a_0]} A \qquad (1.9)$$

where $b$, $d$, and $a_0$ are the pore radius, the distance of between ions and the surface of the carbon electrode, and the effective size of the counter-ions, respectively. A simplified schematic summarizing the pore size dependent models for supercapacitor is shown in Figure 1.12.[129]

### 1.4.3 The Performance of Supercapacitors

Some of the advantages of supercapacitors compared batteries include high power density, long cycleability, fast charge/discharge processes, low self-discharge, cheap price, safe operation, etc. The basic *RC* circuit schematic of a single-cell two electrodes supercapacitor is shown in Figure 1.11e.

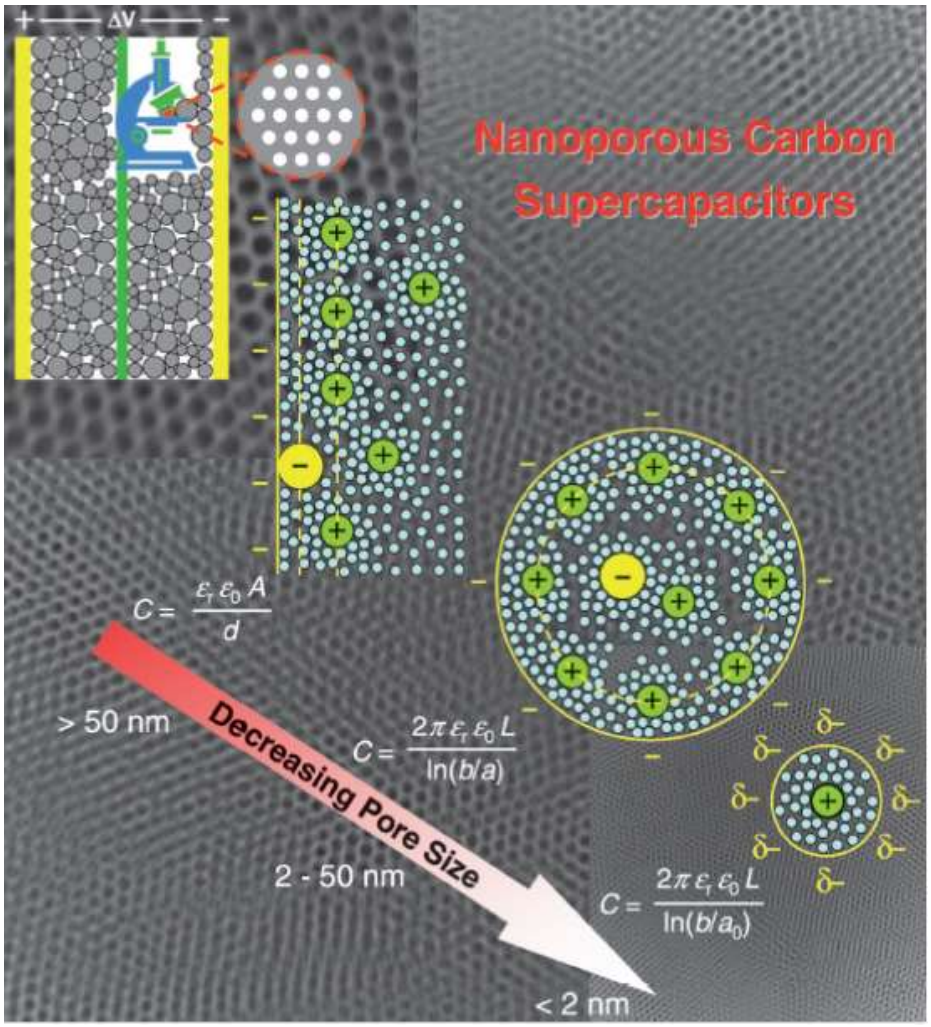


**Figure 1.12** The simplified schematic representation for the pore size dependent models for supercapacitor. Figure is reproduced from the article cover picture with permission from Ref. [129], © 2008 Wiley-VCH.

$C_a$, $C_c$, $R_s$ are the capacitance of the anode, cathode, and the equivalent series resistance (ESR) of the cell respectively. $R_F$, $R_{Fa}$, and $R_{Fc}$ is the resistance due to the self-discharge of a single electrode, anode and the cathode respectively.[51] The total capacitance of the cell ($C_T$) is given by:

$$\frac{1}{C_T} = \frac{1}{C_a} + \frac{1}{C_c} \quad (1.10)$$

For an *RC* circuit, the characteristic of a capacitor is shown by the time constant (τ) defined as resistance ($R$) × capacitance ($C$).

The energy ($E$) and power ($P$) of a single cell supercapacitor are defined as:

$$E = \frac{1}{2} C_T V^2 \quad (1.11)$$

$$P = \frac{V^2}{4R_s} \quad (1.12)$$

where $C_T$ is the total capacitance of the cell in farads, $V$ is the cell voltage in volts, and $R_s$ is the ESR in ohms. The thermodynamic stability of the electrolyte solution limits the cell voltage. Every factor in the equivalent circuit is critical for the overall performance of the supercapacitor and is strongly correlated with the nature of the electrode material. The different types of resistances in the system include mass transfer

resistance of the ions in the matrix, the intrinsic electronic properties of the electrode matrix and electrolyte solution, and contact resistance between the current collector and the electrode associated with ESR. For a good supercapacitor, it should meet all of the critical criterions such as a minimal ESR, high operating cell voltage and large capacitance. Therefore it is necessary it is important carefully design the electrode materials and the electrolyte. In addition, it is important to control the porosity of high surface area carbon electrodes without degrading the stability. The factors affecting the cell performance of supercapacitors is shown in Figure 1.13.[130] A research overview of recent developments on heteroatom-modified/doped carbon nanomaterials as an electrode materials will be discussed in the next section.

### 1.4.4 Heteroatom-Modified Carbon Nanomaterials based Supercapacitor Electrode

Carbon has attracted much interest as electrode materials for electrochemical capacitors due to many reasons such as low production cost, high electrical conductivity and chemical stability, high surface area, etc.[57,58,69,70,83] Many strategies have been developed to

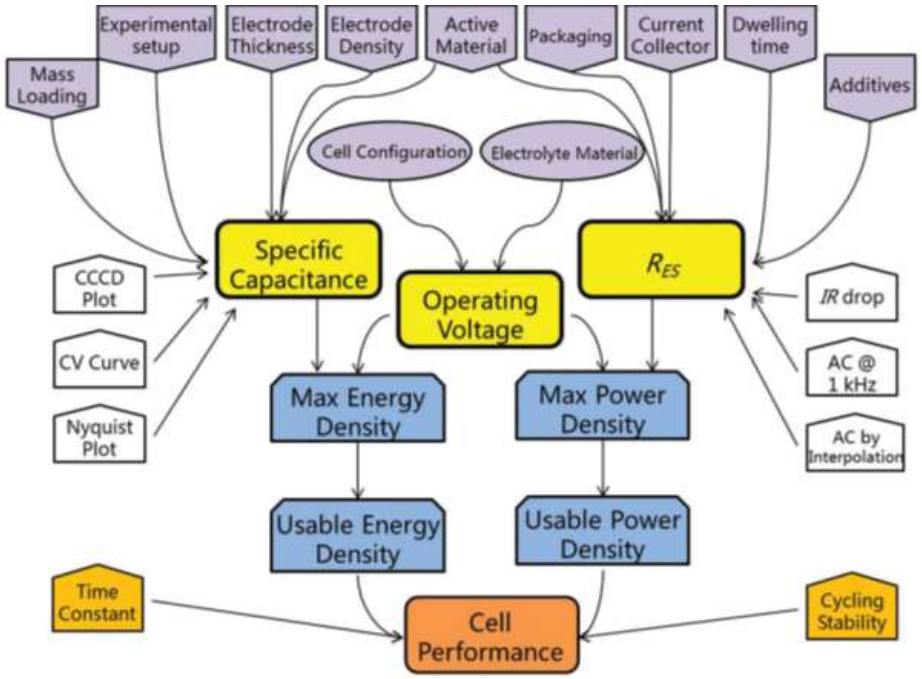


**Figure 1.13** The diagrammatic representation of important parameters which are necessary for supercapacitors. Figure is reproduced with permission from Ref. [130], © 2014 Wiley-VCH.

increase the performance of carbon nanomaterials in EDLC, such as various activation processes used to increase the surface area and to modify the pore size which ultimately facilitates fast ion and electron transportation. For example, Rodney Ruoff *et al.* demonstrated KOH activation of microwave exfoliated GO (MEGO) as seen in Figure 1.14.[15] Additionally, the synthesis of high surface area and porosity controlled carbon nanomaterials by a template or non-template method to enhance the electrical properties in carbon nanomaterials is quite well known.

Surface modification of heteroatoms such as N, P, S, and B by substitution, incorporation or doping in carbon nanomaterials have a critical role for increasing performance.[59,92] These modifications in carbon nanomaterials provide a pair of electrons to achieve pseudocapacitance which increases the overall capacitances due to surface faradaic reactions (Figure 1.15).[131] As discussed in section 1.1, there are various N environments present in N-doped carbon materials, such as pyrrolic, pyridinic and quaternary N which can enhance electron transfer and improve the electrical conductivity of carbon nanomaterials.

Along with N incorporation in carbon nanomaterials, other heteroatoms

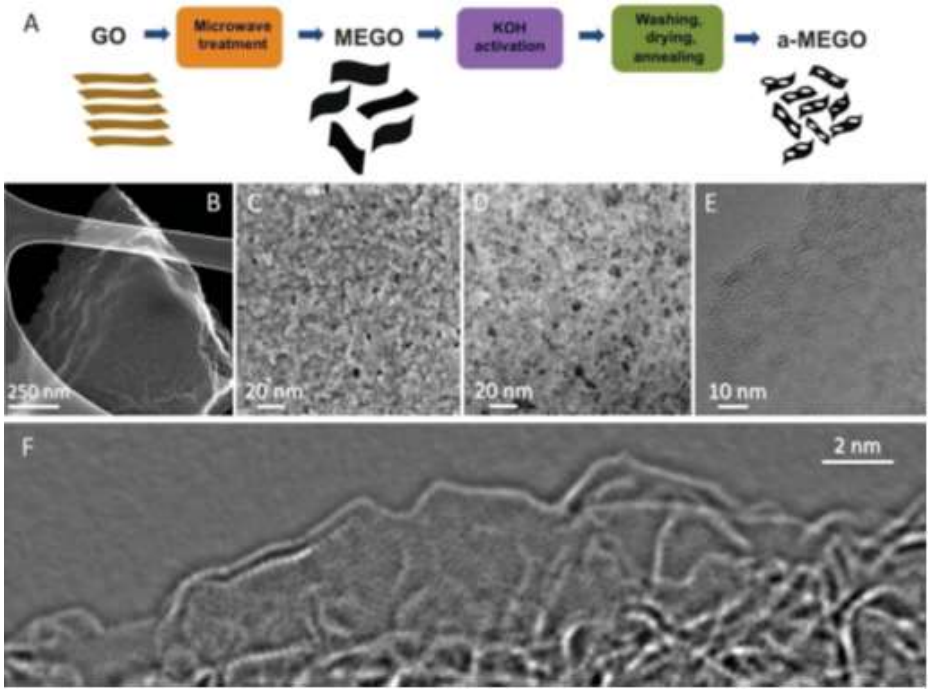


**Figure 1.14** Synthesis and morphological characterization of microwave exfoliated graphene oxide (MEGO). (A) Schematic showing the microwave exfoliation/reduction of GO and the following chemical activation of MEGO with KOH. (B) and (C) SEM images, (D) ADF-STEM image, (E) and (F) HRTEM image of MEGO. The figures are reproduced with permission from Ref. [15], © 2011 AAAS.

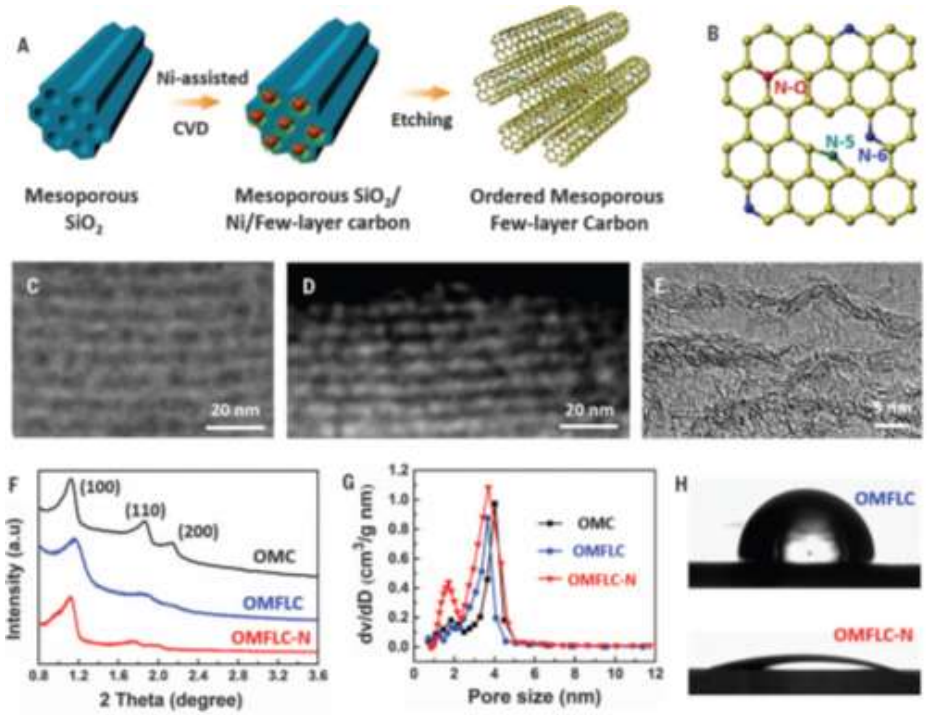


**Figure 1.15** Synthesis and characterization of ordered mesoporous few-layer carbon (OMFLC). (A) Synthesis scheme of OMFLC. (B) Possible locations of N-doped sites. (C and D) HAADF-STEM image. (E) HRTEM image. (F) Low-angle X-ray diffraction patterns. (G) Pore size distributions. (H) Water contact angle images. The figures are reproduced with permission from Ref. [131], © 2015 AAAS.

such as P, S, B, O and F also increase pseudocapacitance and EDLC performances. Due to the lone pair electrons or charge delocalization in carbon nanomaterials the pseudocapacitance increase. Also, it has been shown that modification of heteroatoms in carbon nanomaterials can increase surface activity, wettability, electrical conductivity, metallic properties, thermal stability or degree of disorder. These positive changes due to the modification of heteroatoms into carbon nanomaterials increases the electrochemical performance of supercapacitors. Special attention is focused on the combination of more than one heteroatom(s) which can significantly increase the EDLC performance compared to their individual counterpart modification in carbon nanomaterials due to synergistic effects. Example combinations of heteroatoms include N/P, N/S, N/B, N/P/S, N/P/B, N/S/B, N/P/S/B, P/S, P/B, P/S/B, S/B, etc. Theoretical and experimental studies have investigated how the introduced heteroatoms affect the performance of supercapacitors but a clear answer is still elusive.

## 1.5 Dissertation Overview

For fundamental scientific research as well as various practical applications, the designed synthesis of heteroatom-containing carbon nanomaterials is of key importance. Although it has improved the properties or performances of carbon nanomaterials, the modification of carbon nanomaterials with heteroatoms, which includes the process of doping, substitution or alternation, is not well understood yet. Considering the widespread applicability of heteroatom-modified carbon nanomaterials, there is still a lot of room left for further improvement of syntheses of multi-heteroatom-modified carbon nanomaterials. Further contributions in the field of heteroatom-modified carbon nanomaterials may lead to a paradigm shift the near future. This dissertation is focused on the synthesis of carbon nanomaterials and their modification with heteroatoms, with an emphasis on their application for water oxidation and as supercapacitor electrodes.

In the first part (Chapter-2), natural geodes-inspired unique melamine nanogeodes are synthesized to form graphitic carbon nitride nanostructures. Sulfur-modified graphitic carbon nitride nanostructures were obtained by *in-situ* sulfur modification during the pyrolysis of

melamine nanogeodes. The modification of sulfur in graphitic carbon nitride nanostructures significantly improves the water oxidation reaction by minimizing the activation energy. This performance is the best among carbon-based electrocatalysts for water oxidation. Our synthesis process is simple, inexpensive, and environmentally friendly which are the essential criteria for practical applications. Furthermore, the synthetic strategy and our understanding can be applied directly to various other electrocatalyts, emphasizing the importance of nanostructure and sulfur modification for better activity and stability.

In the third part (Chapter-3), multi-heteroatom-doping in carbon is achieved by a wrap-bake-sublime approach. MOF nanoparticles are used as a sacrificial template to be wrapped by novel N, P containing oligomers and baking of these wrapped nanoparticles results in hollow N, P co-doped hollow carbon nanostructures. The microporosity developed in co-doped carbon nanocages is easily fine-tuned. These co-doped carbon nanocages are used as supercapacitor electrodes which showed excellent correlation between their electrochemical performance and the microporosity. Moreover, a good correlation was found between the electrochemical performance and ratio of the amounts of N, P co-doping in the carbon nanocages. Finally, the gram-scale synthesis and

the assembly of a symmetric all-solid-state-supercapacitor device with long term durability validates the practical applicability of our approach. This is a unique report on the synthesis of microporosity controlled and heteroatom co-doped carbon nanocages with gram-level synthesis.

## 1.6 References


[1] Y. Pan, K. Sun, S. Liu, X. Cao, K. Wu, W.-C. Cheong, Z. Chen, Y. Wang, Y. Li, Y. Liu, D. Wang, Q. Peng, C. Chen, Y. Li, *J. Am. Chem. Soc.* **2018**, *140*, 2610.

[2] J. Zhang, H. Li, P. Guo, H. Ma, X. S. Zhao, *J. Mater. Chem. A* **2016**, *4*, 8497.

[3] L.-F. Chen, Y. Lu, L. Yu, X. W. Lou, *Energy Enviorn. Sci.* **2017**, *10*, 1777.

[4] S. Fu, C. Zhu, J. Song, D. Du, Y. Lin, *Adv. Energy Mater.* **2017**, *7*, 1700363.

[5] P. Huang, H. Li, X. Huang, D. Chen, *ACS Appl. Mater. Interfaces* **2017**, *9*, 21083.

[6] J. Jin, X. Qiao, F. Zhou, Z.-S. Wu, L. Cui, H. Fan, *ACS Appl. Mater. Interfaces* **2017**, *9*, 17317.

[7] V. S. Kale, U. Sim, J. Yang, K. Jin, S. I. Chae, W. J. Chang, A. K. Sinha, H. Ha, C.-C. Hwang, J. An, H.-K. Hong, Z. Lee, K. T. Nam, T. Hyeon, *Small*, **2017**, *13*, 1603893.

[8] Y. V. Kaneti, S. Dutta, M. S. A. Hossain, M. J. A. Shiddiky, K.-L. Tung, F.-K. Shieh, C.-K. Tsung, K. C. W. Wu, Y. Yamauchi, *Adv. Mater.* **2017**, *29*, 1700213.

[9] Y. V. Kaneti, J. Tang, R. R. Salunkhe, X. Jiang, A. Yu, K. C. W. Wu, Y. Yamauchi, *Adv. Mater.* **2017**, *29*, 1604898.

[10] S. Liu, Z. Wang, S. Zhou, F. Yu, M. Yu, C.-Y. Chiang, W. Zhou, J. Zhao, J. Qiu, *Adv. Mater.* **2017**, *29*, 1700874.

[11] C. Wan, X. Huang, *Mater. Today Commun.* **2017**, *11*, 38.

[12] D. Xu, Y. Tong, T. Yan, L. Shi, D. Zhang, *ACS Sustain. Chem. Eng.* **2017**, *5*, 5810.

[13] W. Hooch Antink, Y. Choi, K.-d. Seong, J. M. Kim, Y. Piao, *Adv. Mater. Interfaces* **2018**, *5*, 1701212.

[14] A. K. Geim, K. S. Novoselov, *Nat. Mater.* **2007**, *6*, 183.

[15] Y. Zhu, S. Murali, M. D. Stoller, K. J. Ganesh, W. Cai, P. J. Ferreira, A. Pirkle, R. M. Wallace, K. A. Cychosz, M. Thommes, D. Su, E. A. Stach, R. S. Ruoff, *Science*, **2011**, *332*, 1537.

[16] Y. Liang, Y. Li, H. Wang, J. Zhou, J. Wang, T. Regier, H. Dai, *Nat. Mater.* **2011**, *10*, 780.

[17] S. Yang, X. Feng, X. Wang, K. Müllen, *Angew. Chem. Int. Ed.* **2011**, *50*, 5339.

[18] Z.-S. Wu, A. Winter, L. Chen, Y. Sun, A. Turchanin, X. Feng, K. Müllen, *Adv. Mater.* **2012**, *24*, 5130.

[19] Y. Wang, X. Wang, M. Antonietti, *Angew. Chem. Int. Ed.* **2012**, *51*, 68.

[20] Y. Zheng, Y. Jiao, M. Jaroniec, Y. Jin, S. Z. Qiao, *Small*, **2012**, *8*, 3550.

[21] Z. Niu, L. Zhang, L. Liu, B. Zhu, H. Dong, X. Chen, *Adv. Mater.* **2013**, *25*, 4035.

[22] L. Borchardt, M. Oschatz, S. Kaskel, *Mater. Horizons*, **2014**, *1*, 157.

[23] X. Fan, C. Yu, J. Yang, Z. Ling, J. Qiu, *Carbon*, **2014**, *70*, 130.

[24] X. Wang, G. Sun, P. Routh, D.-H. Kim, W. Huang, P. Chen, *Chem. Soc. Rev.* **2014**, *43*, 7067.

[25] H. Huang, S. Yang, R. Vajtai, X. Wang, P. M. Ajayan, *Adv. Mater.* **2014**, *26*, 5160.

[26] G.-L. Tian, M.-Q. Zhao, D. Yu, X.-Y. Kong, J.-Q. Huang, Q. Zhang, F. Wei, *Small*, **2014**, *10*, 2251.

[27] Y. Zheng, Y. Jiao, Y. Zhu, L. H. Li, Y. Han, Y. Chen, A. Du, M. Jaroniec, S. Z. Qiao, *Nat. Commun.*, **2014**, *5*, 3783.

[28] X. Long, J. Li, S. Xiao, K. Yan, Z. Wang, H. Chen, S. Yang, *Angew. Chem. Int. Ed.* **2014**, *53*, 7584.

[29] J. Tian, Q. Liu, A. M. Asiri, K. A. Alamry, X. Sun,

*ChemSusChem*, **2014**, *7*, 2125.

[30] S. Chen, J. Duan, M. Jaroniec, S. Z. Qiao, *Adv. Mater.* **2014**, *26*, 2925.

[31] M. Mousavi-Khoshdel, E. Targholi, M. J. Momeni, *J. Phys. Chem. C* **2015**, *119*, 26290.

[32] J. Shui, M. Wang, F. Du, L. Dai, *Sci. Adv.*, **2015**, *1*, e1400129.

[33] Y. Zhao, J. Zhang, L. Qu, *ChemNanoMat*, **2015**, *1*, 298.

[34] J. Liu, W. Li, L. Duan, X. Li, L. Ji, Z. Geng, K. Huang, L. Lu, L. Zhou, Z. Liu, W. Chen, L. Liu, S. Feng, Y. Zhang, *Nano Lett.* **2015**, *15*, 5137.

[35] J. Zhang, Z. Zhao, Z. Xia, L. Dai, *Nat. Nanotech.* **2015**, *10*, 444.

[36] C. Xu, Q. Han, Y. Zhao, L. Wang, Y. Li, L. Qu, *J. Mater. Chem. A* **2015**, *3*, 1841.

[37] J. Zhang, Y. Chen, X. Wang, *Energy Enviorn. Sci.* **2015**, *8*, 3092.

[38] Y. Ito, W. Cong, T. Fujita, Z. Tang, M. Chen, *Angew. Chem. Int. Ed.* **2015**, *54*, 2131.

[39] S. Chen, J. Duan, J. Ran, S. Z. Qiao, *Adv. Sci.* **2015**, *2*, e1400015.

[40] C. Hu, J. Xue, L. Dong, Y. Jiang, X. Wang, L. Qu, L. Dai, *ACS Nano*, **2016**, *10*, 1325.

[41] P. Pachfule, D. Shinde, M. Majumder, Q. Xu, *Nat. Chem.* **2016**, *8*, 718.

[42] Y. Jia, L. Zhang, A. Du, G. Gao, J. Chen, X. Yan, C. L. Brown, X. Yao, *Adv. Mater.* **2016**, *28*, 9532.

[43] Y. Hou, Z. Wen, S. Cui, X. Feng, J. Chen, *Nano Lett.* **2016**, *16*, 2268.

[44] J. Song, Z. Yu, M. L. Gordin, D. Wang, *Nano Lett.* **2016**, *16*, 864.

[45] A. M. El-Sawy, I. M. Mosa, D. Su, C. J. Guild, S. Khalid, R. Joesten, J. F. Rusling, S. L. Suib, *Adv. Energy Mater.* **2016**, *6*, 1501966.

[46] J. Zhang, L. Dai, *Angew. Chem. Int. Ed.* **2016**, *55*, 13296.

[47] S. Iijima, *Nature*, **1991**, *354*, 56.
[48] N. Cheng, Q. Liu, J. Tian, Y. Xue, A. M. Asiri, H. Jiang, Y. He, X. Sun, *Chem. Commun.* **2015**, *51*, 1616.
[49] Q. Wang, J. Yan, Z. Fan, *Energy Enviorn. Sci.* **2016**, *9*, 729.
[50] Y. Gong, M. Li, Y. Wang, *ChemSusChem*, **2015**, *8*, 931.
[51] L. L. Zhang, X. S. Zhao, *Chem. Soc. Rev.* **2009**, *38*, 2520.
[52] Y. Zhao, R. Nakamura, K. Kamiya, S. Nakanishi, K. Hashimoto, *Nat. Commun.*, **2013**, *4*, 2390.
[53] S. Yang, L. Peng, P. Huang, X. Wang, Y. Sun, C. Cao, W. Song, *Angew. Chem. Int. Ed.* **2016**, *55*, 4016.
[54] J. Qu, C. Geng, S. Lv, G. Shao, S. Ma, M. Wu, *Electrochim. Acta*, **2015**, *176*, 982.
[55] Y. Chang, F. Hong, C. He, Q. Zhang, J. Liu, *Adv. Mater.* 2013, **25**, 4794.
[56] X. Yu, M. Zhang, J. Chen, Y. Li, G. Shi, *Adv. Energy Mater.* **2016**, *6*, 1501492.
[57] K. Gong, F. Du, Z. Xia, M. Durstock, L. Dai, *Science*, **2009**, *323*, 760.
[58] L. Qu, Y. Liu, J.-B. Baek, L. Dai, *ACS Nano*, **2010**, *4*, 1321.
[59] G. Xu, B. Ding, J. Pan, J. Han, P. Nie, Y. Zhu, Q. Sheng, H. Dou, *J. Mater. Chem. A* **2015**, *3*, 23268.
[60] T. Y. Ma, J. Ran, S. Dai, M. Jaroniec, S. Z. Qiao, *Angew. Chem. Int. Ed.* **2015**, *54*, 4646.
[61] S. Guo, Z. Deng, M. Li, B. Jiang, C. Tian, Q. Pan, H. Fu, *Angew. Chem. Int. Ed.* **2016**, *55*, 1830.
[62] Y. Zhang, T. Mori, J. Ye, M. Antonietti, *J. Am. Chem. Soc.* **2010**, *132*, 6294.
[63] J. P. Paraknowitsch, A. Thomas, *Energy Enviorn. Sci.* **2013**, *6*, 2839.
[64] G. Liu, P. Niu, C. Sun, S. C. Smith, Z. Chen, G. Q. Lu, H.-M.

Cheng, *J. Am. Chem. Soc.* **2010**, *132*, 11642.

[65] J. Zhang, J. Sun, K. Maeda, K. Domen, P. Liu, M. Antonietti, X. Fu, X. Wang, *Energy Enviorn. Sci.* **2011**, *4*, 675.

[66] S. Sergey, Z. Sebastian, *J. Phys. Conden. Matter*, **2013**, *25*, 085507.

[67] Y. Wang, H. Li, J. Yao, X. Wang, M. Antonietti, *Chem. Sci.* **2011**, *2*, 446.

[68] Y. Wang, J. Zhang, X. Wang, M. Antonietti, H. Li, *Angew. Chem. Int. Ed.* **2010**, *49*, 3356.

[69] L. Yang, S. Jiang, Y. Zhao, L. Zhu, S. Chen, X. Wang, Q. Wu, J. Ma, Y. Ma, Z. Hu, *Angew. Chem. Int. Ed.* **2011**, *50*, 7132.

[70] S. Wang, E. Iyyamperumal, A. Roy, Y. Xue, D. Yu, L. Dai, *Angew. Chem. Int. Ed.* **2011**, *50*, 11756.

[71] Q. Han, C. Hu, F. Zhao, Z. Zhang, N. Chen, L. Qu, *J. Mater. Chem. A* **2015**, *3*, 4612.

[72] G. Zhang, M. Zhang, X. Ye, X. Qiu, S. Lin, X. Wang, *Adv. Mater.* **2014**, *26*, 805.

[73] X. Liu, L. Dai, *Nat. Rev. Mater.* **2016**, *1*, 16064.

[74] S. Wang, D. Yu, L. Dai, *J. Am. Chem. Soc.* **2011**, *133*, 5182.

[75] I.-Y. Jeon, Y.-R. Shin, G.-J. Sohn, H.-J. Choi, S.-Y. Bae, J. Mahmood, S.-M. Jung, J.-M. Seo, M.-J. Kim, D. Wook Chang, L. Dai, J.-B. Baek, *Proc. Natl. Acad. Sci. U.S.A.* **2012**, *109*, 5588.

[76] Y. Zheng, Y. Jiao, Y. Zhu, L. H. Li, Y. Han, Y. Chen, A. Du, M. Jaroniec, S. Z. Qiao, *Nat. Commun.* **2014**, *5*, 3783.

[77] Y. Jiang, L. Yang, T. Sun, J. Zhao, Z. Lyu, O. Zhuo, X. Wang, Q. Wu, J. Ma, Z. Hu, *ACS Catal.* **2015**, *5*, 6707.

[78] Y. Xue, J. Liu, H. Chen, R. Wang, D. Li, J. Qu, L. Dai, *Angew. Chem. Int. Ed.* **2012**, *51*, 12124.

[79] B. Kumar, M. Asadi, D. Pisasale, S. Sinha-Ray, B. A. Rosen, R. Haasch, J. Abiade, A. L. Yarin, A. Salehi-Khojin, *Nat. Commun.*

**2013**, *4*, 2819.

[80] I. Y. Jeon, S. Zhang, L. Zhang, H. J. Choi, J. M. Seo, Z. Xia, L. Dai, J. B. Baek, *Adv. Mater.* **2013**, *25*, 6138.

[81] L. Zhang, Z. Xia, *J. Phys. Chem. C* **2011**, *115*, 11170.

[82] X. Li, X. Pan, L. Yu, P. Ren, X. Wu, L. Sun, F. Jiao, X. Bao, *Nat. Commun.* **2014**, *5*, 3688.

[83] J. Zhang, L. Qu, G. Shi, J. Liu, J. Chen, L. Dai, *Angew. Chem. Int. Ed.* **2016**, *55*, 2230.

[84] D. Guo, R. Shibuya, C. Akiba, S. Saji, T. Kondo, J. Nakamura, *Science*, **2016**, *351*, 361.

[85] J. Masa, W. Xia, M. Muhler, W. Schuhmann, *Angew. Chem. Int. Ed.* **2015**, *54*, 10102.

[86] Y. Jiao, Y. Zheng, M. Jaroniec, S. Z. Qiao, *Chem. Soc. Rev.* **2015**, *44*, 2060.

[87] D. Y. Chung, K. J. Lee, S.-H. Yu, M. Kim, S. Y. Lee, O.-H. Kim, H.-J. Park, Y.-E. Sung, *Adv. Energy Mater.* **2015**, *5*, 1401309.

[88] A. Mahmood, W. Guo, H. Tabassum, R. Zou, *Adv. Energy Mater.* **2016**, *6*, 1600423.

[89] S.-L. Li, Q. Xu, *Energy Enviorn. Sci.* **2013**, *6*, 1656.

[90] H. B. Tao, H. B. Yang, J. Chen, J. Miao, B. Liu, *Beilstein J. Nanotech.* **2014**, *5*, 770.

[91] S.-N. Zhao, X.-Z. Song, S.-Y. Song, H.-j. Zhang, *Coordin. Chem. Rev.* **2017**, *337*, 80.

[92] L.-F. Chen, Z.-H. Huang, H.-W. Liang, H.-L. Gao, S.-H. Yu, *Adv. Funct. Mater.* **2014**, *24*, 5104.

[93] Y. Shi, G. Yu, *Chem. Mater.* **2016**, *28*, 2466.

[94] Y. Huang, H. Li, Z. Wang, M. Zhu, Z. Pei, Q. Xue, Y. Huang, C. Zhi, *Nano Energy*, **2016**, *22*, 422.

[95] A. Laforgue, P. Simon, C. Sarrazin, J.-F. Fauvarque, *J. Power Sources*, **1999**, *80*, 142.

[96] S. Glenis, M. Benz, E. LeGoff, J. L. Schindler, C. R. Kannewurf, M. G. Kanatzidis, *J. Am. Chem. Soc.***1993**, *115*, 12519.

[97] X. Chen, J. Zhang, X. Fu, M. Antonietti, X. Wang, *J. Am. Chem. Soc.* **2009**, *131*, 11658.

[98] F. Su, S. C. Mathew, G. Lipner, X. Fu, M. Antonietti, S. Blechert, X. Wang, *J. Am. Chem. Soc.* **2010**, *132*, 16299.

[99] J. Hong, X. Xia, Y. Wang, R. Xu, *J. Mater. Chem.* **2012**, *22*, 15006.

[100] G. Zhang, J. Zhang, M. Zhang, X. Wang, *J. Mater. Chem.* **2012**, *22*, 8083.

[101] Y. Zheng, J. Liu, J. Liang, M. Jaroniec, S. Z. Qiao, *Energy Enviorn. Sci.* **2012**, *5*, 6717.

[102] G. Dong, Y. Zhang, Q. Pan, J. Qiu, *J. Photochem. Photobio. C Photochem. Rev.* **2014**, *20*, 33.

[103] S. Cao, J. Low, J. Yu, M. Jaroniec, *Adv. Mater.* **2015**, *27*, 2150.

[104] S. Lin, X. Ye, X. Gao, J. Huang, *J. Molecular Catal. A Chem.* **2015**, *406*, 137.

[105] X. Dong, F. Cheng, *J. Mater. Chem. A* **2015**, *3*, 23642.

[106] Z. Zhao, Y. Sun, F. Dong, *Nanoscale*, **2015**, *7*, 15.

[107] Y. Zheng, L. Lin, B. Wang, X. Wang, *Angew. Chem. Int. Ed.* **2015**, *54*, 12868.

[108] V. W.-h. Lau, I. Moudrakovski, T. Botari, S. Weinberger, M. B. Mesch, V. Duppel, J. Senker, V. Blum, B. V. Lotsch, *Nat. Commun.* **2016**, *7*, 12165.

[109] J. Liu, H. Wang, M. Antonietti, *Chem. Soc. Rev.* **2016**, *45*, 2308.

[110] X. Wang, K. Maeda, A. Thomas, K. Takanabe, G. Xin, J. M. Carlsson, K. Domen, M. Antonietti, *Nat. Mater*, **2009**, *8*, 76.

[111] A. Schwarzer, T. Saplinova, E. Kroke, *Coordin. Chem. Rev.* **2013**, *257*, 2032.

[112] W. Xia, A. Mahmood, R. Zou, Q. Xu, *Energy Enviorn. Sci.* **2015**,

*8*, 1837.

[113] B. Li, H.-M. Wen, Y. Cui, W. Zhou, G. Qian, B. Chen, *Adv. Mater.* **2016**, *28*, 8819.

[114] D. Sheberla, J. C. Bachman, J. S. Elias, C.-J. Sun, Y. Shao-Horn, M. Dincă, *Nat. Mater.* **2016**, *16*, 220.

[115] K. Shen, X. Chen, J. Chen, Y. Li, *ACS Catal.* **2016**, *6*, 5887.

[116] F. R. Fortea-Pérez, M. Mon, J. Ferrando-Soria, M. Boronat, A. Leyva-Pérez, A. Corma, J. M. Herrera, D. Osadchii, J. Gascon, D. Armentano, E. Pardo, *Nat. Mater.* **2017**, *16*, 760.

[117] T. Kitao, Y. Zhang, S. Kitagawa, B. Wang, T. Uemura, *Chem. Soc. Rev.* **2017**, *46*, 3108.

[118] J. Liu, D. Zhu, C. Guo, A. Vasileff, S.-Z. Qiao, *Adv. Energy Mater.* **2017**, *7*, 1700518.

[119] I. Stassen, N. Burtch, A. Talin, P. Falcaro, M. Allendorf, R. Ameloot, *Chem. Soc. Rev.* **2017**, *46*, 3185.

[120] M.-S. Yao, X.-J. Lv, Z.-H. Fu, W.-H. Li, W.-H. Deng, G.-D. Wu, G. Xu, *Angew. Chem. Int. Ed.* **2017**, *56*, 16510.

[121] A. T. Swesi, J. Masud, M. Nath, *Energy Enviorn. Sci.* **2016**, 9, 1771.

[122] L. Trotochaud, S. W. Boettcher, *Scri. Mater.* **2014**, *74*, 25.

[123] C. C. L. McCrory, S. Jung, J. C. Peters, T. F. Jaramillo, *J. Am. Chem. Soc.* **2013**, *135*, 16977.

[124] T. Y. Ma, S. Dai, M. Jaroniec, S. Z. Qiao, *Angew. Chem. Int. Ed.* **2014**, *53*, 7281.

[125] J. Zhang, Z. Zhao, Z. Xia, L. Dai, *Nat. Nanotech.* **2015**, *10*, 444.

[126] Y. Deng, Y. Xie, K. Zou, X. Ji, *J. Mater. Chem. A* **2016**, *4*, 1144.

[127] E. Raymundo-Piñero, K. Kierzek, J. Machnikowski, F. Béguin, *Carbon*, **2006**, *44*, 2498.

[128] J. Chmiola, G. Yushin, Y. Gogotsi, C. Portet, P. Simon, P. L. Taberna, *Science*, **2006**, *313*, 1760.

[129] J. Huang, B. G. Sumpter, V. Meunier, *Chem. Eur. J.* **2008**, *14*, 6614.

[130] S. Zhang, N. Pan, *Adv. Energy Mater.* **2015**, *5*, 1401401.

[131] T. Lin, I.-W. Chen, F. Liu, C. Yang, H. Bi, F. Xu, F. Huang, *Science*, **2015**, *350*, 1508.

# Chapter 2. Robust Water Oxidation Electrocatalyst from Sulfur-Modified Graphitic Carbon Nitride Nanostructures

## 2.1 Introduction

Oxygen evolution reaction (OER) has been a main focus of scientists working in the field of energy harvesting to convert water into oxygen. The importance of OER lies in the mechanisms of catalytic oxygen evolution for clean and sustainable fuel cells, rechargeable metal-air batteries, and solar fuel production (water splitting). Traditionally, OER has been catalyzed by expensive, rare earth metals, such as Ru and Ir (oxide).[1] Inexpensive metal/metal oxide composites, including Co, Mn, Fe, and Ni-based systems, have been used as alternatives, but low conductivity limits their practical applications.[2-11] Great efforts have been made to find alternatives based on non-metal systems, particularly carbon-based nanomaterials.[12-15] Graphitic carbon nitride (g-$C_3N_4$) is reported to exhibit good electrocatalytic activities originating from the pyridinic and pyrrolic nitrogen in the carbon framework, and has been

successfully used as supports or composite materials in many catalytic or photocatalytic reactions.[16-27] Moreover, the low production cost, high thermal and chemical stability, environmental harmlessness, and easy scalability of g-$C_3N_4$ have attracted increasing attention in recent years.[28-44] To increase the conductivity or catalytic properties of g-$C_3N_4$, various strategies have been developed, such as nanostructuring,[45-50] making composites with other conducting carbon materials,[51-58] and doping or modification with heteroatom such as P,[22,35] B,[23,44] I,[59-60] F,[61] and S.[62-66] Although the heteroatom modified/mediated structures are not well defined and the exact position of dopant is not well understood yet, the enhancement of photocatalytic activity in g-$C_3N_4$ nanostructures is significant.[44,59,67] OER is considered to be a complicated process involving four-electron transfer with a sluggish reaction rate that always suffers from a high overpotential, leading to huge energy losses in practical applications. Though some g-$C_3N_4$ nanomaterials have been reported to be OER active, achieving low overpotentials in the OER process is still a great challenge. [33,35,68-69]

Herein, sulfur-modified g-$CN_x$ nano-electrocatalysts were successfully synthesized from melamine nanogeodes (MNGs) by *in situ* modification with sulfur and subsequent annealing. The unique MNGs were

synthesized by a very simple hydrothermal method, inspired by the synthesis and morphology of natural geodes. S-modified g-$CN_x$ nanostructures show excellent OER activity with the lowest overpotential of 290 mV at a current density of 10 mA $cm^{-2}$. Moreover, a long durability of 91.2% retention for 18 h is achieved, which is essential for electrocatalysts. This result is, to date, the best performance realized among non-metal based electrocatalysts. The modification of g-$CN_x$ nanostructures with sulfur greatly reduces the overpotential for the OER process and results in an efficient electrocatalyst with long-term durability.

## 2.2. Experimental Section

### 2.2.1 Synthesis of Melamine Nanogeodes

Melamine and sulfur were purchased from Sigma-Aldrich and used as received. Novel MNGs were synthesized by a simple hydrothermal method. Typically, 0.5 g melamine was dissolved in 75 mL of D. I. water at a slightly higher temperature of 50 °C. After dissolution of melamine, the solution was transferred to a 100 mL Teflon-lined stainless steel autoclave. An electric oven was used to heat the autoclave for 24 h at 160 °C. After completion of the reaction, the reaction mixture was allowed to cool naturally to room temperature. The reaction product was carefully collected and centrifuged at 10,000 rpm for 30 min. The upper fraction was assumed to contain the MNGs and was collected. The MNGs were recovered in powder form by evaporating the water with a rotavapor.

### 2.2.2 Synthesis of Graphitic Carbon Nitride Nanostructures

The g-$CN_x$ nanostructures were prepared using 1.0 g of the MNG powder obtained using the above procedure. Two-step heating of the powder in a high-quality alumina crucible with a lid was conducted under an argon atmosphere at a gas flow rate of 100 sccm. In the first

step, the powder was heated from room temperature to 400 °C at a heating rate of 4.4 °C $min^{-1}$ and held for 1 h 30 min. In the second step, the powder was further heated to 600 °C at the same heating rate of 4.4 °C $min^{-1}$ and held for 2 h. After the heating procedure, the sample was allowed to cool naturally to room temperature, and the final product was collected as g-$CN_x$ nanostructures in powder form.

### 2.2.3 Synthesis of Sulfur-Modified Graphitic Carbon Nitride Nanostructures

S-modified g-$CN_x$ nanostructures in powder form were prepared using 0.5 g of sulfur and 1.0 g of MNG powder, thoroughly mixed with a mortar and pestle followed by the two-step heating process described above. Various S-modified g-$CN_x$ catalysts were obtained by varying the initial amount of sulfur (0.125, 0.25, 0.5, or 1.0 g) to 1 g of MNG powder.

### 2.2.4 Synthesis of bulk graphitic carbon nitride

Bulk graphitic carbon nitride was prepared by using 1.0 g commercial melamine as a precursor and the two-step heating process described above. The final product was collected as bulk graphitic carbon nitride in powder form.

### 2.2.5 Synthesis of Sulfur Mediated Bulk Graphitic Carbon Nitride

Initially 0.5 g of sulfur and 1.0 g of melamine powder thoroughly mixed with a mortar and pestle followed by the two-step heating process described in the main text. The final product was collected as sulfur mediated bulk graphitic carbon nitride in powder form.

### 2.2.6 Electrochemical Cell Preparation and Measurements

The preparation procedure for the working electrode was as follows. The catalyst ink was prepared using g-$CN_x$ catalyst, carbon black (Super P®), and polyvinylidene fluoride (PVDF) (8:1:1) in N-methyl-2-pyrrolidone. The catalyst ink (10 μL) was deposited on a glassy carbon tip (5 mm diameter) and dried at 120 °C. The electrochemical measurements were performed in a three-electrode cell using an electrochemical analyzer (CHI 760E, CH Instruments, Inc.). A Pt ring was used as the counter electrode, and a Ag/AgCl/3M NaCl electrode was used as the reference electrode. A graphite counter electrode was also used and the CV response result was same as the CV response using Pt counter electrode (Figure 2.15). The electrodes were evaluated from pH 6 to 12 in phosphate buffered saline solution buffered using KOH, and from pH 12 to 14 in aqueous KOH and $NaClO_4$ buffered using KOH.

The ionic strength of all electrolytes was maintained at 1 M. The reference electrode was carefully calibrated with respect to RHE at 25 °C. The RHE was calibrated to -0.201 V vs. the Ag/AgCl reference electrode. For the electrochemical study, a rotating disk electrode (RDE) system was used (PINE Inc.) with a glass carbon tip (5 mm diameter). The RDE measurements were performed at a rotation speed of 2,000 rpm and a scan rate of 5 mV $s^{-1}$. The current densities were obtained based on the geometry surface area of the working electrode in the electrolyte (0.196 $cm^2$ for the glassy carbon tip). The measured potentials were corrected for the ohmic potential drop (iR) losses that originate from the resistance of the interface between the substrate and the electrolyte. Resistances were measured using iR compensation mode in the electrochemical analyzer. Analyzing the impedance spectroscopy reveals that the resistances of the bare glassy carbon electrode, bulk g-$CN_x$, g-$CN_x$ nanostructures, S-modified g-$CN_x$ nanostructures are 7.0 Ω, 10.0 Ω, 7.3 Ω, and 7.1 Ω, respectively and, the degree of iR compensation is 100%.

### 2.2.7 Physicochemical Characterization

TEM analysis was performed using an aberration-corrected TEM (Titan G2 Cube 60-300 kV, FEI). The samples were mounted on Quantifoil

mesh grids. To minimize exposure of the sample to the beam, the image was collected at a low operating voltage (80 kV) with a least beam exposure approach. The scanning transmission electron microscopy (STEM) imaging and EELS mapping were carried out on a FEI Titan cubed G2 electron microscope operated at 80 kV equipped with a monochromator. A probe size of 1.5 Å and a best energy resolution of 0.2 ± 0.05 eV, as measured from the full-width-at-half-maximum of the zero-loss peak, were achieved. For simultaneous EELS mapping of the *K*-edge structures for carbon and nitrogen, and *L*-edge structure for sulfur, a 5 mm spectrometer entrance aperture and 0.25 eV per channel dispersion were used. Synchrotron HRPD measurements were performed at the 9B beamline of Pohang Accelerator Laboratory (PAL, Pohang, Republic of Korea), the incident X-ray source was vertically collimated by mirror and monochromatized to $\lambda$=1.4863 Å by a double-crystal Si(111) monochromator (DCM). X-ray photoelectron spectroscopy (XPS) analysis were performed in an UHV multipurpose surface analysis system (Sigma Probe, Thermo, UK) operating at base pressures $<10^{-9}$ mbar, and the HRPES end-station at 10D beamline of PAL. Fourier transform infrared (FT-IR) spectra was collected using a TENSOR27/Bruker instrument.

## 2.3 Result and Discussion

### 2.3.1 Synthesis and Characterization of Electrocatalysts

Unique melamine nanogeodes (MNGs) were used as starting materials for the synthesis of g-$CN_x$ nanostructures and S-modified g-$CN_x$ nanostructures. The synthesis and morphology of MNGs is inspired by natural geodes found in the earth's crust, which are formed under high temperature and pressure in liquids (Figure 2.1a). To achieve similar reaction conditions, a hydrothermal method, which is a well-established, simple, and cost-effective method, is used to synthesize MNGs from cheap melamine in environmentally friendly aqueous medium. The stepwise synthesis of MNGs in solution is shown schematically in Figure 2.1b (i–iv). After the hydrothermal reaction, MNGs are obtained by centrifugation of the reaction mixture. Owing to their lower density, MNGs remain in the upper fraction, which is carefully separated from the residue. The MNGs can be acquired as a powder by evaporating the solvent. Low-magnification transmission electron microscope (TEM) image in Figure 2.1c shows the morphology of the MNGs. The high resolution transmission electron microscope (HRTEM) images in Figure 2.1d and e show that the MNGs are multiwalled with polygonal shapes,

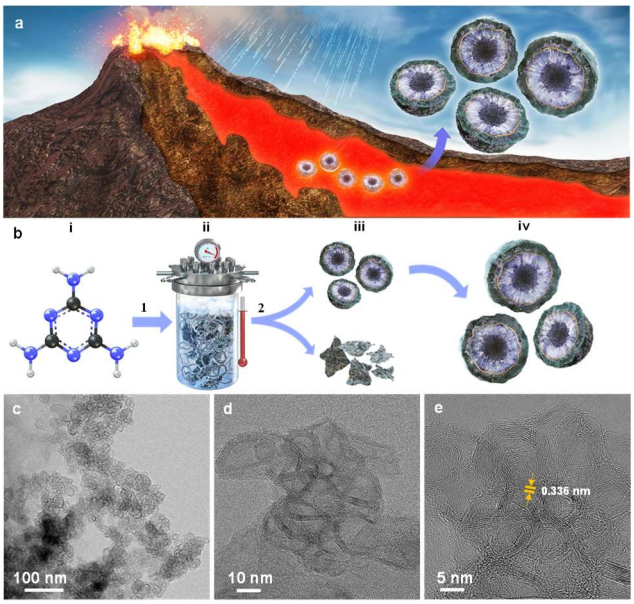


**Figure 2.1** Synthesis of melamine nanogeodes. (a) Schematic representation of the synthesis process for naturally occurring geodes in the earth's crust. (b) The precursor melamine (i) in an aqueous solution is used to synthesize melamine nanogeodes (MNGs) under the hydrothermal conditions of 160 °C for 24 h in step (1). After completion of the hydrothermal reaction, the reaction mixture (ii) of MNGs mixed with a residue is centrifuged in step (2) to separate the lighter density MNGs from the higher density residue (iii). Representative images of MNGs (iv). (c) TEM image of MNGs. (d and e) HRTEM images of MNGs showing multiwalled closed cage structures with an interlayer distance of 0.336 nm.

similar to natural geodes. The MNGs are ~10-20 nm in diameter and each nanogeode has a closed-cage structure with 8-10 multilayers and an interlayer spacing of 0.336 nm. To obtain S-modified g-$CN_x$ nanostructures, typically 0.5 g sulfur powder is mixed thoroughly with 1.0 g MNG powder using a mortar and pestle, and then the mixture is annealed in argon atmosphere. In the absence of sulfur, g-$CN_x$ nanostructures are produced in a similar way. Under similar conditions, two step thermal annealing of commercial melamine without formation of MNGs results in the synthesis of bulk g-$CN_x$, which is used as the reference sample. The S-modified g-$CN_x$ nanostructures were further characterized by TEM elemental analysis (Figure 2.2). For comparison, the g-$CN_x$ nanostructures without sulfur were similarly analyzed (Figure 2.3). As shown in the TEM and HRTEM images, the morphologies of the S-modified g-CNx nanostructures (Figure 2.2a and b) and the g-$CN_x$ nanostructures (Figure 2.3a and b) are similar, which implies that sulfur modification does not affect the morphology. High-angle annular dark field scanning TEM (HAADF-STEM) combined with electron energy loss spectroscopy (EELS) was used to characterize the elemental distribution in S-modified g-$CN_x$ nanostructures (Figure 2.2c). The spatial distributions of the various elements were visualized by EELS

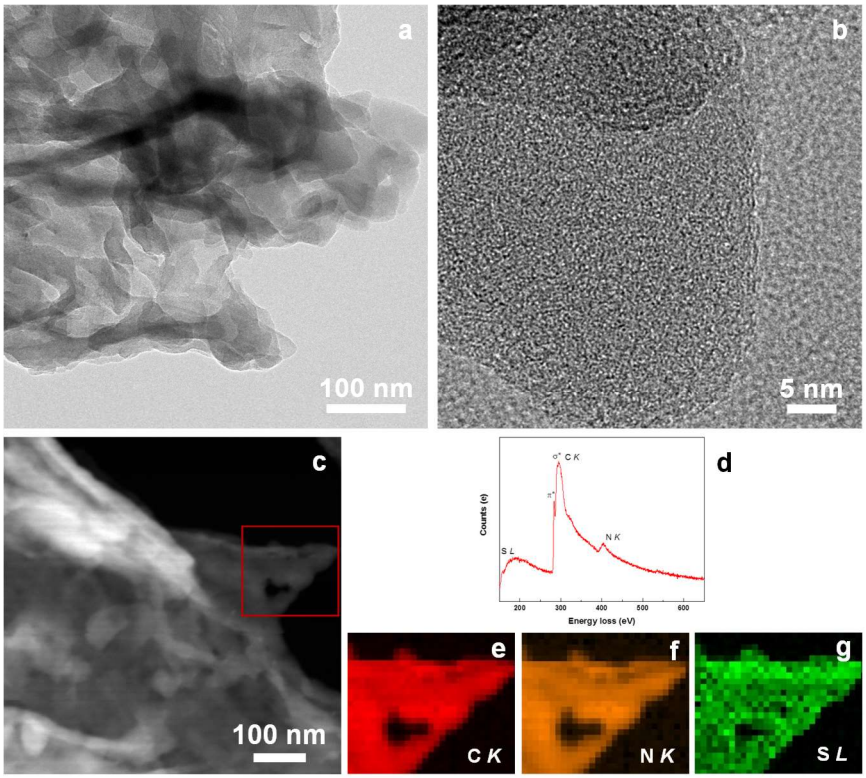


**Figure 2.2** Electron microscopy characterization of S-modified g-$CN_x$ nanostructures. (a) TEM and (b) HRTEM images, respectively. (c) High-angle annular dark field scanning TEM image. (d) EELS spectra collected at the site indicated in c. (e-g) EELS elemental maps obtained from the site indicated by the red box in c: (e) C-*K* edge, (f) N-*K* edge, and (g) S-$L_{2,3}$ edge.

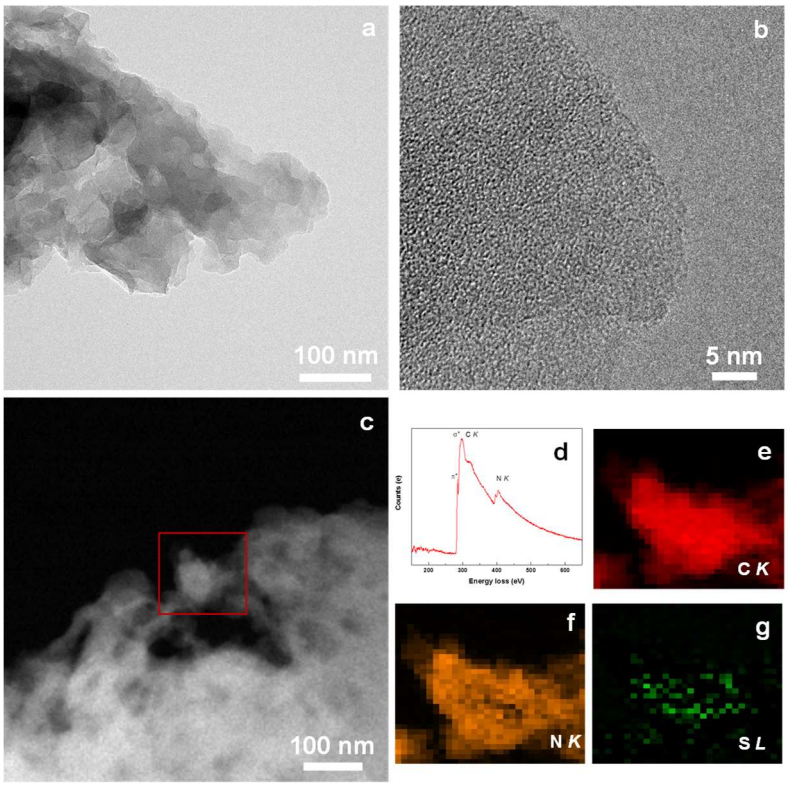


**Figure 2.3** Electron microscopy characterization of g-$CN_x$ nanostructures. (a and b) TEM and HRTEM images, respectively. (c) High-angle annular dark field scanning TEM image. (d) EELS spectra collected at the site indicated in c. (e and f) EELS elemental maps obtained from the site indicated by the red box in c: (e) C-*K* edge, (f) N-*K* edge and (g) S-*L* edge (indicates noise level signals only).

mapping based on the intensity variation of the energy loss peaks (Figure 2.2d). The EELS spectrum of the area marked with a red box in Figure 2.2c clearly shows an S-*L* edge along with C-*K* and N-*K* edges. The C-*K* edge shows one π* state at 284.75 eV and one σ* state at 292 eV. The N-*K* edge shows combined π* and σ* states at 403 eV. The peak observed at 165.7 eV due to the S-$L_{2,3}$ edge is not observed in the spectrum for g-$CN_x$ nanostructures without sulfur-modification (see Figure 2.2d and 2.3d for comparison). This significant EELS elemental peak, along with the elemental mapping images shown in Figure 2.2e-g for the C-*K* edge, N-*K* edge and S-$L_{2,3}$ edge spectra, respectively, clearly indicate the presence of sulfur in S-modified g-$CN_x$ nanostructures. Whereas elemental mapping image of g-$CN_x$ nanostructures is shown in Figure 2.3e, f for the C-*K* edge, N-*K* edge spectra respectively, Figure 2.3g for S-$L_{2,3}$ edge spectra shows noise level. The synthesis and graphitic nature of carbon nitride is also confirmed by high resolution synchrotron powder diffraction (HRPD) analysis of bulk g-$CN_x$, g-$CN_x$ nanostructures, and S-modified g-$CN_x$ nanostructures. The HRPD spectra in Figure 2.4a show two prominent peaks. The strong peak at 2θ = 26.5° arises from the (002) interlayer diffraction of the fundamental carbon nitride structure (d = 0.326 nm), whereas the second peak at 2θ =

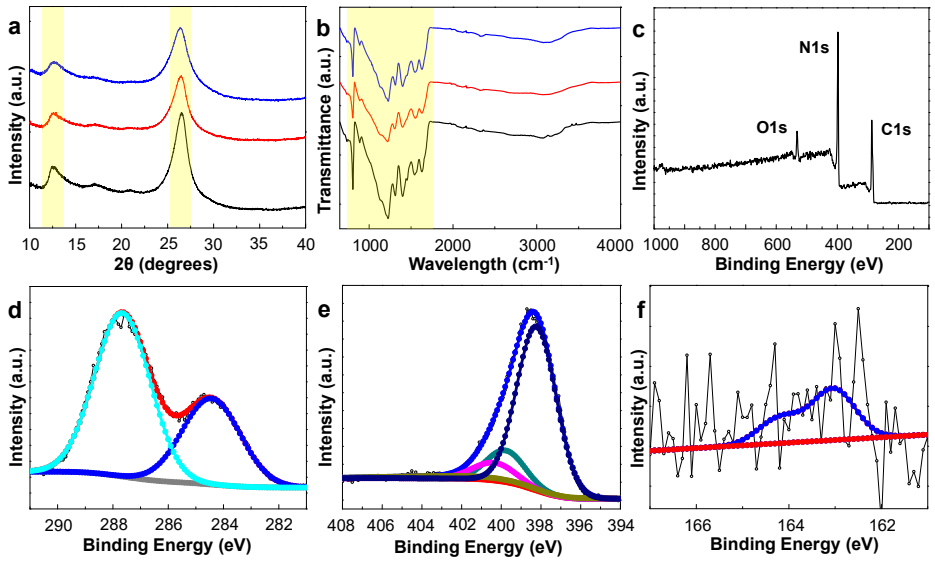


**Figure 2.4** Structural characterization of electrocatalysts. Comparisons of (a) HRPD and (b) FT-IR spectra of bulk g-$CN_x$ (black), g-$CN_x$ nanostructures (red), and S-modified g-$CN_x$ nanostructures (blue). (c) Widescan XPS spectra, (d) C1s, (e) N1s and (f) S2p XPS spectra of S-modified g-$CN_x$ nanostructures.

12.5° is considered to correspond to the in-plane repeating units of tri-s-triazine (d = 0.663 nm). Furthermore, the chemical nature and bonding structures of the g-$CN_x$ materials were investigated by Fourier transform infrared (FT-IR) spectroscopy, as shown in Figure 2.4b. The sharp peak at 810 $cm^{-1}$ is correspond to the breathing mode of the tri-s-triazine units. The multiple bands observed in the range of 900-1800 $cm^{-1}$ are typical of the CN heterocyclic structures present in the carbon nitride structure. The broad peak at 2900-3600 $cm^{-1}$ is an enhanced adsorption due to N-H stretches. The C, N, and S elements in the S-modified g-$CN_x$ nanostructures is characterized by X-ray photoelectron spectroscopy (XPS), and the widescan XPS spectra is shown in Figure 2.4c. The C1s core-level XPS data of S-modified g-$CN_x$ nanostructures in Figure 2.4d shows two peaks centered at 284.5 and 287.7 eV. The first peak at 284.5 eV is due to $sp^2$ C-C bonds and the peak at 287.7 eV is due to $sp^2$ bonded carbon with N in aromatic rings (N-C=N). The N1s core-level XPS data of S-modified g-$CN_x$ nanostructures in Figure 2.4e shows four peaks centered at 398.3, 399.9, 400.5, and 403.7 eV. The intense peak at 398.3 eV is due to the $sp^2$ bonded N from the triazine rings (C-N=C), and 399.9 eV for tertiary nitrogen [N-$(C)_3$], the peak at 400.5 eV is for amino functional groups (C-N-H) and the peak at 403.7 eV is due to charging

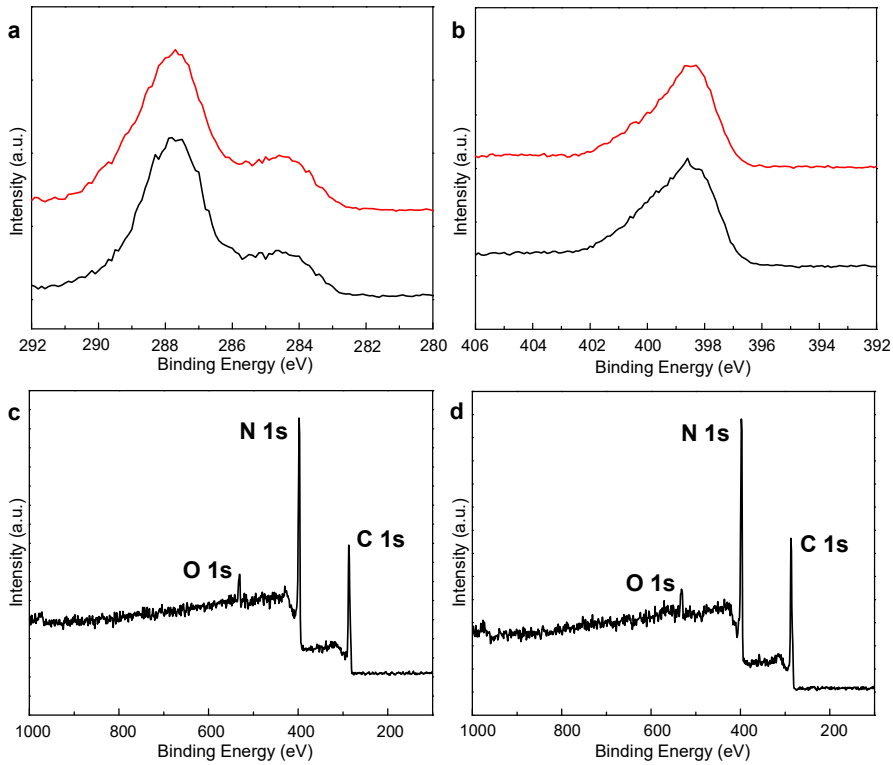


**Figure 2.5** (a) C1s, (b) N1s XPS spectra of bulk g-$CN_x$ (black) and g-$CN_x$ nanostructures (red). Widescan XPS spectra of (c) bulk g-$CN_x$ and (d) g-$CN_x$ nanostructures.

| Sr. No. | Sample Name | Elemental composition by XPS (Atomic %) | | | |
|---|---|---|---|---|---|
| | | C | N | O | S |
| 1 | bulk g-$CN_x$ | 55.05 | 39.18 | 5.77 | - |
| 2 | MNGs | 47.54 | 41.94 | 10.52 | - |
| 3 | g-$CN_x$ nanostructures | 51.52 | 43.71 | 4.77 | - |
| 4 | S-modified g-$CN_x$ nanostructures (S: 0.5 g) | 52.46 | 41.52 | 5.73 | 0.29 |
| 5 | S-modified g-$CN_x$ nanostructures (S: 0.125 g) | 53.79 | 39.12 | 6.91 | 0.18 |
| 6 | S-modified g-$CN_x$ nanostructures (S: 0.25 g) | 52.95 | 40.10 | 6.71 | 0.24 |
| 7 | S-modified g-$CN_x$ nanostructures (S: 1.0 g) | 48.61 | 46.09 | 4.98 | 0.32 |
| 8 | S-mediated bulk g-$CN_x$ | 53.37 | 37.69 | 8.43 | 0.51 |

**Table 2.1** Comparison of elemental analysis.

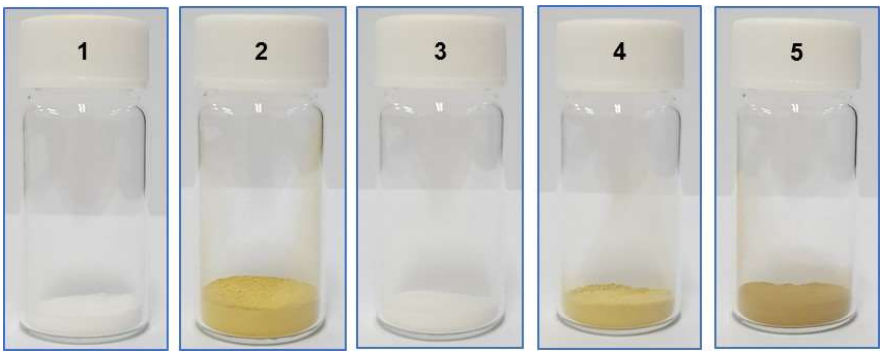


**Figure 2.6** Digital images of (1) commercial melamine powder, (2) bulk g-$CN_x$, (3) MNGs, (4) g-$CN_x$ nanostructures, and (5) S-modified g-$CN_x$ nanostructures in each 10 mL glass vials with cap.

effect. The peaks centered at 163.1 and 164.2 eV shown in Figure 2.4f for S2p core-level XPS data are assigned for S-C bonds, which implies the interaction of sulfur and carbon atoms of the g-$CN_x$ planes.[29,62,65] The details of XPS data for bulk g-$CN_x$ and g-$CN_x$ nanostructures is given in Figure 2.5 and comparison of XPS analysis is given in Table 2.1.

### 2.3.2 OER Activity of the Electrocatalysts

To investigate the electrocatalytic activity of the g-$CN_x$ nano-electrocatalysts, cyclic voltammetry was measured using a rotating disk electrode (RDE) system. The current density vs. potential (*J-E*) curves (Figure 2.7a) obtained from the RDE measurements show that the current density associated with the OER exponentially increases when the potential is swept from 1.0 to 1.95 V vs. RHE. To compare the capability of these materials for OER activity, the potential required to attain a current density of 10 mA $cm^{-2}$ for the OER is defined as overpotential from *J-E* curves (Figure 2.7c; Table 2.2). In addition, RDE measurements of a bulk g-$CN_x$ catalyst as a standard reference sample were obtained. The overpotential to attain a current density of 10 mA $cm^{-2}$ for the OER with g-$CN_x$ nanostructures is 480 mV vs. RHE; this potential is negatively (cathodically) shifted by 200 mV relative to that

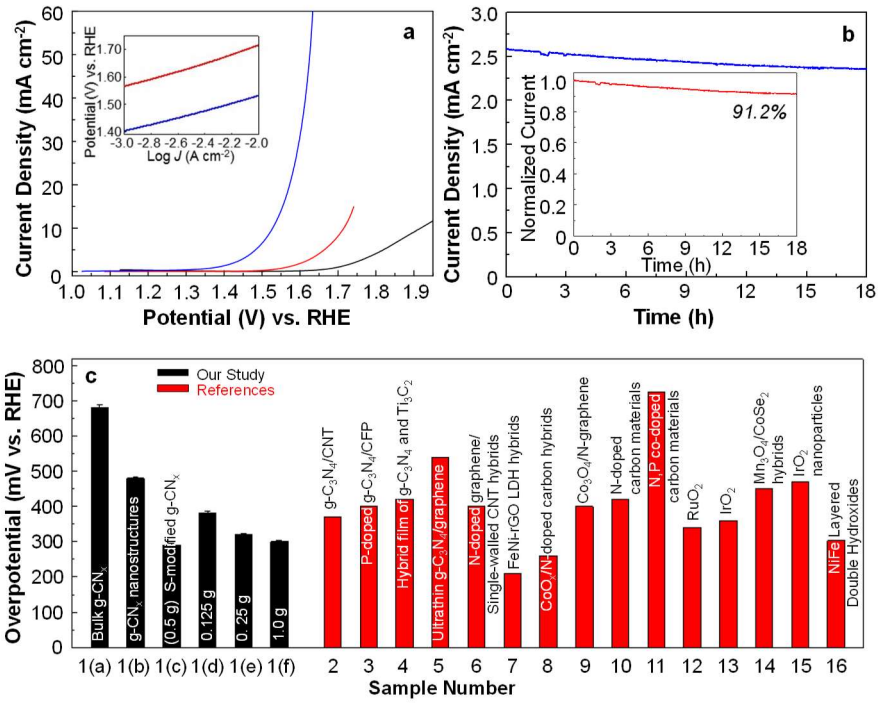


**Figure 2.7** Electrochemical response of g-$CN_x$ catalysts. (a) Current density–potential (*J-E*) curves for bulk g-$CN_x$ (black), g-$CN_x$ nanostructures (red), and S-modified g-$CN_x$ nanostructures (blue). The inset shows the Tafel plots derived from the *J-E* data. (b) Chronoamperometric operation of S-modified g-$CN_x$ nanostructures at the potential of 1.45 V vs. RHE. The inset shows the normalized current density with increasing operation time. (c) Overpotentials of various catalyst samples at 10 mA $cm^{-2}$. Detailed information about the various catalysts can be found in Table 2.2.

| **Sample Number from Figure 2.7** | **Sample** | **V at 10 mA $cm^{-2}$ (V vs. RHE) *(overpotential, η)*** | **References** |
|---|---|---|---|
| **1(a)** | **Bulk g-$CN_x$** | **1.91, pH 14 *(η = 680 mV)*** | **This study** |
| **1(b)** | **g-$CN_x$ nanostructures** | **1.71, pH 14 *(η = 480 mV)*** | |
| **1(c)** | **S-modified g-$CN_x$ nanostructures (S: 0.5 g)** | **1.52, pH 14 *(η = 290 mV)*** | |
| **1(d)** | **S-modified g-$CN_x$ nanostructures (S: 0.125 g)** | **1.61, pH 14 *(η = 380 mV)*** | |
| **1(e)** | **S-modified g-$CN_x$ nanostructures (S: 0.25 g)** | **1.55, pH 14 *(η = 320 mV)*** | |
| 2 | g-$C_3N_4$/CNT | 1.60, pH 14 *(η = 370 mV)* | *Angew. Chem. Int. Ed.* **2014**, *53,* 7281 |
| 3 | P-doped g-$C_3N_4$/CFP | 1.63, pH 13 *(η = 400 mV)* | *Angew. Chem. Int. Ed.* **2015**, *54,* 4646 |
| 4 | Hybrid film of g-$C_3N_4$ and $Ti_3C_2$ | 1.65, pH 13 *(η = 420 mV)* | *Angew. Chem. Int. Ed.* **2016**, *55,* 1138 |
| 5 | Ultrathin g-$C_3N_4$/graphene | 1.769, pH 13 *(η = 539 mV)* | *ChemSusChem.* **2014**, *7,* 2125 |

| | | | |
|---|---|---|---|
| 6 | N-surface doped graphene/single-walled CNT hybrids | 1.63, pH 13 (*η = 400 mV)* | *Small* **2014**, *10,* 2251 |
| 7 | FeNi-rGO LDH hybrids | 1.44, pH 14 (*η = 210 mV)* | *Angew. Chem. Int. Ed.* **2014**, *53,* 7584 |
| 8 | $CoO_x$/N-surface doped carbon hybrids | 1.49, pH 14 (*η = 260 mV)* | *J. Am. Chem. Soc.* **2015**, *137,* 2688 |
| 9 | $Co_3O_4$/N-graphene | 1.63, pH 14 *(η = 400 mV)* | *Nat. Mater.* **2011**, *10,* 780 |
| 10 | N-surface doped carbon materials | 1.65, pH 13 *(η = 420 mV)* | *Nat. Commun.* **2013,**, *4,* 2390 |
| 11 | N, P co-surface doped carbon materials | 1.95, pH 13 *(η = 725 mV)* | *Nat. Nanotech.* **2015**, *10,* 444 |
| 12 | $RuO_2$ | 1.57, pH 14 *(η = 340 mV)* | *Electrochim. Acta.* **2011**, *56,* 2009 |
| 13 | $IrO_2$ | 1.59, pH 14 *(η = 360 mV)* | *Phys. Chem. Chem. Phys.* **2014**, *16,* 3623 |
| 14 | $Mn_3O_4/CoSe_2$ hybrids | 1.68, pH 13 *(η = 450 mV)* | *J. Am. Chem. Soc.* **2012**, *134,* 2930 |
| 15 | $IrO_2$ nanoparticles | 1.70, pH 13 *(η = 470 mV)* | *Chem. Mater.* **2011**, *23,* 3201 |
| 16 | NiFe layered double hydroxides | 1.533, pH 13 *(η = 303 mV)* | *Nat. Commun.* **2014**, *5,* 4477 |

**Table 2.2** Comparison of overpotentials of catalysts at 10 mA $cm^{-2}$

for the bulk g-$CN_x$ catalyst. The OER properties of the g-$CN_x$ nanostructures are further enhanced by sulfur modification. Tuning and optimization of the amount of S-modification allows the OER activity to be increased by lowering the overpotential (Figure 2.7a; Figure 2.8). Interestingly, the *J-E* curve for the S-modified g-$CN_x$ nanostructures shows the largest negative shift with an overpotential at 10 mA $cm^{-2}$ of 290 mV vs. RHE, indicating a negative shift of 190 mV compared with that of unmodified g-$CN_x$ nanostructures. To the best of our knowledge, this value is the lowest among g-$CN_x$ OER catalysts reported to date and is comparable to those of the best-performing metal-based catalysts (see Table 2.2). We varied the amount of initial sulfur (0.125, 0.25, 0.5, and 1.0 g) with 1.0 g of MNG to tune sulfur loading of the electrocatalysts and confirmed that the elemental composition of sulfur is 0.18, 0.24, 0.29, and 0.32 at%, respectively (Table 2.1). The electrocatalytic performance exhibits dependency on the initial amount of sulfur used. The overpotentials (η) are 380, 320, 290, and 300 mV for the electrocatalysts prepared using 0.125, 0.25, 0.5, and 1.0 g of sulfur, respectively (Figure 2.8). The best performance (η=290 mV) is achieved for the electrocatalyst prepared using 0.5 g of sulfur, designated as S-modified g-$CN_x$ nanostructures. The S-mediated bulk g-CNx catalyst has been

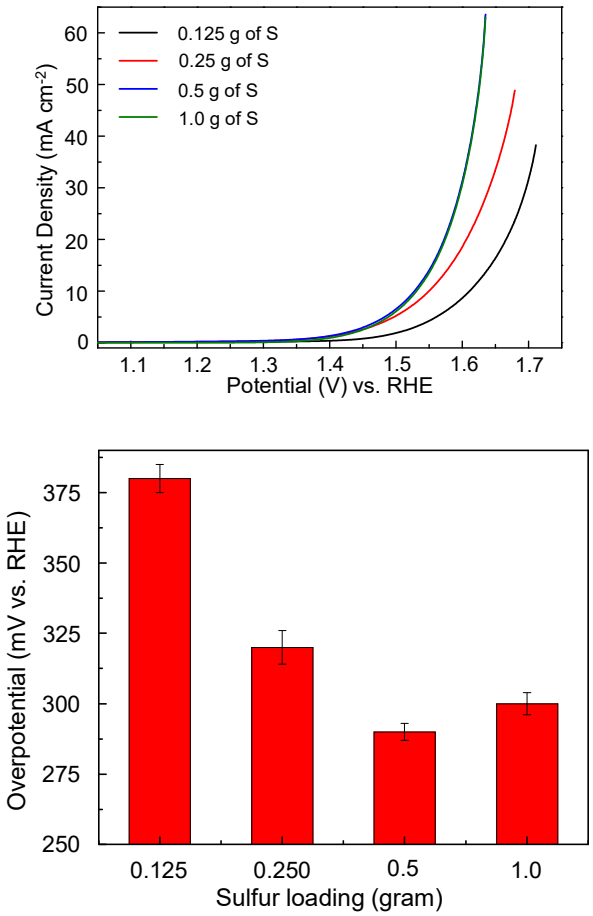


**Figure 2.8** Electrochemical response of S-modified g-$CN_x$ catalysts. *J-E* curves of S-modified g-$CN_x$ nanostructures and their overpotential at 10 $mAcm^{-2}$. During synthesis, the amount of S was varied from 0.125 to 1 g for 1 g of MNGs.

synthesized in the same way, except that commercial melamine is used instead of MNG powder. The lower activity of S-mediated bulk g-$CN_x$ catalysts shows the importance of MNGs for the synthesis of the electrocatalyst (Figure 2.9). We also varied annealing temperature during calcination step for the synthesis of S-modified g-$CN_x$ nanostructures and confirmed the sample annealed at 600 °C showed the best OER activity (Figure 2.10).

To measure an electrochemically active surface area (ECSA), a capacitance of an electrical double layer (Cdl) at a solid/electrolyte interface was evaluated by measuring the *J-E* response of the g-$CN_x$ nanostructures and the S-modified g-$CN_x$ nanostructures on the glassy carbon electrode at various scan rates (Figure 2.11). The Cdl is estimated from the slope of the plot of $J_C$, which is the current at the potential with a net current density of 0 μA $cm^{-2}$ increasing the scan rate from 20 mV $sec^{-1}$ to 100 mV $sec^{-1}$. The capacitance is 237.5 μF $cm^{-2}$ for S-modified g-$CN_x$ nanostructures and 145.0 μF $cm^{-2}$ for g-$CN_x$ nanostructures, respectively. Values are much higher than that of typical compact flat electrode reported to date (10-20 μF $cm^{-2}$).[70] The slope is also proportional to the exchange current density, which is directly related to the catalytically active surface area.[71-72] The ECSA is calculated from

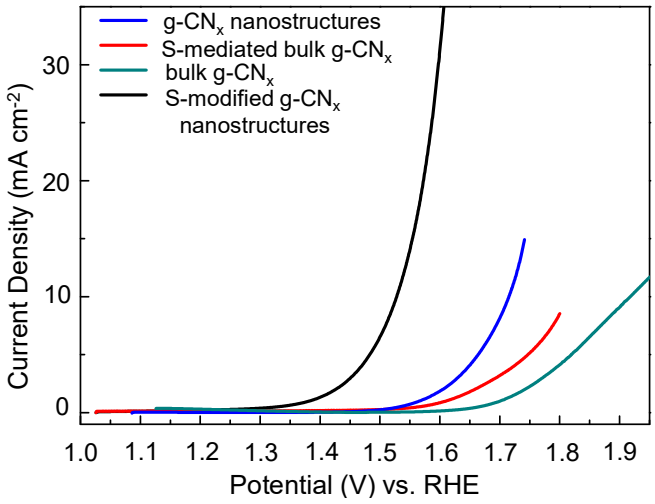


**Figure 2.9** Electrochemical response of various catalysts.

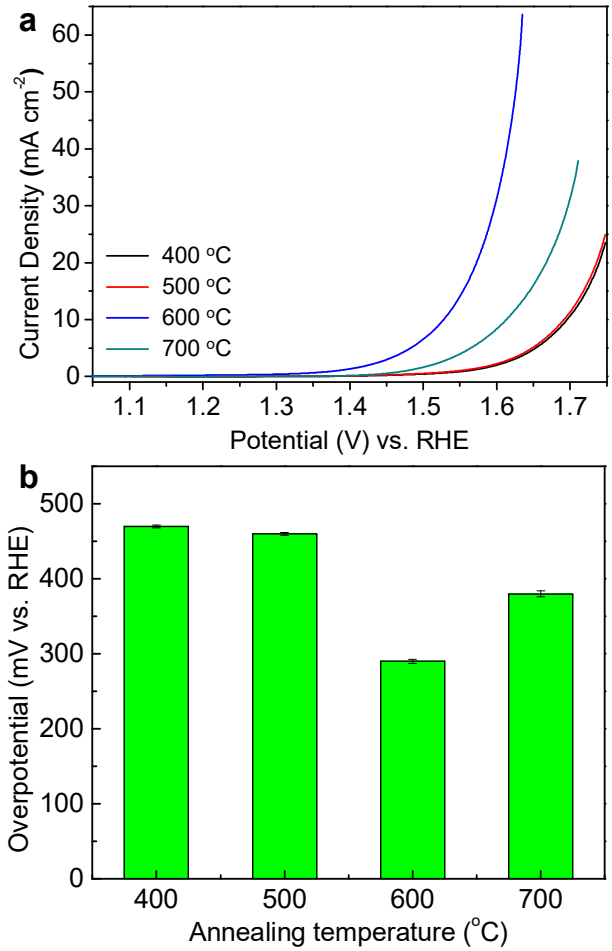


**Figure 2.10** Electrochemical responses of S-modified g-$CN_x$ nanostructures annealed at various temperatures.

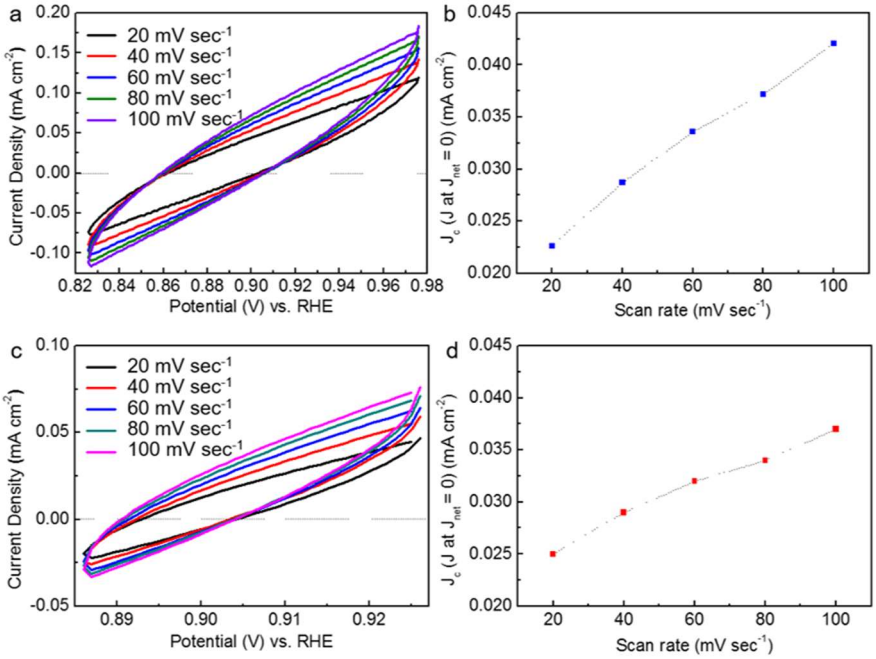


**Figure 2.11** The current to potential result of (a) S-modified g-$CN_x$ nanostructures and (c) g-$CN_x$ nanostructures at different scan rates. The capacitance current ($J_C$) of (b) S-modified g-$CN_x$ nanostructures and (d) g-$CN_x$ nanostructures at $J_{net}$= 0 mA $cm^{-2}$ depending on scan rates. The slope of the $J_C$ to scan rates plot is the capacitance of the double layer ($C_{dl}$), the value of which is 237.5 μF $cm^{-2}$ for S-modified g-$CN_x$ nanostructures and 145.0 μF $cm^{-2}$ for g-$CN_x$ nanostructures, respectively.

the Cdl divided by the capacitance of a smooth planar surface of the catalyst (Cs). Using the general Cs value of μF $cm^{-2}$ = 40 in 1 M KOH,[2] the ECSA of the S-modified g-$CN_x$ nanostructures and g-$CN_x$ nanostructures are 1.16 $cm^2$ and 0.71 $cm^2$, which corresponds to the roughness factor of 5.94 and 3.63, respectively. Therefore, the S-modified g-$CN_x$ nanostructures have high electrochemical catalytic surface area, due to the sulfur atoms adsorbed on the g-$CN_x$ surface, which may also provide the effective active sites for the OER. Furthermore, the rotating ring disk electrode measurement shows that the oxygen is directly generated from S-modified g-$CN_x$ nanostructures (Figure 2.12). The superior catalytic performance of S-modified g-$CN_x$ nanostructures isfurther demonstrated by their high stability. Chronoamperometry measurements were performed at 1.45 V vs. RHE in 1 M KOH solution (pH 14), and the obtained current densities normalized by their initial values are displayed as a function of time in Figure 2.7b. The S-modified g-$CN_x$ nanostructures maintain a current density of 2.3 mA $cm^{-2}$ and more than 91% of the normalized current, even after 18 h, which is comparable to other g-$CN_x$-based OER catalysts reported to date (Table 2.3). This result indicates that the S-modified g-$CN_x$ nanostructures exhibit good stability as well as efficient

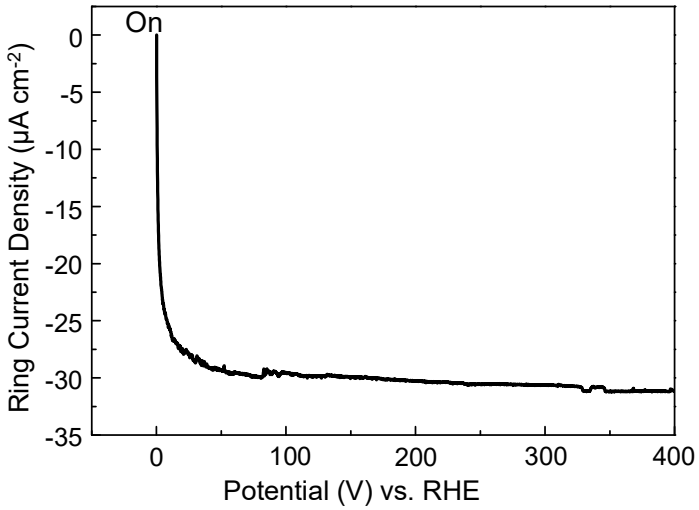


**Figure 2.12** Rotating ring disk electrode measurement proves that the $O_2$ is directly generated from S-modified g-$CN_x$ nanostructures. $I_{disk}$ is 0.2 mA at a disk potential of 0.4 V vs. RHE. The measurement was conducted referring to the following literature: *Science* **2011**, *334*, 1383

| Sr. No. | Sample | Remaining stability after chrono-amperometry operation (%) | Condition | References |
|---|---|---|---|---|
| 1 | S-modified g-$CN_x$ nanostructures (S: 0.5 g) | 91.2 | *18 h at 1.45 V vs. RHE* | *This study* |
| 2 | g-$C_3N_4$/CNT | 86.7 | *10 h at 1.54 V vs. RHE* | *Angew. Chem. Int. Ed.* **2014**, *53,* 7281 |
| 3 | P-doped g-$C_3N_4$/CFP | 93.4 | *30 h at 1.63 V vs. RHE* | *Angew. Chem. Int. Ed. 54,* **2015**, 4646 |
| 4 | Hybrid film of g-$C_3N_4$ and $Ti_3C_2$ | 95.5 | *10 h at 1.65 V vs. RHE* | *Angew. Chem. Int. Ed.* **2016**, *55,* 1138 |
| 5 | Ultrathin g-$C_3N_4$/graphene | 100 | *10 h at 1.0 V vs. Ag/AgCl (0.1 M KOH)* | *ChemSusChem.* **2014**, *7,* 2125 |

**Table 2.3** Comparison of remaining stabilities of g-$CN_x$ based OER catalysts after chronoamperometry operation

electrocatalytic activity towards the OER, demonstrating the significance of the sulfur modification in the g-$CN_x$ catalyst.

To gain more quantitative insight into the catalytic activity of the g-$CN_x$ catalysts, the *J-E* curves in Figure 2.7a are converted into Tafel plots, in which the potential is plotted as a function of the logarithm of *J*. Owing to solution resistance at the interface between the electrode and electrolyte, the measured potentials compensate for ohmic potential drop (iR) losses. The Tafel slope is defined as the potential required to increase the resulting current by one order of magnitude. A Tafel slope of 146 mV $dec^{-1}$ is obtained for the g-$CN_x$ nanostructures, whereas a Tafel slope of 120 mV $dec^{-1}$ is obtained for the S-modified g-$CN_x$ nanostructures (Figure 2.7a, inset). The Tafel slope is an inherent property of the catalyst that is determined by the rate-limiting step for the OER. Theoretically, Tafel slope value is closely related to the transfer coefficient value, α, that can provide mechanical insights for OER. Tafel slope of 60-80 mV $dec^{-1}$ is corresponding to 2.3 RT/F which means that reversible one-electron transfer reaction takes place before rate-determining step (RDS).Tafel slope of 110-130 mV $dec^{-1}$, 2.3×2RT/F suggests that a single-electron transfer step without pre-equilibrium step should exist in the following four electron-involved stepwise reaction paths:

$$H_2O(l) + * \rightarrow HO* + H^+ + e^- \quad (2.1)$$

$$HO* \leftrightarrow O* + H^+ + e^- \quad (2.2)$$

$$O* + H_2O(l) \leftrightarrow HOO* + H^+ + e^- \quad (2.3)$$

$$HOO* \leftrightarrow * + O_2(g) + H^+ + e^- \quad (2.4)$$

where * is an active site for OER catalysis. Therefore, observed Tafel slope of 120 mV $dec^{-1}$ in S-modified g-$CN_x$ nanostructures implies that the rate determining step is determined by a single-electron transfer step as shown in equation (2.1).

To evaluate the detailed water oxidation mechanism, proton reaction order was further investigated by a pH dependency test in the pH range between 6 and 14. The dependence of proton activity on current density is derived as

$$\left(\frac{\partial E}{\partial pH}\right)_j = -\left(\frac{\partial log j}{\partial pH}\right)_E \left(\frac{\partial E}{\partial log j}\right)_{pH} \quad (2.5)$$

From the pH dependency test, $\left(\frac{\partial E}{\partial pH}\right)_j$ is calculated as -127.5 mV $pH^{-1}$ (Figure 2.13a and b). Substituting the value of $\left(\frac{\partial E}{\partial pH}\right)_j$ and the Tafel slope $\left(\frac{\partial E}{\partial log j}\right)_{pH}$ (Figure 2.13c) into equation (2.5) gave a

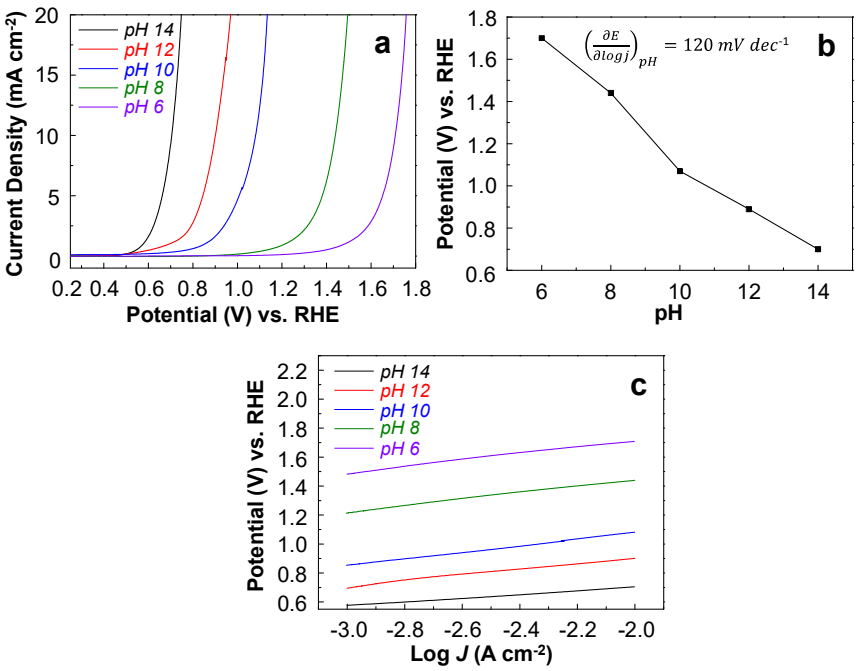


**Figure 2.13** pH dependence of S-modified g-$CN_x$ nanostructures. (a) *J-E* curves of S-modified g-$CN_x$ nanostructures in a pH range from 6 to 14. (b) Potential of the catalyst at 10 mA $cm^{-2}$ with in creasing pH. (c) Tafel plots derived from the *J-E* data in (a).

$\left(\frac{\partial log j}{\partial pH}\right)_E$ value of 1.06. It indicates that the water oxidizing reaction rate is affected by the proton activity with inverse first-order dependence. Taken together, the electrochemical law for S-modified g-$CN_x$ nanostructures is derived, as follows:

$$i = k_0(a_{H^+})^{-1.06} e^{\frac{0.5EF}{RT}} \quad (2.6)$$

where, $k_0$, $a_{H+}$, and $F$ are a potential-independent constant, the proton activity, and the Faraday constant, respectively. From the established equation 2.6, it can be assumed that a single electron is involved at the rate-determining step, as obtained from the above described experimental results. From the literature, the OER mechanism of g-$CN_x$ has been also calculated, and the rate determining step is shown to be the first step. Modification with sulfur does not change the OER mechanism, but lowers the overpotential for the OER, which is consistent with the experimental results. DFT calculation from the literature also can provide helpful insights for possible intrinsic mechanism for the enhanced OER property of the S-modified g-$CN_x$ nanostructures.[64] The S-doping or S-adsorption of g-$CN_x$ forms the material a conductor by reasonably narrowing of the band gap and also by the Fermi level shifting to the conduction band. The electronic structure of g-$CN_x$ catalyst in our

system might be also affected by S-modification favourable to enhanced conductivity as well as higher catalytic property. The impedance spectroscopy was also analysed to measure a resistance of catalysts in an electrolyte solution. The resistances of the bare glassy carbon electrode, bulk g-$CN_x$, g-$CN_x$ nanostructures, and S-modified g-$CN_x$ nanostructures are 7.0 Ω, 10.0 Ω, 7.3 Ω, and 7.1 Ω, respectively. The resulting lower resistance also proves that the S-modified g-$CN_x$ nanostructures have higher conductivity compared to the bare g-$CN_x$ nanostructures. To investigate more about the origin of the enhanced catalytic activity, electrochemical impedance measurements were performed. A Nyquist plot of a typical impedance result with only one semicircle is shown in Figure 2.14. The single semicircle indicates that the equivalent circuit for the electrocatalysis is characterized by one time constant. Compared with the bare g-$CN_x$ nanostructures (135 Ω $cm^2$), the semicircle observed for the S-modified g-$CN_x$ nanostructures is much smaller, corresponding to a lower charge-transfer resistance (38 Ω $cm^2$). The charge-transfer resistance is related to the kinetic barrier energy for Faradaic reactions (OER) across the interface between the catalyst and electrolyte.[73] The charge-transfer resistance is also inversely proportional to the exchange current for the Faradaic reaction, as

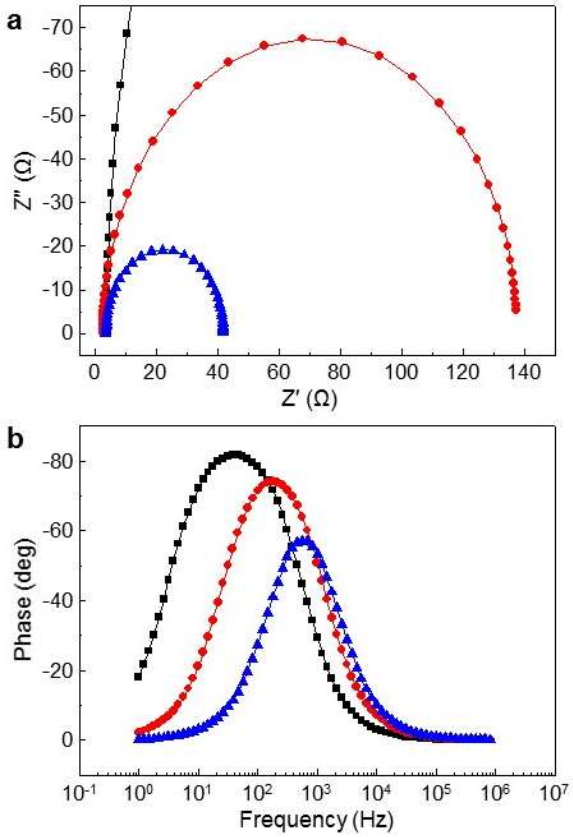


**Figure 2.14** Impedance results for g-$CN_x$ electrocatalysts. (a) Nyquist plots for bulk g-$CN_x$ (black), g-$CN_x$ nanostructures (red), and S-modified g-$CN_x$ nanostructures (blue) at a constant potential of 1.4 V vs. RHE. (b) Bode phase plots for bulk g-$CN_x$ (black), g-$CN_x$ nanostructures (red), and S-modified g-$CN_x$ nanostructures (blue).

described by the Butler-Volmer equation.[74] Consequently, the lower charge-transfer resistance of the S-modified g-$CN_x$ nanostructures promotes the OER, thus lowering the overpotential. Moreover, the dependence of the phase angle on the frequency (Bode phase plot), as shown in Figure 2.14b, shows the same frequency time constant trend. Thus, the impedance analysis verifies the enhanced catalytic properties of the S-modified g-$CN_x$ nanostructures and the above-mentioned mechanism.

## 2.4 Conclusion

In conclusion, we successfully synthesized S-modified g-$CN_x$ nanostructures by *in situ* modification of our novel melamine nanogeodes with sulfur and they showed excellent catalytic properties due to minimization of the activation energy for the OER. The low overpotential ($\eta$ = 290 mV) achieved with the S-modified g-$CN_x$ nanostructures is indeed an urgent requirement for OER catalysts to minimize energy loss during the process. To date, this value is the best among non-metal, metal/metal oxide, and well-established catalysts. The long-term performance of 18 h with more than 91% retention of activity for S-modified g-$CN_x$ nanostructures will allow realization of practical applications. New catalysts are needed for the OER, and the unique morphology MNGs to achieve g-$CN_x$ nanostructures and improved activity through sulfur modification will attract much attention in this field. The developed synthetic strategy and our understanding can be directly applied to various other electrocatalysts, emphasizing the importance of nanostructure and sulfur modification for better activity and stability.

**Most of the contents of this chapter were published in the article, "Sulfur-Modified Graphitic Carbon Nitride Nanostructures as an Efficient Electrocatalyst for Water Oxidation"

*Small*, **2017**, *13(17)*, 1603893

## 2.5 References


[1] L. Trotochaud, S. W. Boettcher, *Scr. Mater.* **2014***, 74,* 25.

[2] C. C. L. McCrory, S. Jung, J. C. Peters, T. F. Jaramillo, *J. Am. Chem. Soc.*, **2013**, *135*, 16977.

[3] C. C. L. McCrory, S. Jung, I. M. Ferrer, S. M. Chatman, J. C. Peters, T. F. Jaramillo, *J. Am. Chem. Soc.* **2015,** *137*, 4347.

[4] H. Kim, J. Park, I. Park, K. Jin, S. E. Jerng, S. H. Kim, K. T. Nam, K. Kang, *Nat. Commun.* **2015,** *6 ,*8253.

[5] K. Jin, A. Chu, J. Park, D. Jeong, S. E. Jerng, U. Sim, H. Y. Jeong, C. W. Lee, Y. S. Park, K. D. Yang, G. K. Pradhan, D. Kim, N. E. Sung, S. H. Kim, K. T. Nam, *Sci. Rep.* **2015,** *5*, 10279.

[6] K. Jin, J. Park, J. Lee, K. D. Yang, G. K. Pradhan, U. Sim, D. Jeong, H. L. Jang, S. Park, D. Kim, N. E. Sung, S. H. Kim, S. Han, K. T. Nam, *J. Am. Chem. Soc.* **2014,** *136*, 7435.

[7] T. Takashima, K. Hashimoto, R. Nakamura, *J. Am. Chem. Soc.* **2012,** *134*, 18153.

[8] T. Takashima, K. Hashimoto, R. Nakamura, *J. Am. Chem. Soc.* **2012,** *134*, 1519.

[9] A. Yamaguchi, R. Inuzuka, T. Takashima, T. Hayashi, K. Hashimoto, R. Nakamura, *Nat. Commun.* **2014,** *5,* 4256.

[10] B. J. Trześniewski, O. Diaz-Morales, D. A. Vermaas, A. Longo, W. Bras, M. T. M. Koper, W. A. Smith, *J. Am. Chem. Soc.* **2015,** *137*, 15112.

[11] N. Han, F. Zhao, Y. Li, *J. Mater. Chem. A* **2015,** *3*, 16348.

[12] Y. Zhao, R. Nakamura, K. Kamiya, S. Nakanishi, K. Hashimoto, *Nat. Commun.* **2013,** *4,* 2390.

[13] Y. Jia, L. Zhang, A. Du, G. Gao, J. Chen, X. Yan, C. L. Brown, X. Yao, *Adv. Mater.* **2016,** *28*, 9532.

[14] J. Li, Y. Wang, T. Zhou, H. Zhang, X. Sun, J. Tang, L. Zhang, A.

M. Al-Enizi, Z. Yang, G. Zheng, *J. Am. Chem. Soc.* **2015,** *137*, 14305.

[15] H. Wu, J. Geng, H. Ge, Z. Guo, Y. Wang, G. Zheng, *Adv. Energy Mater.* **2016,** *6*, 1600794.

[16] X. Wang, K. Maeda, A. Thomas, K. Takanabe, G. Xin, J. M. Carlsson, K. Domen, M. Antonietti, *Nat. Mater.* **2009,** *8*, 76.

[17] X. Chen, J. Zhang, X. Fu, M. Antonietti, X. Wang, *J. Am. Chem. Soc.* **2009,** *131*, 11658.

[18] Y. Wang, J. Yao, H. Li, D. Su, M. Antonietti, *J. Am. Chem. Soc.* **2011,** *133*, 2362.

[19] J. Liu, H. Wang, M. Antonietti, *Chem. Soc. Rev.* **2016,** *45*, 2308.

[20] Y. Zheng, J. Liu, J. Liang, M. Jaroniec, S. Z. Qiao, *Energy Environ. Sci.* **2012,** *5*, 6717.

[21] Y. Zheng, Y. Jiao, M. Jaroniec, Y. Jin, S. Z. Qiao, *Small* **2012,** *8*, 3550.

[22] Y. Zhang, T. Mori, J. Ye, M. Antonietti, *J. Am. Chem. Soc.* **2010,** *132*, 6294.

[23] Y. Wang, H. Li, J. Yao, X. Wang, M. Antonietti, *Chem. Sci.* **2011,** *2*, 446.

[24] J. Shui, M. Wang, F. Du, L. Dai, *Sci. Adv.* **2015,** *1,* e1500564.

[25] G. Wu, Y. Hu, Y. Liu, J. Zhao, X. Chen, V. Whoehling, C. Plesse, G. T. M. Nguyen, F. Vidal, W. Chen, *Nat. Commun.* **2015,** *6,* 7258.

[26] K. Sakaushi, M. Antonietti, *Acc. Chem. Res.* **2015,** *48*, 1591.

[27] S. J. A. Moniz, S. A. Shevlin, D. J. Martin, Z. X. Guo, J. Tang, *Energy Environ. Sci.* **2015,** *8*, 731.

[28] J. Zhang, J. Sun, K. Maeda, K. Domen, P. Liu, M. Antonietti, X. Fu, X. Wang, *Energy Environ. Sci.* **2011,** *4*, 675.

[29] J. Xu, S. Cao, T. Brenner, X. Yang, J. Yu, M. Antonietti, M. Shalom, *Adv. Funct. Mater.* **2015,** *25*, 6265.

[30] Y. Zheng, Y. Jiao, J. Chen, J. Liu, J. Liang, A. Du, W. Zhang, Z. Zhu, S. C. Smith, M. Jaroniec, G. Q. Lu, S. Z. Qiao, *J. Am. Chem. Soc.* **2011,** *133*, 20116.

[31] J. Liang, Y. Zheng, J. Chen, J. Liu, D. H. Jurcakova, M. Jaroniec, S. Z. Qiao, *Angew. Chem. Int. Ed.* **2012,** *51*, 3892.

[32] Y. Zheng, Y. Jiao, Y. Zhu, L. H. Li, Y. Han, Y. Chen, A. Du, M. Jaroniec, S. Z. Qiao, *Nat. Commun.* **2014,** *5,* 3783.

[33] T. Y. Ma, S. Dai, M. Jaroniec, S. Z. Qiao, *Angew. Chem. Int. Ed.* **2014,** *53*, 7281.

[34] Y. Jiao, Y. Zheng, M. Jaroniec, S. Z. Qiao, *Chem. Soc. Rev.* **2015,** *44*, 2060.

[35] T. Y. Ma, J. Ran, S. Dai, M. Jaroniec, S. Z. Qiao, *Angew. Chem. Int. Ed.* **2015,** *54*, 4646.

[36] S. Cao, J. Low, J. Yu, M. Jaroniec, *Adv. Mater.* **2015,** *27*, 2150.

[37] L. B. Sun, X. Q. Liu, H. C. Zhou, *Chem. Soc. Rev.* **2015,** *44*, 5092.

[38] Y. Gong, M. Li, Y. Wang, *ChemSusChem* **2015,** *8*, 931.

[39] Z. Zhao, Y. Sun, F. Dong, *Nanoscale* **2015,** *7*, 15.

[40] Y. Zheng, L. Lin, B. Wang, X. Wang, *Angew. Chem. Int. Ed.* **2015,** *54*, 12868.

[41] J. Zhang, Y. Chen, X. Wang, *Energy Environ. Sci.* **2015,** *8*, 3092.

[42] X. Dong, F. Cheng, *J. Mater. Chem. A* **2015,** *3*, 23642.

[43] Y. Zhao, J. Zhang, L. Qu, *ChemNanoMat* **2015,** *1*, 298.

[44] Z. Lin, X. Wang, *Angew. Chem. Int. Ed.* **2013,** *52*, 1735.

[45] J. S. Lee, G. S. Park, S. T. Kim, M. Liu, J. Cho, *Angew. Chem. Int. Ed.* **2013,** *52*, 1026.

[46] H. Huang, S. Yang, R. Vajtai, X. Wang, P. M. Ajayan, *Adv. Mater.* **2014,** *26*, 5160.

[47] J. Sun, J. Zhang, M. Zhang, M. Antonietti, X. Fu, X. Wang, *Nat. Commun.* **2012**, *3*, 1139.

[48] Z. Zhou, J. Wang, J. Yu, Y. Shen, Y. Li, A. Liu, S. Liu, Y. Zhang, *J. Am. Chem. Soc.* **2015,** *137*, 2179.

[49] T. Y. Ma, Y. Tang, S. Dai, S. Z. Qiao, *Small* **2014,** *10*, 2382.

[50] S. Yang, Y. Gong, J. Zhang, L. Zhan, L. Ma, Z. Fang, R. Vajtai, X. Wang, P. M. Ajayan, *Adv. Mater.* **2013,** *25*, 2452.

[51] G. Vilé, D. Albani, M. Nachtegaal, Z. Chen, D. Dontsova, M. Antonietti, N. López, J. Pérez-Ramírez, *Angew. Chem. Int. Ed.* **2015,** *54*, 11265.

[52] J. Liu, W. Li, L. Duan, X. Li, L. Ji, Z. Geng, K. Huang, L. Lu, L. Zhou, Z. Liu, W. Chen, L. Liu, S. Feng, Y. Zhang, *Nano Lett.* **2015,** *15*, 5137.

[53] Y. Hou, Z. Wen, S. Cui, X. Feng, J. Chen, *Nano Lett.* **2016,** *16*, 268.

[54] Q. Pang, L. F. Nazar, *ACS Nano* **2016,** *10*, 4111.

[55] L. Hao, J. Ning, B. Luo, B. Wang, Y. Zhang, Z. Tang, J. Yang, A. Thomas, L. Zhi, *J. Am. Chem. Soc.* **2015,** *137*, 219.

[56] J. Zhu, K. Sakaushi, G. Clavel, M. Shalom, M. Antonietti, T. P. Fellinger, *J. Am. Chem. Soc.* **2015,** *137*, 5480.

[57] Y. Hou, F. Zuo, A. P. Dagg, J. Liu, P. Feng, *Adv. Mater.* **2014,** *26*, 5043.

[58] J. Liu, Y. Liu, N. Liu, Y. Han, X. Zhang, H. Huang, Y. Lifshitz, S. T. Lee, J. Zhong, Z. Kang, *Science* **2015,** *347*, 970.

[59] G. Zhang, M. Zhang, X. Ye, X. Qiu, S. Lin, X. Wang, *Adv. Mater.* **2014,** *26*, 805.

[60] Q. Han, C. Hu, F. Zhao, Z. Zhang, N. Chen, L. Qu, *J. Mater. Chem. A* **2015,** *3*, 4612.

[61] Y. Wang, Y. Di, M. Antonietti, H. Li, X. Chen, X. Wang, *Chem. Mater.* **2010,** *22*, 5119.

[62] G. Liu, P. Niu, C. Sun, S. C. Smith, Z. Chen, G. Q. Lu, H. M. Cheng, *J. Am. Chem. Soc.* **2010,** *132*, 11642.

[63] S. Lin, X. Ye, X. Gao, J. Huang, *J. Mol. Catal. A: Chem.* **2015,** *406*, 137.

[64] S. Sergey, Z. Sebastian, *J. Phys. Condens. Matter* **2013,** *25*, 085507.

[65] C. Xu, Q. Han, Y. Zhao, L. Wang, Y. Li, L. Qu, *J. Mater. Chem. A* **2015,** *3*, 1841.

[66] J. Hong, X. Xia, Y. Wang, R. Xu, *J. Mater. Chem.* **2012,** *22*, 15006.

[67] Y. Wang, J. Zhang, X. Wang, M. Antonietti, H. Li, *Angew. Chem. Int. Ed.* **2010,** *49*, 3356.

[68] J. Tian, Q. Liu, A. M. Asiri, K. A. Alamry, X. Sun, *ChemSusChem* **2014,** *7*, 2125.

[69] T. Y. Ma, J. L. Cao, M. Jaroniec, S. Z. Qiao, *Angew. Chem. Int. Ed.* **2016,** *55*, 1138.

[70] J. P. Randin, E. Yeager, *J. Electrochem. Soc.* **1971***, 136*, 711.

[71] D. Kong, H. Wang, Z. Lu, Y. Cui, *J. Am. Chem. Soc.* **2014,** *136,* 4897.

[72] S. Trasatti, O. A. Petrii, *J. Electroanal. Chem.* **1992,** *327*, 353.

[73] D. Merki, H. Vrubel, L. Rovelli, S. Fierro, X. Hu, *Chem. Sci.* **2012,** *3*, 2515.

[74] A. J. Bard, L. R. Faulkner, Electrochemical Methods: Fundamentals and Applications, *Wiley New York* **1980**.

# Chapter 3. Gram-Scale Synthesis of Porous and Heteroatom Co-doped Hollow Carbon Nanostructures Derived from MOF-Oligomer Nanoparticles for Flexible All-Solid-State-Supercapacitors

## 3.1 Introduction

There is an immense rise in the energy demand of the globe due to the increased population and rise in usage of the portable electronics in the day to day life. In order to fulfill such a vast energy hunger, attention is need to be focused on the exploration of alternative energy conversion and storage devices having high efficiency, low cost and environmental compatibility. Hence, it's the need of the hour to synthesize novel electrode materials or catalysts which can produce zero production waste and achieve the best performance in the energy conversion and storage regime. There are a plenty of materials explored for the enhanced energy conversion and storage such as nanostructured

metal oxides, conjugated polymers, metal sulfides, transition metal dichalcogenides (TMDs) and heteroatom-doped/co-doped carbons etc. Heteroatom co-doped carbon materials are showing greater promise as an option for electrode materials replacing traditional carbon materials such as carbon fibers, carbon nanotubes and carbon blacks.[1-4] It should be noted that doping of carbon nanomaterials with heteroatoms like N, S, B and P could be responsible for electron modulation to tune their chemical activities. Amongst the heteroatoms, nitrogen plays a more critical role in modifying the carbon frameworks as nitrogen (65 pm) and carbon (70 pm) atoms have nearly similar atomic size and five valence electrons, so it can form strong covalent bonds with the carbons. The good electronic conductivity of nitrogen-doped carbon materials have shown best electrochemical performance compared to their un-doped counterparts. Along with N, other heteroatom co-doping with P also important due to the synergistic effects in carbon nanomaterials.[1] Recently, hexachlorocyclotriphosphazene (HCTP) have attracted a lot attention due to equal number of N and P atoms in six membered cyclic backbone.[2-4] HCTP can be easily condensed or complexed with other functional groups such as -$NH_2$, -OH, etc to form a class of macromolecules known as “phosphazene”. Hexahydroxytriphenylene

(HHTP) has six free –OH group and has been used to make metal-organic frameworks.[5-6] Combination of HCTP and HHTP to make cross-linked oligomers are not successfully synthesized yet.

Metal-organic framework (MOF) have a systematic arrangements of metal ions and organic ligands. Due to the rich source of N-doped carbon and the availability to choose metals to be incorporated, MOF derived carbon is being used in many applications.[7-8] Also MOFs, particularly, zinc containing MOF (i.e. ZIF-8) is used as a sacrificial template due to the sublimation tendency of zinc at high temperatures. But still there is a lack of systematic study on the use of ZIF-8 as a core and phosphazenes as a shell to synthesize heteroatom-doped/co-doped carbon nanomaterials which can have control over microporosity.

Present chapter deals with the wrap-bake-sublime approach to scalable synthesis of N, P co-doped hollow carbon nanostructures (NPHCs) by the carbonization of core ZIF-8 nanoparticles wrapped with a cross-linked OCHT oligomer shell which was formed by a condensation reaction between HCTP and HHTP. The carbonization at high temperature leads to sublimation of zinc creating pores in the final product. The OCHT shell is then converted to N, P co-doped hollow

carbon nanostructures resultant due to hollow cavities from the sacrificial ZIF-8 template. The control over the microporosity and N, P co-doping is achieved through the variation in the thickness of OCHT shell during the formation of core-shell ZIF-8@OCHT nanoparticles and due to successive carbonization at high temperature. Moreover, our approach is easily scalable to achieve gram-level synthesis. The microporosity and amount of co-doping dependency is found to determine the electrochemical performance of supercapacitors using NPHC electrodes. Finally, a symmetric and flexible all-solid-state-supercapacitor was assembled and demonstrated notable specific capacitance, energy density, power density and long-term cycling durability.

## 3.2. Experimental Section

### 3.2.1 Synthesis of MOF (ZIF-8)

Zinc nitrate (1.66 g, 5.6 mM) in 20 mL of methanol is mixed quickly with 2-methyl imidazole (MIZ) (4 g, 48.7 mM) in 60 mL of methanol stirred for 1 h. The solution was aged for 24 h at room temperature. The aliquot was washed with methanol many times by centrifugation at 10,000 r.p.m. for 15 minutes each. ZIF-8 nanoparticles were recovered in powder form and vacuum dried overnight at 80 °C. For further use ZIF-8 powder were re-dispersed in 40 mL methanol and D. I. water. Various core-shell nanoparticles (ZIF-8@OCHT-0.5, ZIF-8@OCHT, ZIF-8@OCHT-2 and ZIF-8@OCHT-3) were synthesized by using above ZIF-8 nanoparticles.

### 3.2.2 Synthesis of Core-shell ZIF-8@OCHT Nanoparticles

The 20 mL methanol solution was prepared by dissolving hexachlorocyclotriphosphazene (HCTP) (100 mg, 0.29 mM) and hexahydroxytriphenylene (HHTP) (94 mg, 0.29 mM); then added to the 40 mL methanol solution dissolved with the given amounts of ZIF-8. After stirring for 5 min, 1 mL of triethylamine (TEA) was quickly added, and overnight stirred. Methanol and D. I. water was used several times to wash the aliquot several by centrifugation, and vacuum dried

overnight at 80 °C. ZIF-8@OCHT nanoparticles in powder form is recovered. Without using ZIF-8 as core, in the same way only OCHT oligomer was synthesized.

The same method was used to prepare core-shell nanoparticles with increasing amounts of oligomers (ZIF-8@OCHT-0.5, ZIF-8@OCHT-2, and ZIF-8@OCHT-3) only the equimolar amounts of HCTP and HHTP used were varied. Typically, 50 mg (0.145 mM) of HCTP and 47 mg (0.145 mM) of HHTP with 0.5 mL TEA were used for ZIF-8@OCHT-0.5; 200 mg (0.58 mM) of HCTP and 188 mg (0.58 mM) of HHTP with 2 mL TEA for ZIF-8@OCHT-2; and 302 mg (0.87 mM) of HCTP and 282 mg (0.87 mM) of HHTP with 3 mL TEA for ZIF-8@OCHT-3 were used.

### 3.2.3 Synthesis of NPHC

A tubular quartz furnace was used for thermal annealing. An alumina crucible was used for the core-shell ZIF-8@OCHT nanoparticles. Argon gas (99.995 %) was used at the flow rate of 100 sccm. The temperature of 915 °C for 4 h was used for annealing, starting from room temperature at the ramping rate of 2 °C per minute. After the high temperature annealing, the carbonized sample of NPHC was collected and a coarse powder was achieved by using mortar and pestle. The acid treatment was

carried out by using 3 N HCl to dissolve powder and stirred overnight at 80 °C. D.I. water was used to thoroughly wash the acid solution by vacuum filtration and the washing procedure was repeated several times. The same procedure was repeated for NPHC-0.5, NPHC-2, and NPHC-3, by using ZIF-8@OCHT-0.5, ZIF-8@OCHT-2, ZIF-8@OCHT-3 nanoparticles as a starting materials, respectively. Also NPC and NC were synthesized from OCHT and ZIF-8 nanoparticles, respectively. 800 and 1000 °C temperature is used to get NPHC-800 and NPHC-1000 by using the same core-shell ZIF-8@OCHT nanoparticles. All the samples were acid washed in the same manner as NPHC.

*Synthesis of NPHC-GS*: The gram-level synthesis was achieved by increasing each reagent by a factor of 12.5 from typical small scale synthesis of NPHC.

### 3.2.4 Physicochemical Characterization

The TEM, high-resolution TEM, and HAADF-STEM images with EDS elemental mapping were obtained with a JEOL 2100F electron microscope operated at 200 kV. The FESEM images were obtained with ZEISS MERLIN Compact instrument. The XRD measurements were done using a D/Max-3C diffractometer (Cu Kα radiation source, λ = 0.15418 nm) equipped with a rotating anode. XPS data were collected

using an AXIS-Ultra DLD system (Kratos Inc.), and all spectra were corrected using C 1s at 284.5 eV. $N_2$ sorption measurements were performed on a high-end volumetric gas adsorption instrument (BELSORP-Max, MicrotracBEL Corp.) using high purity (99.999 %) $N_2$ at 77 K. Prior to the sorption measurements, the samples were pretreated at pressure below 0.001 torr and temperature of 200 °C for 14 h. The surface areas and pore size distributions were calculated using Brunauer-Emmett-Teller (BET) method and the non-localized density functional theory (NLDFT) method, respectively. A TENSOR27 spectrometer from Bruker, Germany was used for FT-IR spectra. 4 mm CPMAS probes and a 500 MHz Bruker ADVANCE III HD NMR spectrometer was used for solid state $^{31}P$ MAS NMR and $^{13}C$ CPTOSS spectra in NCIRF (National Center for Inter-University Research Facilities, Seoul National University, Republic of Korea). $^{31}P$ MAS spectra were obtained by using the spinning speed of 8 kHz and pulse repetition delays of 1s. Chemical shifts for the $^{31}P$ spectra are referenced in parts per million relative to 99 % phosphoric acid. $^{13}C$ CPTOSS spectra are collected using the contact times of 2 ms and spinning speed of 5 kHz. MALDI-TOF MS analysis was performed on a Voyager-DETM STR Biospectrometry Workstation (Applied Biosystems Inc.) located at the NCIRF (Seoul National

University, Republic of Korea). The Raman spectra were obtained using a T64000 system (HORIBA Jobin Yvon, France) equipped with an Ar-ion laser ($\lambda$ = 514 nm).

### 3.2.5 Electrochemical Characterization

A ZIVE SP1 electrochemical workstation (ZIVE Lab, Korea) was used for the electrochemical characterizations with a standard three-electrode system. A homogeneous slurry was made by mixing active material (40 mg), polyvinylidene difluoride (PVDF; 5 mg), and carbon black (5 mg) with 0.5 mL N-methyl 2-pyrrolidine (NMP) to prepare the working electrode. A Ti foil substrate was used to coat the slurry and dried at 60 °C overnight in a vacuum oven. A geometric surface area of 1.0 $cm^2$ with approximately 2 mg of total mass contain on each electrode. The electrochemical measurements were performed with a Pt foil as a counter electrode and a saturated Ag/AgCl electrode as a reference electrode was used in 1 M $H_2SO_4$ at room temperature. Cyclic voltammograms (CVs) were obtained with a potential range from 0.0 V to 1.0 V at various scan rates. The same potential range at different current densities was used for galvanostatic charge/discharge (GCD) measurements.

For the full-cell electrochemical test, the PVA-$H_2SO_4$ gel electrolyte were sandwiched together into two identical electrodes. The

homogeneous PVA-$H_2SO_4$ solution was prepared by dissolving 10 g of polyvinyl alcohol (PVA) in 10 mL of 1 M $H_2SO_4$ solution, and the mixture was stirred at 80 °C. CV and GCD were measured with similar manner of three electrode measurements. The AC amplitude of 5 mV at open circuit voltage (OCV) over the frequency range of 0.1 Hz-1 MHz was used for EIS measurements. The specific capacitance was calculated from GCD curves using the following equation:

$$Cs = \frac{I \times \Delta t}{\Delta V \times m} \tag{3.1}$$

where I (A) is the discharging current, Δt (t) is discharging time, ΔV (V) is voltage range during discharging and m (g) is active mass of the samples.

Energy density (*E*, in Wh $kg^{-1}$) and power density (*P*, in W $kg^{-1}$) were calculated from Equation (3.2) and (3.3), respectively:

$$E = \frac{0.5C(\Delta V)^2}{3.6} \tag{3.2}$$

$$P = \frac{E3600}{\Delta t} \tag{3.3}$$

## 3.3. Results and Discussion

### 3.3.1 Synthesis of NPHCs by Wrap-Bake-Sublime Approach and Morphological Characterization

The synthesis of NPHC by wrap-bake-sublime approach is shown in the schematic illustration in Figure 3.1a. The ZIF-8 nanoparticles were used as a core and wrapped in an OCHT shell in the step i. The as-synthesized core-shell ZIF-8@OCHT nanoparticles, were baked (the step ii), at slightly higher temperature (915 °C) than the zinc sublimation temperature (907 °C), in an argon atmosphere. During this annealing process, Zn ions in the core of the ZIF-8 nanoparticles are reduced to metallic zinc and then sublime to the outside *via* the OCHT shell, introducing porosity in the OCHT shell. After annealing (step iii), the OCHT shell is converted into N, P co-doped hollow carbon nanostructures (NPHC). The OCHT oligomer was obtained by the condensation reaction of equimolar mixture of HCTP and HHTP in methanol with triethylamine (TEA) (Figure 3.1b). Fourier transform infrared (FT-IR) spectra in Figure 3.1c (Finger print region in Figure 3.2a) show that HCTP have characteristic peaks at 1182 $cm^{-1}$ for P=N and 874 $cm^{-1}$ for P-N, which are retained and red shifted in OCHT. A new peak of OCHT at 923 $cm^{-1}$ is evidence of the successful formation of P-O-Ar

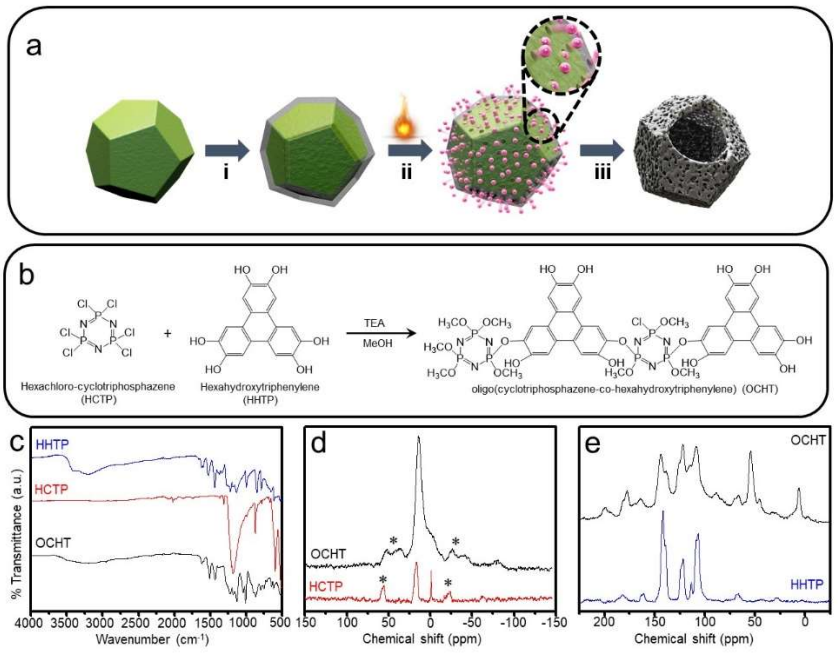


**Figure 3.1** (a) Schematic illustration for the synthesis of N, P co-doped carbon nanocage (NPHC). Preparation of OCHT oligomer is shown in scheme (b). (c) FT-IR analysis of HHTP, HCTP, and OCHT. (d) $^{31}$P MAS NMR spectra of HCTP and OCHT (8 kHz spinning, *spinning sideband). (e) $^{13}$C CPTOSS NMR spectra of HHTP and OCHT.

bonds. The distinct peak for P-Cl at 595 $cm^{-1}$ in HCTP is attenuated in OCHT. Solid-state $^{31}P$ nuclear magnetic resonance (NMR) of OCHT oligomer (Figure 3.1d) shows a broad peak at 14.2 ppm for N=P(-O-Ar) and N=P(-$OCH_3$) and a shoulder at -3.4 ppm for N=P(-Cl), while the HCTP monomer shows peaks at 16.4 ppm for N=P(-$Cl_2$) and -0.9 ppm for the partially polymerized cyclic molecules from the reagent itself.[2-4] The solid-state $^{13}C$ NMR of HHTP monomer in Figure 3.1e shows three sets of peaks at 141.9, 121.9, and 106.8 ppm for the three kinds of carbon environment, which after the oligomerization in OCHT are shifted to 144.4, 122.3, and 108.7 ppm, respectively.[5-6] Further, solid-state $^{13}C$ NMR data of OCHT in Figure 3.1e show an additional peak at 54.7 ppm for N=P(-$OCH_3$) coming from methanol, and two peaks at 45.6 and 6.4 ppm for triethylamine hydrochloride. This spectroscopy analysis of FT-IR, $^{31}P$ and $^{13}C$ solid-state NMR ascertains oligomerization of OCHT. The most plausible structure of OCHT, shown in Figure 3.1b, is supported by matrix-assisted laser desorption/ionization time-of-flight (MALDI-TOF) mass spectra (Figure 3.2b). Field-emission scanning electron microscopy (FESEM) (Figure 3.3a-b) and transmission electron microscopy (TEM) images (Figure 3.3c-d) show that approximately spherical nanoparticles of OCHT are formed with varying sizes. The

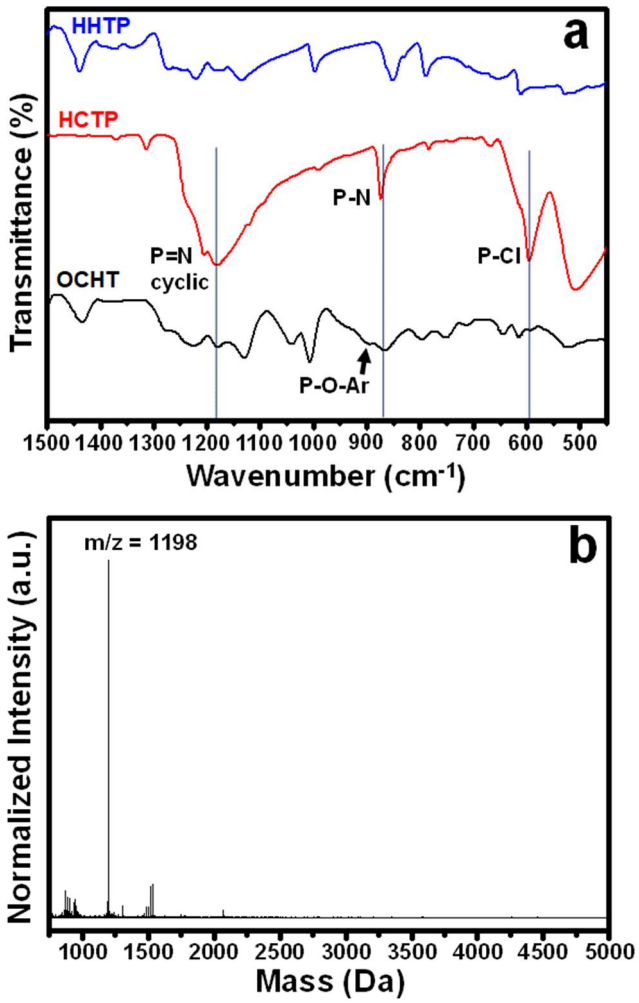


**Figure 3.2** (a) Finger print region FT-IR analysis of HHTP, HCTP, and OCHT. (b) MALDI-TOF mass spectra of OCHT. The plausible structure of OCHT presented in Figure 3.1e is assigned to the peak of m/z = 1198 Da.

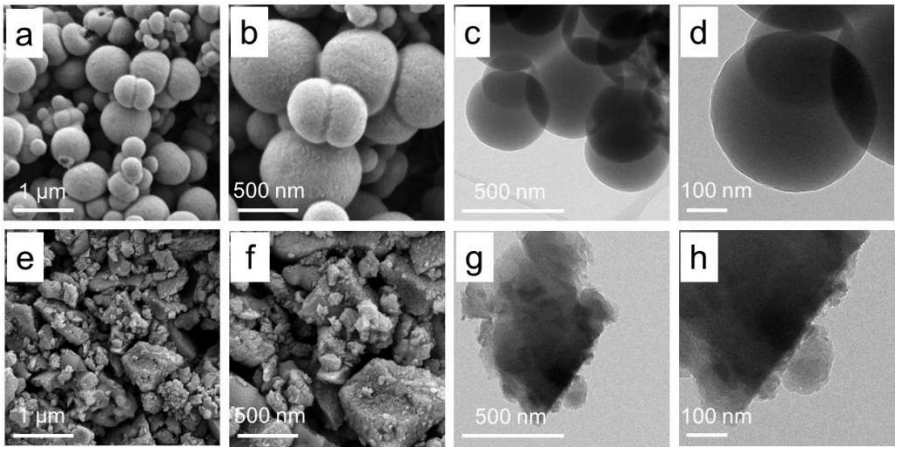


**Figure 3.3** FESEM (a, b) and TEM (c, d) images of OCHT nanoparticles. FESEM (e, f) and TEM (g, h) images of NPC (OCHT carbonized) nanoparticles.

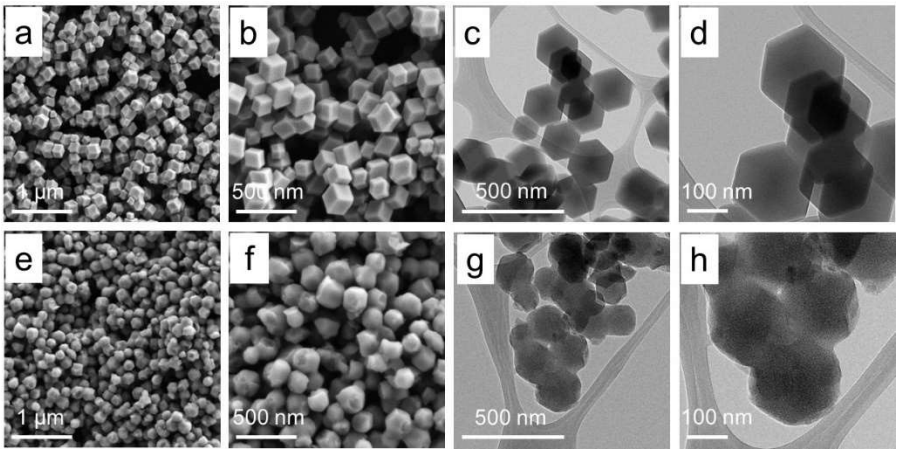


**Figure 3.4** FESEM (a, b) and TEM (c, d) images of core ZIF-8. FESEM (e, f) and TEM (g, h) images of NC (ZIF-8 carbonized) nanoparticles.

ZIF-8 nanoparticles were prepared at room temperature in a simple reaction from a methanol solution of zinc nitrate and 2-methyl imidazole (MIZ). The FESEM and TEM images in Figure 3.4a-b and c-d show that ZIF-8 nanoparticles are successfully formed to have solid polygonal structures with size ranging from 200 to 350 nm.

The solid ZIF-8 nanoparticles were then wrapped with the OCHT oligomer to form the solid core-shell ZIF-8@OCHT nanoparticles, as shown in electron microscopy images in Figure 3.5. Details of the synthesis are discussed in the experimental section. According to the FESEM (Figure 3.5a-b) and TEM images (Figure 3.5c-d and f), the size of the solid core-shell ZIF-8@OCHT nanoparticles is approximately 200-350 nm, and wrapping the OCHT shell does not damage the original polygonal morphology of solid ZIF-8. In fact, π–π interaction at the interface and free hydroxyl groups can help to coat the OCHT shell uniformly on the core nanoparticles. High-angle annular dark field-scanning TEM (HAADF-STEM) image (Figure 3.5g) with energy-dispersive X-ray spectroscopy (EDS) elemental mapping of C, Zn, N, P, and O in (Figure 3.5h-l) shows that the OCHT shell is well wrapped on the ZIF-8 solid core. Powder X-ray diffraction (PXRD) patterns confirm the formation of core-shell ZIF-8@OCHT nanoparticles without

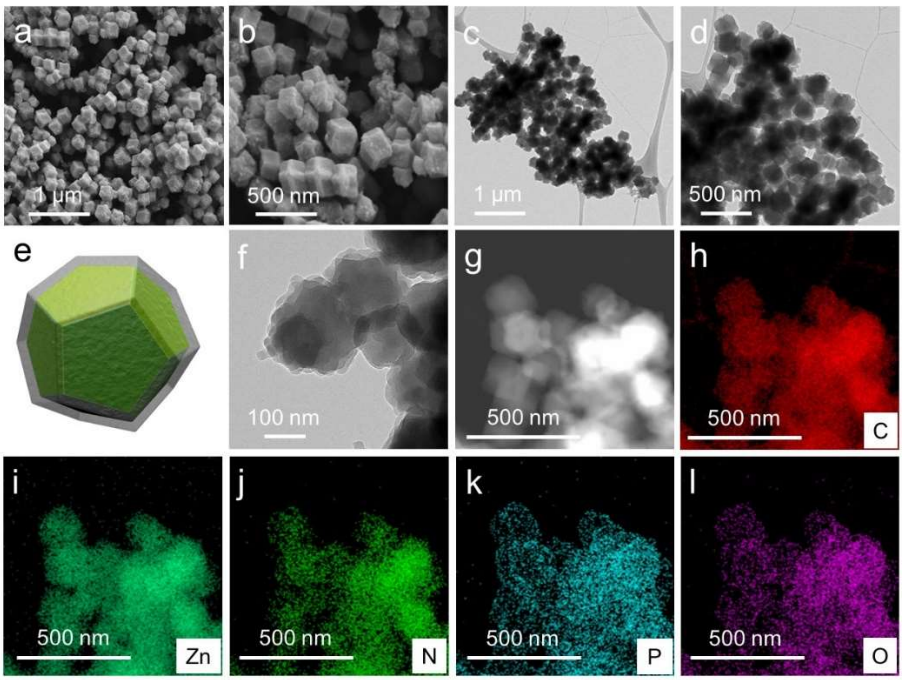


**Figure 3.5** Electron microscopy characterizations of core-shell ZIF-8@OCHT nanoparticles. FESEM (a and b) and TEM (c, d, and f) images with schematic illustration of single nanoparticle (e). HAADF-STEM image (g) with EDS elemental mapping for carbon (h), zinc (i), nitrogen (j), phosphorus (k), and oxygen (l).

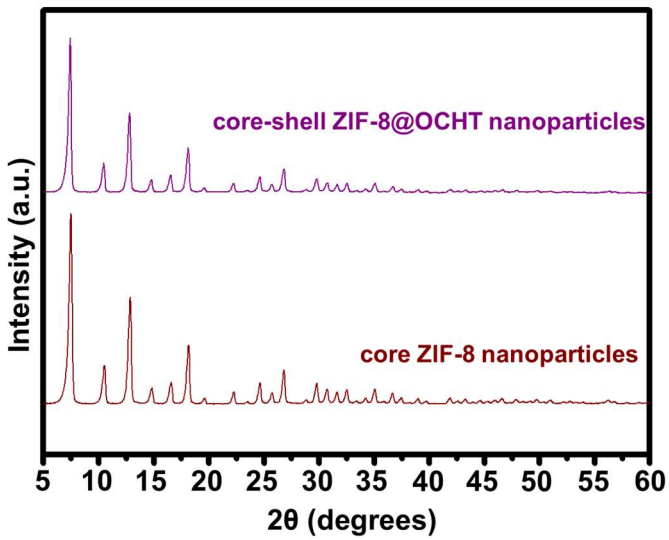


**Figure 3.6** Comparison of PXRD patterns for core ZIF-8 nanoparticles and core-shell ZIF-8@OCHT nanoparticles.

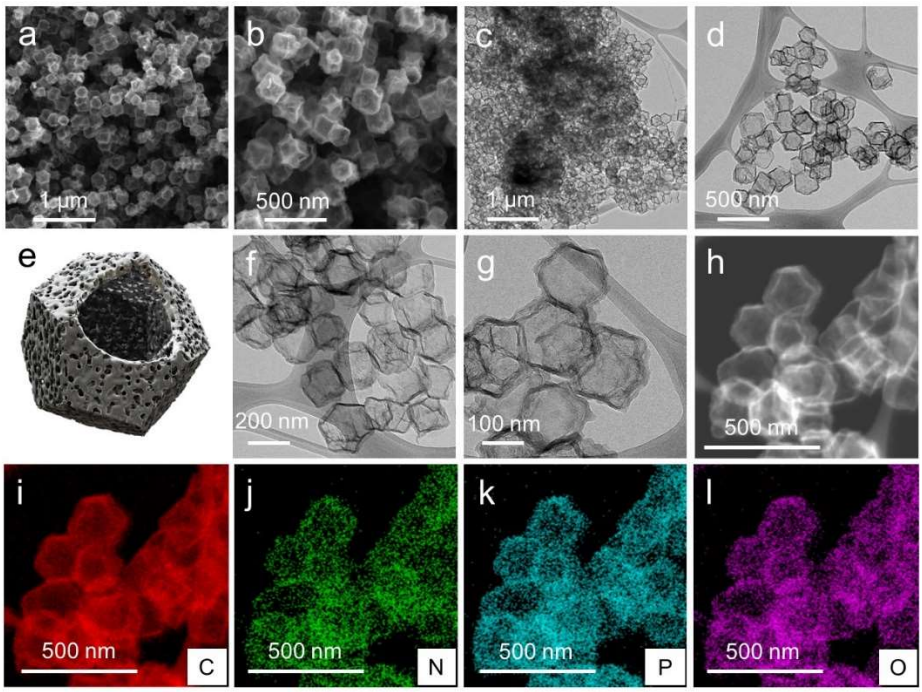


**Figure 3.7** Electron microscopy characterizations of N, P co-doped hollow carbon nanostructures. FESEM (a and b) and TEM (c, d, f, and g) images with schematic illustration of single nanoparticle (e). HAADF-STEM image (h) with EDS elemental mapping for carbon (i), nitrogen (j), phosphorus (k), and oxygen (l).

affecting the ZIF-8 structures (Figure 3.6). Figure 3.5e is the schematic representation of a single solid core-shell ZIF-8@OCHT nanoparticle.

These solid core-shell ZIF-8@OCHT nanoparticles were carbonized at 915 °C in inert atmosphere to synthesize NPHCs, as discussed in Figure 3.1a. FESEM images in Figure 3.7a-b and TEM images in Figure 3.7c-d, f-g clearly show that NPHC have hollow polygonal cavities with sizes varying from 200 to 350 nm, and the thickness of the NPHC shell is ~13 ± 2 nm. Figure 3.7e is the representative schematic of a single NPHC nanoparticle. The HAADF-STEM image and EDS elemental mapping of C, N, P, and O in Figure 3.7h-l show the formation of hollow carbon nanocages with even N, P co-doping. Furthermore, the solid core part (i.e. ZIF-8 nanoparticles) and the shell part (i.e. OCHT) were carbonized separately at the same annealing conditions of the synthesis of NPHCs. After annealing, imidazole molecules from organic part in the ZIF-8 nanoparticles were converted into N-doped carbon (NC). The size of the parent ZIF-8 nanoparticles was approximately maintained, but the polygonal shape became more irregular with increased surface roughness due to the porosity developed by the sublimation of zinc (Figure 3.4e-h). On the other hand, spherical OCHT nanoparticles (Figure 3.3a-d) after annealing were converted into N, P co-doped carbon

(NPC) nanostructures with irregular size and structure (Figure 3.3e-h). The synthesis of solid core-shell ZIF-8@OCHT nanoparticles followed by carbonization produces NPHCs, while the separate synthesis of the solid core ZIF-8 nanoparticles and OCHT nanoparticles followed by their respective carbonization produced NC and NPC, correspondingly (Figure 3.8). This control experiment underlines the importance of our unique wrap-bake-sublime approach to achieve porous and heteroatom co-doped carbon nanocages using solid ZIF-8 as the sacrificial template. Furthermore, the effect of the annealing temperature on the sublimation of zinc and the eventual formation of NPHCs was studied (Figure 3.9). NPHCs synthesized at 800 °C (NPHC-800) show a denser and more regularly formed shell, as can be seen from the FESEM and TEM images (Figure 3.10a-b and c-d, where the thickness of the shell was ~20 ± 3 nm), since the annealing temperature is lower than that of zinc sublimation. On the other hand, N, P co-doped hollow carbon nanostructures synthesized at 1000 °C (NPHC-1000), as shown by FESEM and TEM images in Figure 3.10e-f and g-h, (shell thickness: ~13 ± 2 nm), had an irregular and distorted form, because of higher annealing temperature.

### 3.3.2 Physicochemical Characterization of NPHCs

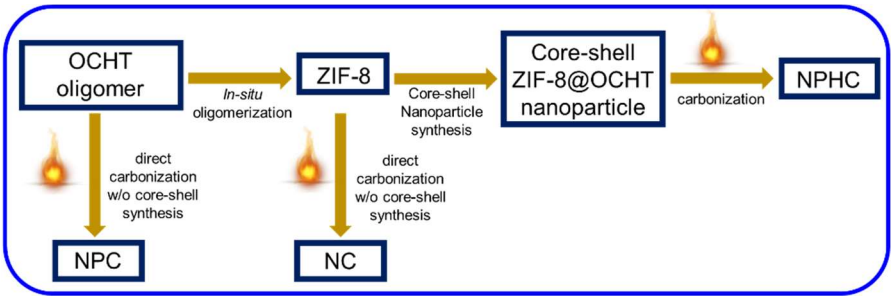


**Figure 3.8** Schematic representation for the synthesis of NC, NPC, and NPHC.

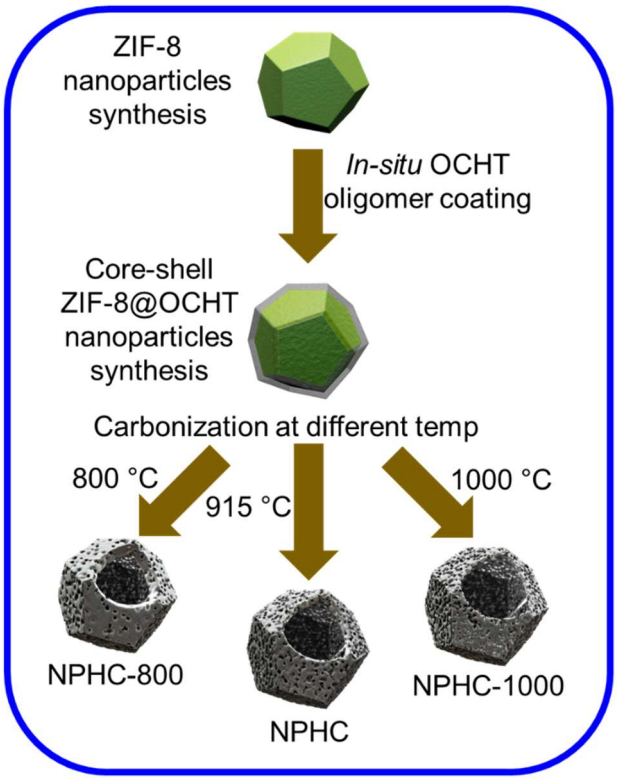


**Figure 3.9** Schematic illustration for the carbonization temperature dependent preparation of NPHC-800, NPHC, and NPHC-1000 starting from the same precursor of core-shell ZIF-8@OCHT nanoparticles at 800, 915, and 1000 °C, respectively.

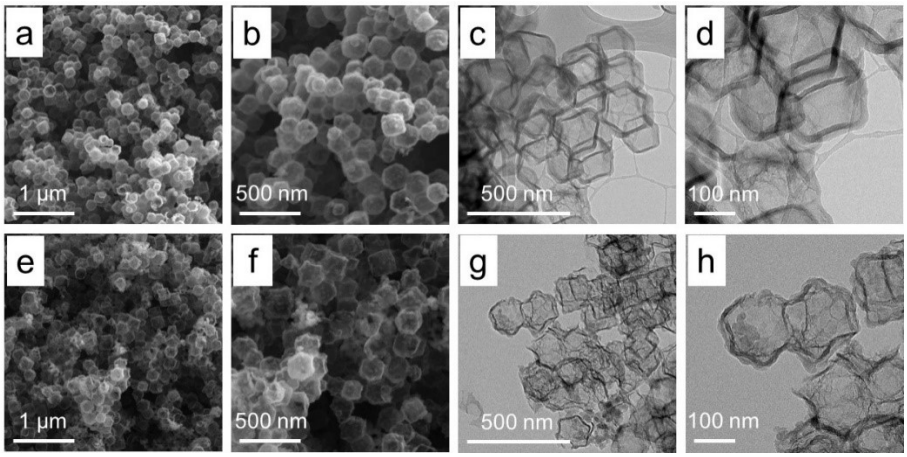


**Figure 3.10** FESEM (a, b) and TEM (c, d) images of NPHC-800. FESEM (e, f) and TEM (g, h) images of NPHC-1000.

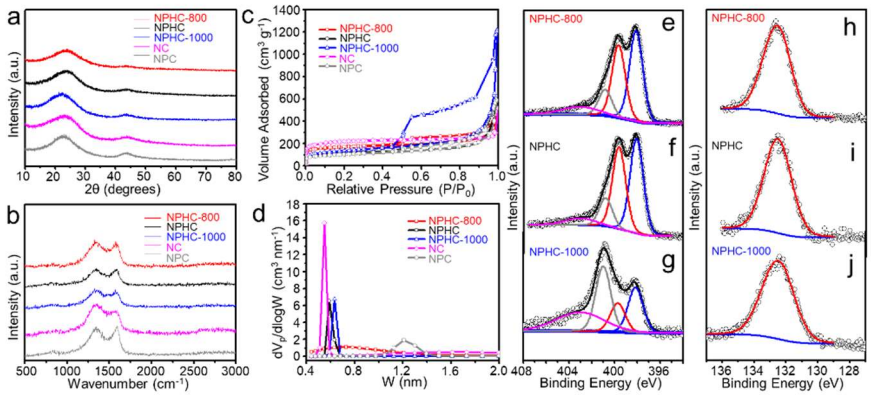


**Figure 3.11** Structural and materials characterization of various carbon nanomaterials. (a) PXRD analysis, (b) Raman spectra, (c) $N_2$ adsorption-desorption isotherms, and (d) pore size distributions calculated using the NLDFT method for NPHC-800, NPHC, NPHC-1000, NC, and NPC. High resolution XPS spectra of N1s (e), (f), and (g); and P2p (h), (i), and (j) for NPHC-800, NPHC, and NPHC-1000, respectively.

The structural, physical, and chemical properties of the synthesized carbon nanomaterials were investigated by multiple techniques, as shown in Figure 3.11. The PXRD patterns (Figure 3.11a) show two broad peaks centered at ~23.5 and ~44.5 ° for graphitic carbon (002) and (101) planes, which come from the amorphous nature of carbon due to the high-temperature annealing. The absence of any zinc-related peaks suggests complete sublimation of zinc during carbonization. Raman spectroscopy is a powerful tool to probe the quality of carbon nanomaterials. The Raman spectra in Figure 3.11b show two typical prominent peaks, one is the D band at ~1338 $cm^{-1}$ related to disordered carbon with defects, while the other peak at ~1589 $cm^{-1}$ is the G band for the ordered and $sp^2$-bonded carbon. Their intensity ratio ($I_D/I_G$) predicts the degree of defects introduced into the carbon nanomaterials. Increasing the annealing temperature during carbonization from 800 to 915 or 1000 °C induces more defects, as indicated by increasing $I_D/I_G$ ratio (1.05, 1.07, and 1.08, respectively). Meanwhile, this ratio for NC and NPC is 1.32 and 0.93, revealing more defects in NC compared to NPC. Based on the Brunauer-Emmett-Teller (BET) theory, the surface area of carbon nanomaterials was measured by $N_2$ adsorption-desorption isotherms and the pore size distribution (PSD) was calculated using a

non-local density functional theory (NLDFT) method (Figure 3.11c and d) Core (ZIF-8) carbonized carbon nanomaterial (NC) shows typical Type 1 isotherms, confirming the dominance of micropores. The other carbon nanomaterials show type 4 isotherms indicating the co-existence of micropores and mesopores. The specific surface area ($S_{BET}$) of NC is 800.16 $m^2g^{-1}$ with a micropore diameter of 0.54 nm in the PSD graph, while NPC has $S_{BET}$ of 355.19 $m^2g^{-1}$ with micropore diameter of 1.20 nm. NPHC-800 has micropores (diameter = 1.09 nm), as 800 °C was enough to sublime zinc while retaining regularity in the shell with few defects (as shown in the FESEM and TEM images and Raman spectrum). The NPHC has a micropore diameter of 0.58 nm, as the carbonization temperature of 915 °C is slightly higher than the zinc sublimation temperature. As a result, the zinc sublimed easily to cause irregularity and defects in the shell, which also corroborates observations in the FESEM/TEM images and Raman spectrum. NPHC-1000 nanoparticles have a micropore diameter of 0.63 nm, and the temperature of 1000 °C is high enough to impart more irregularity to the shell as observed in the micrographs and Raman spectrum. Increasing the carbonization temperature for the core-shell ZIF-8@OCHT nanoparticles caused more defects in the shells of NPHC *via* sublimation of zinc, with a minimum

micropore diameter observed at 915 °C. The $S_{BET}$ values of NPHC-800, NPHC, and NPHC-1000 are 600.47, 394.01, and 467.63 $m^2g^{-1}$, respectively.

The chemical composition of carbon nanomaterials was investigated by X-ray photoelectron spectroscopy (XPS). High resolution N1s XPS analysis of NPHC-800, NPHC, and NPHC-1000 (Figure 3.11e, f, and g, respectively) shows the presence of pyridinic N (398.1 eV), pyrrolic N (399.65 eV), graphitic N (400.85 eV), and oxidized N (403.1 eV) in all the samples. The N atomic percentages according to XPS data are 7.76 at%, 6.92 at%, and 2.56 at%, respectively (wide scan in Figure 3.12). High resolution P2p XPS analysis of these samples (Figure 3.11h, i, and j) shows the presence of P at 132.65 eV in all of them, with a respective atomic percentage of 0.69 at%, 0.68 at%, and 0.65 at%. The respective calculated N/P ratio for NPHC-800, NPHC, and NPHC-1000 is 11.24, 10.17, and 3.93, which indicates decreasing ratio upon increasing the carbonization temperature from 800 to 1000 °C. In comparison, the co-doped carbon nanomaterial NPC, which was derived directly by carbonization of OCHT without using ZIF-8 template, has the lowest N/P ratio, of 0.70 (Figure 3.13). Clearly, the imidazole molecules from the ZIF-8 nanoparticle cores contributed extra nitrogen to the prepared

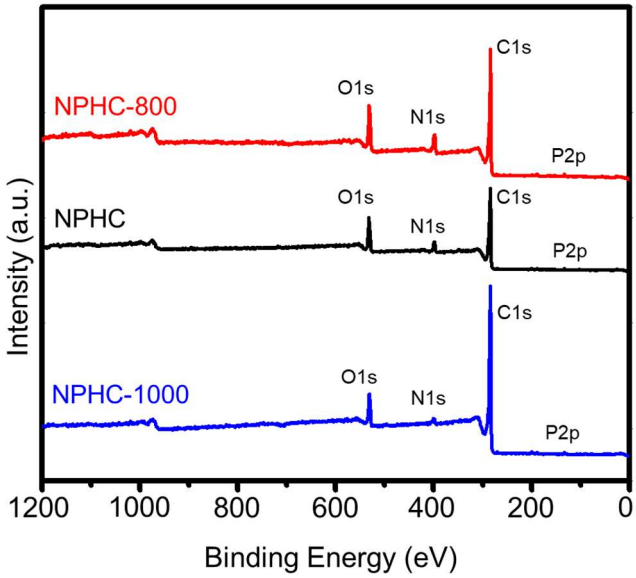


**Figure 3.12** Wide-scan XPS spectra of NPHC-800, NPHC, and NPHC-1000.

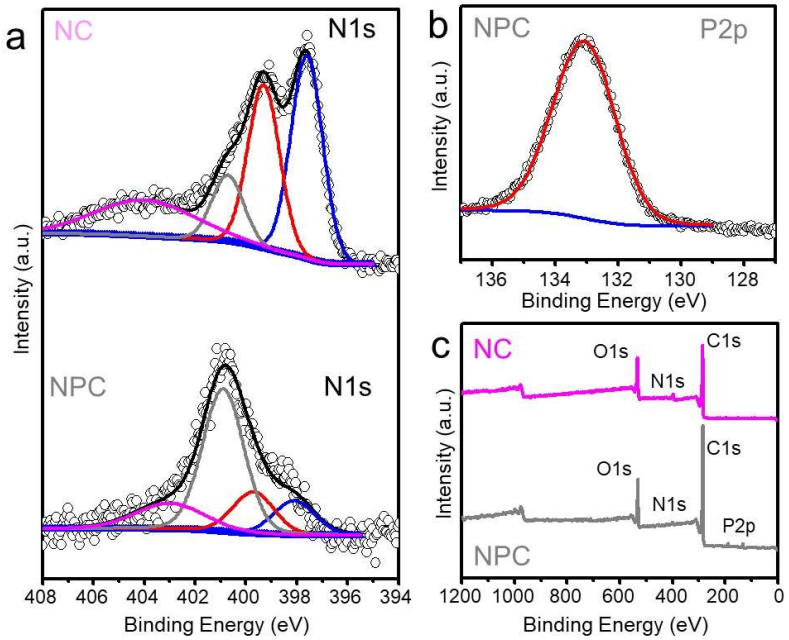


**Figure 3.13** High resolution (a) N1s spectra of NC and NPC, (b) High resolution P2p spectra of NPC, and (c) Wide-scan XPS spectra of NC and NPC, respectively.

carbon nanomaterial. Almost all the zinc sublimed from the above NPHCs after carbonization and subsequent acid washing.

### 3.3.3 Micropore Engineering of NPHCs

The three carbon nanomaterials discussed above (NPHC-800, NPHC, and NPHC-1000) were synthesized from the same solid core-shell ZIF-8@OCHT nanoparticles, in which the OCHT shell was formed with equimolar HCTP and HHTP (0.29 mM each) and 1 mL TEA. Eventually, the microporosity in NPHC was controlled by simply varying the amount of coated OCHT (in terms of HCTP, HHTP, and TEA) to form three additional types of solid core-shell ZIF-8@OCHT-x nanoparticles (x represents the amount of OCHT precursors used, relative to that of NPHC). For x = 0.5, 2, and 3 (Figure 3.14 and Figure 3.15), the amounts of reagents were: 0.145 mM HCTP-HHTP with 0.5 mL TEA, 0.58 mM HCTP-HHTP with 2 mL TEA, and 0.87 mM HCTP-HHTP with 3 mL TEA, respectively. The uniformity of shape and size of the solid core-shell nanoparticles was verified with the FESEM and TEM images (Figure 3.16a-b and c-d for ZIF-8@OCHT-0.5, Figure 3.17a-b and c-d for ZIF-8@OCHT-2, and Figure 3.18a-b and c-d for ZIF-8@OCHT-3, respectively). Carbonization of these ZIF-8@OCHT-x nanomaterials was

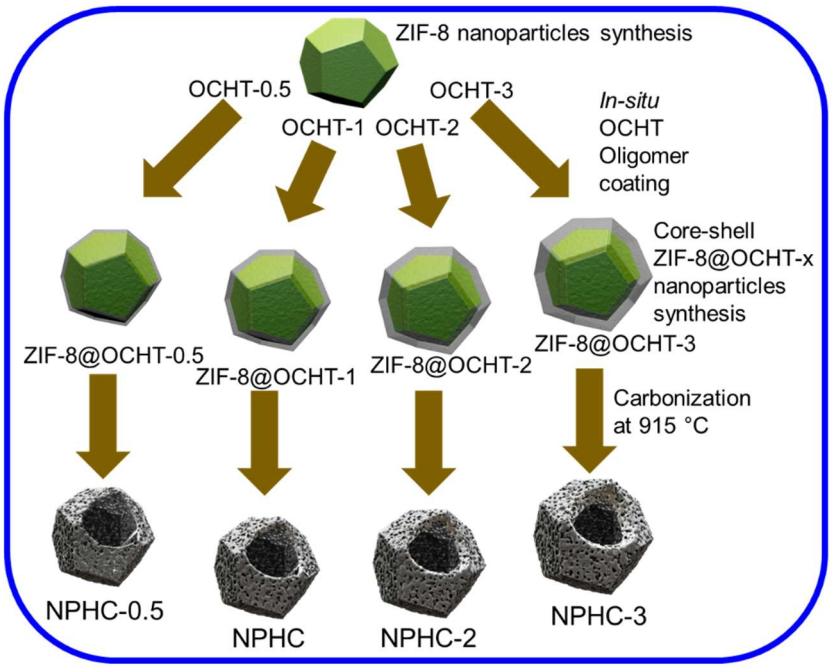


**Figure 3.14** Schematic illustration for the OCHT amount dependent synthesis of NPHC-0.5, NPHC, NPHC-2, and NPHC-3 starting from core ZIF-8 nanoparticles followed by coating of various amounts (OCHT-0.5, OCHT-1, OCHT-2, and OCHT-3) of OCHT during *in-situ* oligomerization to achieve core-shell nanoparticles of ZIF-8@OCHT-0.5, ZIF-8@OCHT-1, ZIF-8@OCHT-2, and ZIF-8@OCHT-3 and finally by carbonization at exactly same conditions of 915 °C temperature, to achieve NPHC-0.5, NPHC, NPHC-2, and NPHC-3, respectively.

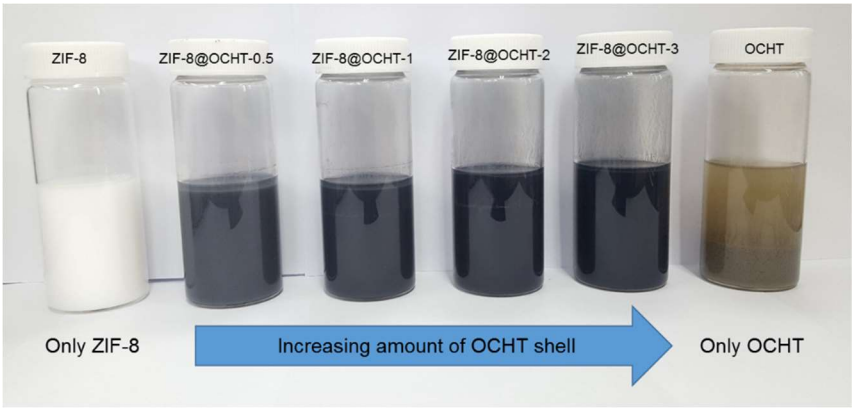


**Figure 3.15** Optical photographs of as-synthesized various nanoparticles starting from left to right of only ZIF-8 core, core-shell ZIF-8@OCHT-0.5, core-shell ZIF-8@OCHT-1, core-shell ZIF-8@OCHT-2, core-shell ZIF-8@OCHT-3, and only OCHT. As the amount of OCHT increases from 0.5 to 3, the color of core-shell nanoparticles becomes darker.

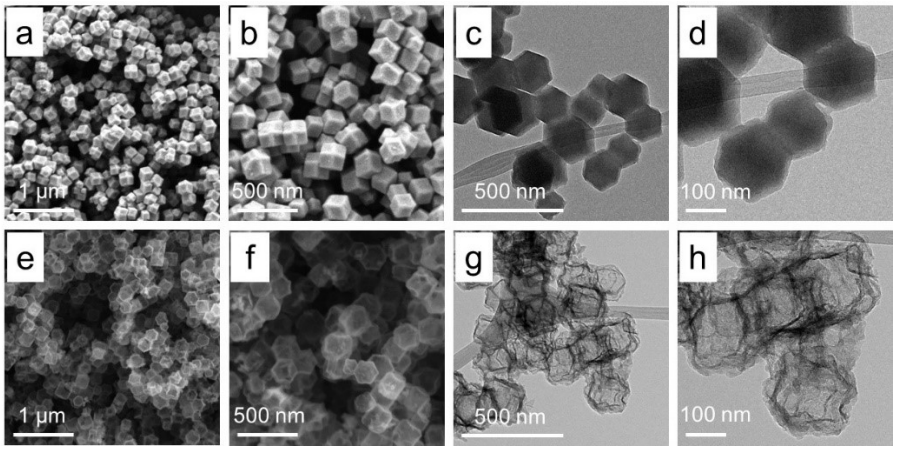


**Figure 3.16** FESEM (a, b) and TEM (c, d) images of core-shell ZIF-8@OCHT-0.5 nanoparticles, respectively. FESEM (e, f) and TEM (g, h) images of NPHC-0.5.

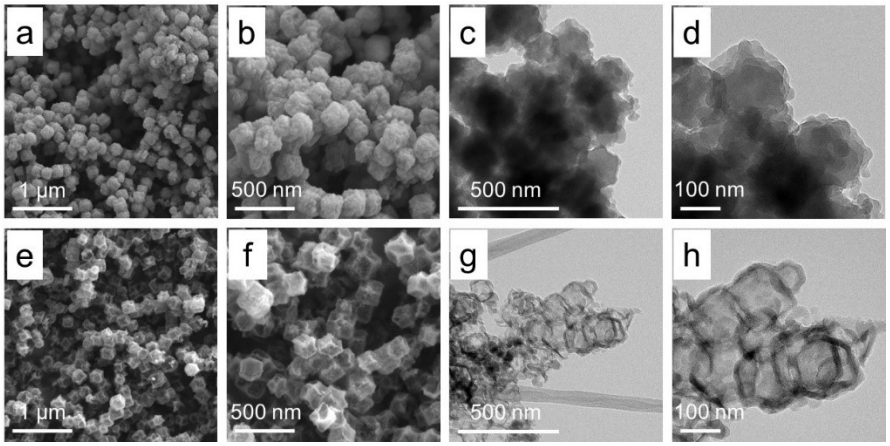


**Figure 3.17** FESEM (a, b) and TEM (c, d) images of core-shell ZIF-8@OCHT-2 nanoparticles, respectively. FESEM (e, f) and TEM (g, h) images of NPHC-2.

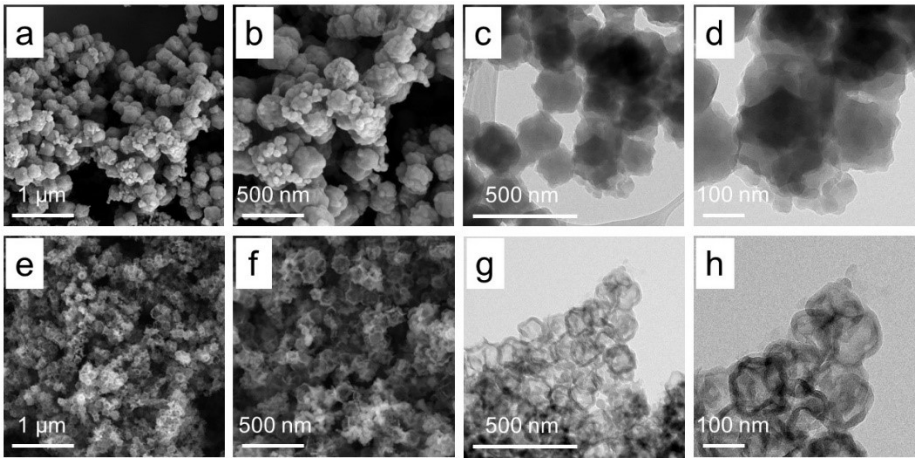


**Figure 3.18** FESEM (a, b) and TEM (c, d) images of core-shell ZIF-8@OCHT-3 nanoparticles, respectively. FESEM (e, f) and TEM (g, h) images of NPHC-3.

carried out under the same conditions as for NPHC (915 °C in inert atmosphere). The obtained co-doped carbon nanocages are denoted as NPHC-0.5, NPHC-2, and NPHC-3, respectively. The FESEM and TEM show that the minimum shell thickness increased from ~10 ± 2 nm (Figure 3.16e-f and g-h) to ~15 ± 2 nm (Figure 3.17e-f and g-h) and ~16 ± 2 nm (Figure 3.18e-f and g-h) by changing the concentrations of HCTP and HHTP relative to NPHC and PXRD patterns confirmed the graphitization of carbon (Figure 3.19). The $I_D/I_G$ ratios calculated from Raman data for NPHC-0.5, NPHC, NPHC-2, and NPHC-3 were 1.04, 1.07, 1.08, and 1.21, respectively, revealing that more defects were introduced upon thickness of the OCHT shell (Figure 3.20). High-resolution N1s XPS analysis shows four kinds of nitrogen species (pyridinic, pyrrolic, graphitic, and oxidized N at the same binding energies) in NPHC-0.5, NPHC-2, and NPHC-3, similar to NPHCs (Figure 3.21a) and the N atomic percentage measured by XPS is 7.31 at%, 1.9 at%, and 2.1 at%, respectively. High-resolution P2p XPS analysis (Figure 3.21b) also shows the presence of P (132.65 eV) in all samples. The XPS atomic percentage of P was measured to be 1.03 at%, 0.77 at%, and 0.93 at%, resulting in a N/P ratio of 7.09, 2.41, and 2.23

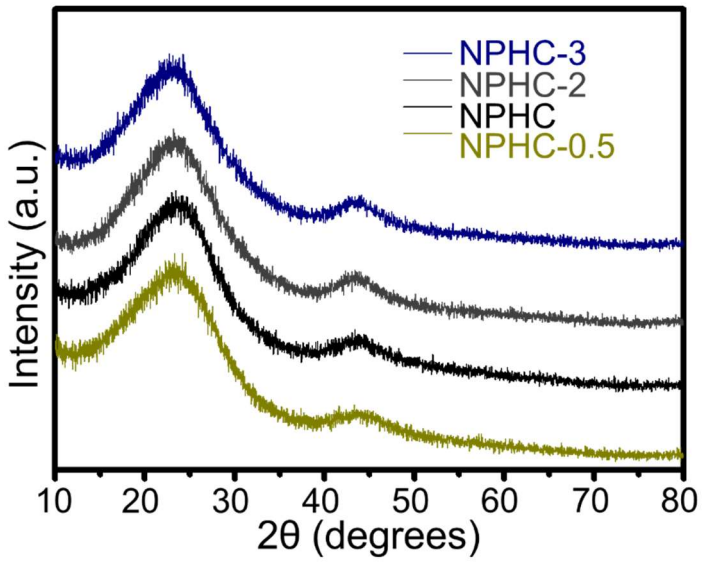


**Figure 3.19** Comparison of PXRD patterns of NPHC-0.5, NPHC, NPHC-2, and NPHC-3.

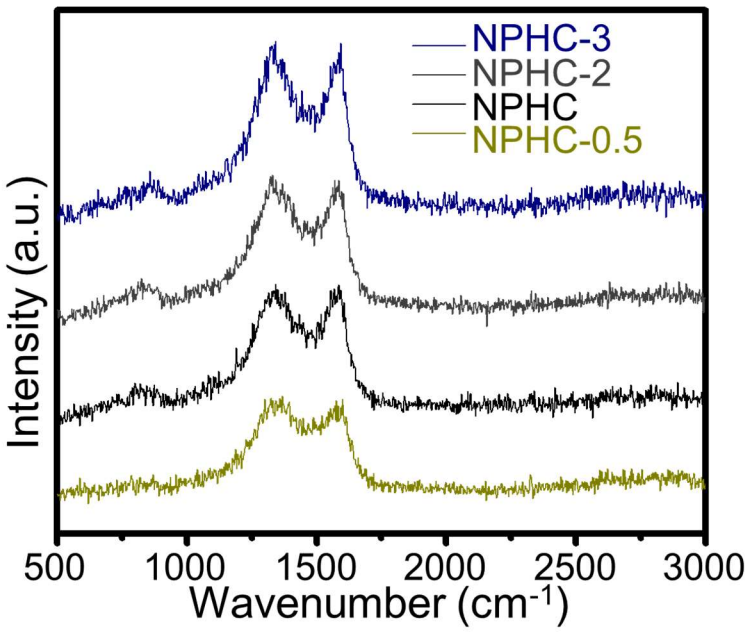


**Figure 3.20** Comparison of Raman spectra of NPHC-0.5, NPHC, NPHC-2, and NPHC-3.

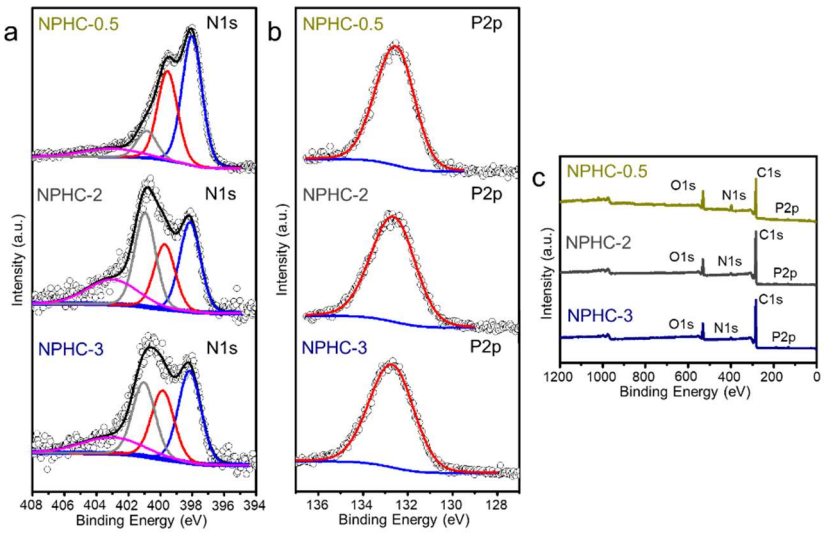


**Figure 3.21** High resolution (a) N1s and (b) P 2p, and (c) wide-scan XPS spectra of NPHC-0.5, NPHC-2, and NPHC-3, respectively.

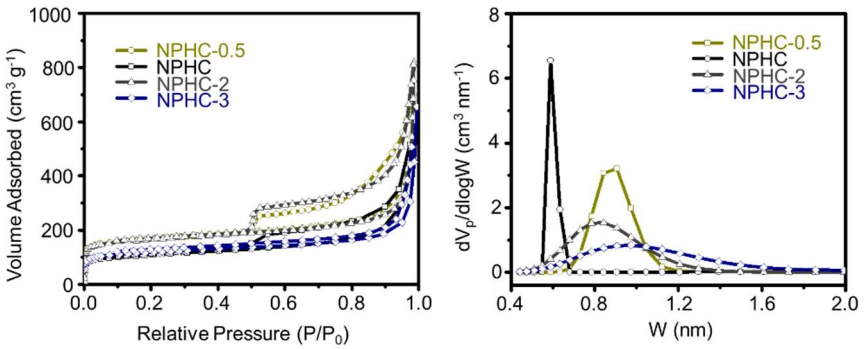


**Figure 3.22** Comparison of (a) $N_2$ adsorption-desorption isotherms and (b) pore size distributions calculated from NLDFT method for NPHC-0.5, NPHC, NPHC-2, and NPHC-3.

for NPHC-0.5, NPHC-2, and NPHC-3, respectively. $N_2$ adsorption-desorption analysis (Figure 3.22a) of the NPHC-x samples indicates Type 4 isotherms, and the narrow peaks in their PSDs (Figure 3.22b) reveal precise micropore distribution. Micropore diameters of 0.90, 0.58, 0.84, and 0.97 nm and $S_{BET}$ values of 642.93, 394.01, 611.16, and 435.57 $m^2g^{-1}$ were calculated for NPHC-0.5, NPHC, NPHC-2, and NPHC-3, respectively. Hence, by varying the amount of OCHT shell on the core-shell nanoparticles, the microporosity of NPHC samples under the same conditions of carbonization could be finely tuned, due to the shell's different levels of resistance against zinc sublimation. However, the overall surface area was less affected.

### 3.3.4 Gram-Scale Synthesis of NPHCs

Our wrap-bake-sublime approach can easily be scaled up to achieve gram-scale production of NPHC (NPHC-GS). For the scaled up synthesis one liter of reaction mixture for the synthesis of ZIF-8 (750 mL of methanolic solution of MIZ and 250 mL methanolic solution of zinc nitrate) was used, which is ~12.5 times the amounts in the aforementioned synthesis. 1.46 g of the final product was obtained (Figure 3.23).

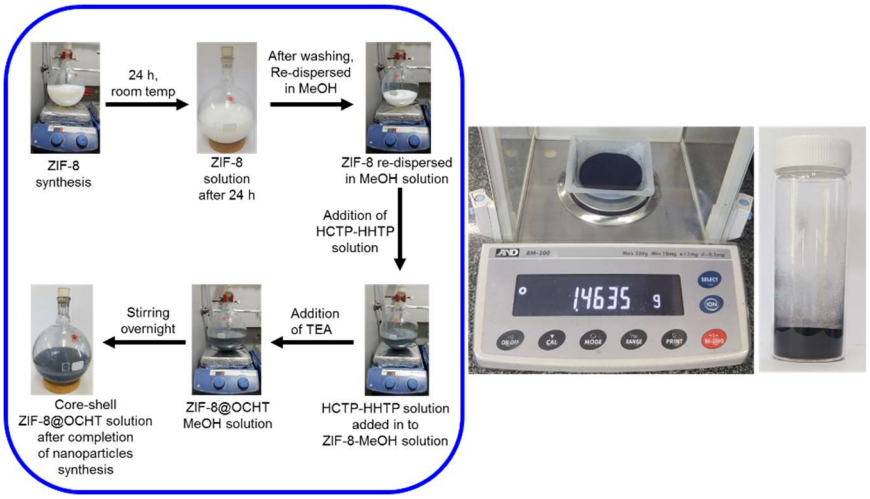


**Figure 3.23** Gram-scale synthesis of NPHC in the laboratory. Starting from 1 liter batch of ZIF-8 core nanoparticles up to the synthesis of core-shell ZIF-8@OCHT solution is shown in each step with optical photographs followed by description in between. Right side photograph shows NPHC-GS after carbonization followed by washings which gives ~1.46 g powder.

### 3.3.5 Electrochemical Performance of NPHCs

Supercapacitors are the energy storage devices with ultra-fast charge-discharge rate along with important features such as high power density, safe operations over wide temperature range, and long cycle life and stability.[7-9] Electrochemical double layer capacitors (EDLCs) are a type of supercapacitors where energy is stored by physical adsorption of electrolyte ions on the surface of the electrodes. It is commonly stated that the performance of EDLCs (i.e. specific capacitance) increases with increasing specific surface area. However, the correlation between these two is not linear, as the PSD (especially the micropore diameter) of the electrodes also has a significant role. When the micropores of the electrodes have the size closer to the size of the electrolyte ions, the maximum area of the micropores can be accessed for the utilization by the electrolyte ions, while too small or too large micropores can lower the utilization of the micropores.[10-11] The pioneering work by Gogotsi and Simon *et al.* showed that a maximum specific capacitance in EDLCs is achieved when the micropore size in the electrode is very close to the ion size of the electrolyte.[10-11] Along with microporosity, heteroatom(s) doping in the carbon nanomaterials is also important, because it can dramatically change the electron donor-acceptor features

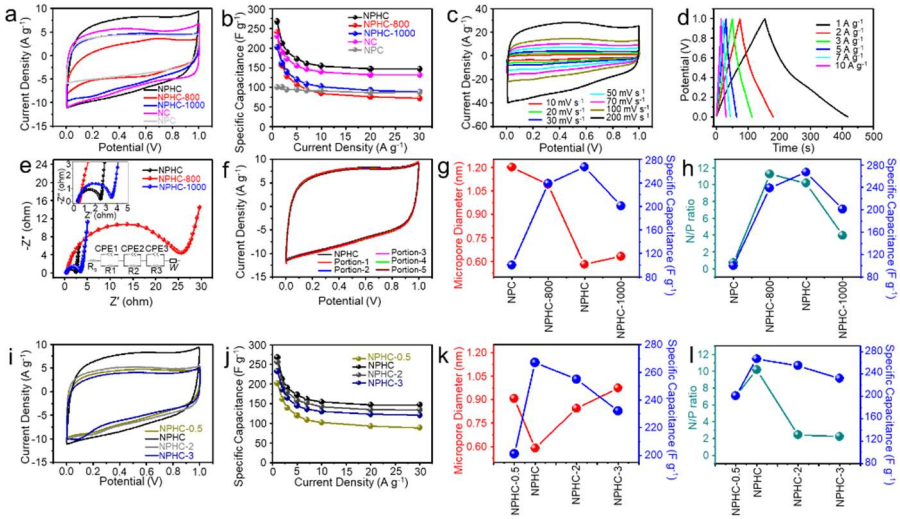


**Figure 3.24** Supercapacitor performance of various carbon nanomaterials. Comparisons of (a) CVs with scan-rate of 50 mV $s^{-1}$ within a potential range of 0.0 to 1.0 V and (b) specific capacitance with various current densities from 1 to 30 A $g^{-1}$ of NPHC-800, NPHC, NPHC-1000, NC, and NPC. (c) CVs at different scan-rates from 1 to 200 mV $s^{-1}$ and (d) Galvanostatic charge-discharge curves with current densities from 1 to 10 A $g^{-1}$ for NPHC. (e) Nyquist comparison plot of NPHC-800, NPHC, and NPHC-1000. Inset shows the lower series resistance values from the impedance data in high frequency range of NPHC-800, NPHC, and NPHC-1000. (f) CVs with scan-rate of 50 mV $s^{-1}$ within a potential range of 0.0 to 1.0 V for various portions (1 to 5) of gram-scale synthesized NPHC (NPHC-GS) compared with typical small

scale batch (NPHC). Plot for dependency of specific capacitance values on (g) micropore diameter and (h) N/P ratio for NPC, NPHC-800, NPHC, and NPHC-1000. The second set data to compare (i) CVs with scan-rate of 50 mV $s^{-1}$ within a potential range of 0.0 to 1.0 V and (j) Specific capacitance with various current densities from 1 to 30 A $g^{-1}$ of NPHC-0.5, NPHC, NPHC-2, and NPHC-3, respectively. Plot for dependency of specific capacitance values on (k) micropore diameter and (l) N/P ratio for NPHC-0.5, NPHC, NPHC-2, and NPHC-3. All the electrochemical measurements above were done using 1.0 M $H_2SO_4$ with reference electrode Ag/AgCl.

and create extra functional groups on the carbon surface for a higher specific capacitance.[12-14] For example, it is known that the low quantum capacitance in graphene-based electrode materials in supercapacitors is due to the scarcity of states near the Fermi level.[15] According to the first principle calculation by Mousavi-Khoshdel *et al.,*[15] compared to pristine and singly doped graphene; co-doping of heteroatoms in graphene creates new electronic states near the Fermi level, and induces more electrical charge which enhances quantum capacitance. This co-doping of heteroatoms in graphene evidently increases energy density and specific capacitance of supercapacitor electrodes. Considering these findings, our novel wrap-bake-sublime approach for the synthesis of NPHC meets all the criteria for electrode materials in supercapacitors such as tunable microporosity, high surface area, and heteroatom co-doping.

The capacitive performances of our carbon nanomaterials was investigated using Ag/AgCl, Pt mesh, and 1.0 M $H_2SO_4$ as the reference electrode, counter electrode, and electrolyte, respectively. Figure 3.24a shows the steady-state cyclic voltammograms (CVs) of NPHC, NPHC-800, NPHC-1000, NC, and NPC at a scan rate of 50 mV $s^{-1}$ within a potential range from 0.0 V to 1.0 V. These CVs are all nearly rectangular

shape, and NPHC (carbonization temperature: 915 °C, micropore diameter: 0.58 nm, N/P ratio: 10.17) shows the largest integrated area. In contrast, the smaller integrated area of NPHC-1000 indicates that a higher carbonization temperature caused destruction of the microporous structure, increasing the micropore diameter to 0.63 nm. Moreover, NPHC-800 shows more distortion in the rectangular CV shape, indicating its micropore diameter (1.09 nm) is too large, and 800 °C is insufficient to activate the carbon. The same trend was observed in the electrochemical impedance spectroscopy (EIS) data (frequency range from 0.01 Hz to 1 MHz, Figure 3.24e). The equivalent circuit shown in the inset was used for fitting the EIS spectra, where $R_s$ is the combined resistance (intrinsic resistance and contact resistance); W is the Warburg impedance related to the vertical line in the low frequency region; $R_1$, $R_2$, and $R_3$ are the charge transfer resistances related to the semicircle in the high frequency region; and CPE is the constant phase element. Although NPHC has a similar $R_s$ value compared to NPHC-800 and NPHC-1000, it shows improved values for $R_{ct}$ and W. The carbon nanomaterials of NC and NPC also have a nearly rectangular shape during CV, but the areas are smaller than that of NPHC, underlining the advantage of our wrap-bake-sublime approach compared to the separate carbonization of

ZIF-8 and OCHT (which produces NC and NPC, respectively). The specific capacitance data in Figure 3.24b were calculated by using equation (3.1). At current rate of 1 A $g^{-1}$, the specific capacitance of NPHC is the highest (267 F $g^{-1}$) among all carbon nanomaterials, and this value becomes 146 F $g^{-1}$ at the higher current rate of 30 A $g^{-1}$, (54 % capacitance retention). Other carbon nanomaterials show lower specific capacitance, in accordance with the CV data. The CVs of NPHC at scan rates from 10 to 200 mV $s^{-1}$ are shown in Figure 3.24c. The rectangular shape is maintained at high scan rates without any distortion, suggesting good transport properties of NPHCs due to the proper micropore size.

Furthermore, the galvanostatic charge/discharge (GCD) curves of NPHCs at current densities from 1 to 10 A $g^{-1}$ were measured in order to investigate the electrochemical performance accurately. As shown in Figure 3.24d, the almost triangular-shaped curves indicate stable reversible charge-discharge reaction, in accordance with the CV results. To ensure the quality of the gram-scale co-doped carbon nanocages, the electrochemical activity of NPHC-GS was compared to that of NPHCs. Specifically, various portions (labeled 1-5) of NPHC-GS were tested at the scan rate of 50 mV $s^{-1}$ under exactly the same conditions (Figure 3.24f). The corresponding CVs show excellent overlaps with that of

NPHC-GS, validating that the gram-scale synthesis of NPHC was successful. Interestingly, the dependence of specific capacitance values (measured at 1 A $g^{-1}$) for various carbon nanomaterials with their respective micropore diameter were shown in Figure 3.24g; the specific capacitance increases (100, 239, and 267 F $g^{-1}$) with decreasing micropore diameter (1.20, 1.09, and 0.58 nm) for NPC, NPHC-800, and NPHC, respectively. NPHC-1000 shows an anomalous decrease in specific capacitance (201 F $g^{-1}$) for the micropore diameter of 0.63 nm. It can be concluded that the microporosity and the defects introduced in carbon nanomaterials tuned by carbonization at various temperature are important in determining the capacitance. Besides, the N/P ratio also affects the capacitance values. From Figure 3.24h, NPC has the lowest N/P ratio (0.7) and specific capacitance (100 F $g^{-1}$). NPHC-800 and NPHC have the respective N/P ratios of 11.24 and 10.17 and specific capacitances of 239 and 267 F $g^{-1}$ while, NPHC-1000 has N/P ratio of 3.93 with specific capacitance of 201 F $g^{-1}$.

We investigate the dependence of capacitive performance on micropore diameter and N/P ratio when different amounts of OCHT were used in the core-shell ZIF-8@OCHT-x nanoparticles. Under the same electrochemical condition, the CVs of NPHC-0.5, NPHC-2, NPHC-3,

and NPHC all show nearly rectangular shapes, with the largest integrated area observed for NPHC (Figure 3.24i). Figure 3.24j plots the specific capacitance for NPHC-x measured at various current densities (1-30 A $g^{-1}$), and Figure 3.24k shows the specific capacitance values measured at 1 A $g^{-1}$ vs. micropore diameters for NPHC-x. In Figure 3.24k, from NPHC-0.5 to NPHC there is an increase in the specific capacitance from 201 to 267 F $g^{-1}$ while the micropore diameter decreases from 0.90 to 0.58 nm. Otherwise, the specific capacitance tends to decrease upon increasing the micropore diameter: 267, 255, and 232 F $g^{-1}$ with the micropore diameters of 0.58, 0.84, and 0.97 nm for NPHC, NPHC-2, and NPHC-3, respectively. Again, the maximum specific capacitance is correlated with the minimum micropore diameter in the case of NPHC. Therefore, we conclude that at the carbonization temperature and the resulting microporosity is critical for the capacitance of NPHC-x. In the sample with the highest capacitance, the micropore diameter (0.58 nm) is close to that of hydrated $H^+$ ions.[10-11,16-22] Similar to the micropore diameter, the N/P ratio in NPHC-x also has a significant role in the specific capacitance. From the plot in Figure 3.24l (N/P ratio vs. specific capacitance), NPHC displays both the highest N/P ratio (10.17) and specific capacitance (267 F $g^{-1}$), underlining the importance of a proper

amount of heteroatom co-doping in carbon nanomaterials.

### 3.3.6 Application of NPHC as Flexible All-Solid-State-Supercapacitor

To explore the potential of the N, P co-doped hollow carbon nanostructures for real industry applications, the NPHC was used as two symmetric electrodes to make an all-solid-state-supercapacitor (ASSS). The scheme of the ASSS device is shown in Figure 3.25a. Figure 3.25b shows the CVs of the symmetric supercapacitor at varying scan rates from 10 to 200 mV $s^{-1}$. There is no major distortion in the shape of CVs at high scan rate, suggesting high rate capability. Furthermore, GCD analysis at various current densities (Figure 3.25c) gave results in good agreement with the CVs. The capacitance calculated from GCD is 58 F $g^{-1}$ at a current density of 1 A $g^{-1}$ (Figure 3.25d). Moreover, the device is highly flexible and bendable, as shown in the photograph (inset of Figure 3.25e). The CV curves show that the capacitance in the flat state was well-retained even after the device was bent 180° (Figure 3.25e). To enhance the operating voltage and total capacitance, multiple devices could be integrated in parallel or series connections (Figure 3.25f). Figure 3.25g is the Ragone plot that compares our device with other

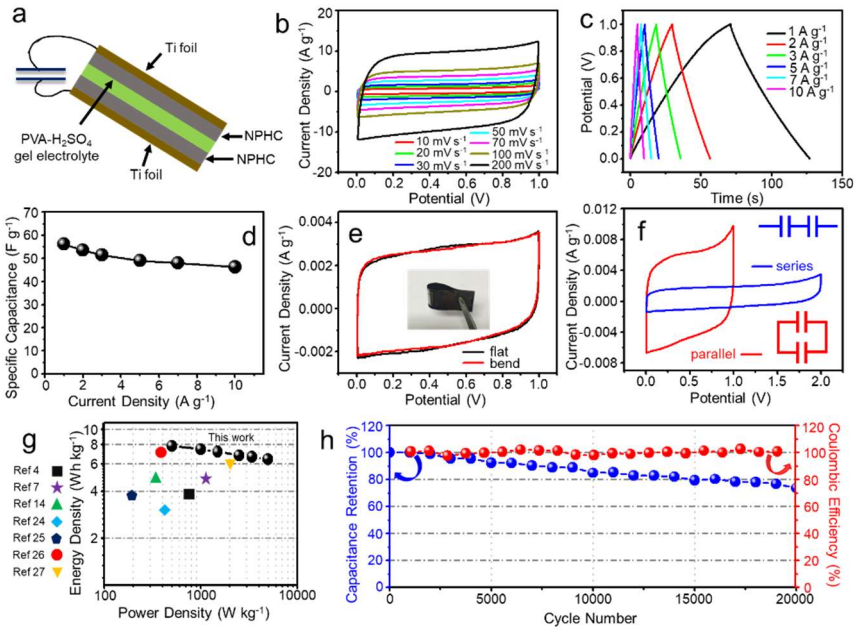


**Figure 3.25** All-solid-state-supercapacitors (ASSSs) performance of N, P co-doped hollow carbon nanostructures. (a) Schematic illustration, (b) Scan-rate dependent CVs varying from 10 to 200 mV $s^{-1}$ within a potential range of 0.0 - 1.0 V, (c) Galvanostatic charge-discharge, (d) Specific capacitance with various current densities from 1 to 10 A $g^{-1}$, (e) CVs under flat and bend condition at a scan rate of 50 mV $s^{-1}$ of ASSSs. (f) Integration of the device with parallel or series connections. (g) Ragone plot. (h) Cycle stability performance data of the ASSSs.

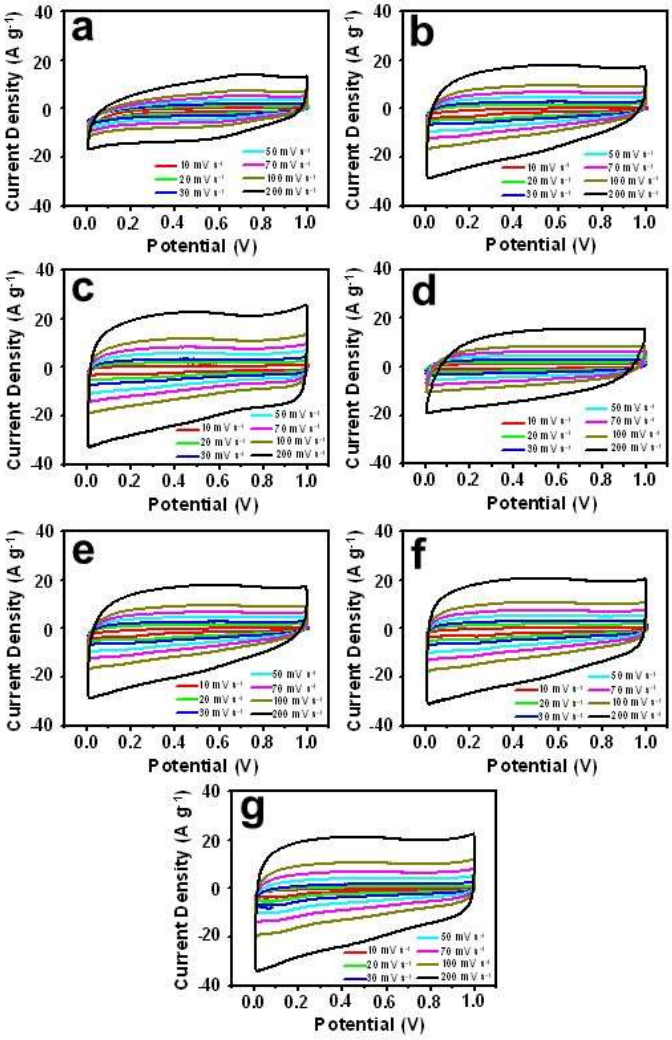


**Figure 3.26** Comparison of CVs of (a) NPHC-800, (b) NPHC-1000, (c) NC, (d) NPC, (e) NPHC-0.5, (f) NPHC-2, and (g) NPHC-3, respectively at various scan-rates from 10-200 mV $s^{-1}$ using 1.0 M $H_2SO_4$ electrolyte with Ag/AgCl reference electrode.

reported symmetric supercapacitors. Our device shows a maximum energy density of 7.8 Wh $kg^{-1}$ and maximum power density of 4952.5 W $kg^{-1}$. Both values are much higher than those of other similar supercapacitors.[4,7,14,24-27] Finally, cycle stability is an important criteria for rechargeable devices in practical applications. The charge-discharge test was conducted at a current density of 10 A $g^{-1}$ for 20,000 cycles displaying good cycle stability, with a capacitance retention of ~75% (Figure 3.25h).

## 3.4 Conclusion

To the best of our knowledge, this study represents the first demonstration of a wrap-bake-sublime approach for the synthesis of N, P co-doped hollow carbon nanostructures (NPHCs) with tunable porosity. Solid ZIF-8 nanoparticles are used as cores, around which a heteroatom-containing OCHT is wrapped to create a shell of varying thickness. The resulting core-shell ZIF-8@OCHT-x nanoparticles are carbonized at high temperatures. The microporosity of the derived NPHCs could be finely tuned, since the thickness of the shell affect the escape tendency of sublimed zinc from the ZIF-8 core. The use of NPHCs as supercapacitor electrodes demonstrated that the electrochemical performance depends on the microporosity of NPHCs. The highest specific capacitance (267 F $g^{-1}$ at current density of 1 A $g^{-1}$) is achieved at a micropore diameter of 0.58 nm, which is close to the size of hydrated $H^+$ ions. The amounts of N and P co-doping in NPHCs also has significant effect on the electrochemical properties. The correlation of electrochemical performance with microporosity and the ratio of N and P co-doping in NPHCs is documented. The NPHCs were used in symmetric flexible all-solid-state-supercapacitors, showing remarkable specific capacitance, high energy and power densities, and long-term

cycling durability (75% capacity retention after 20,000 cycles). Furthermore, the successful gram-scale production of NPHCs without compromising the electrochemical activity guarantees its potential for various industrial energy applications such as supercapacitors, Li-ion batteries, electrocatalysts, etc.

**Most of the contents of this chapter were published in the article, "Microporosity-Controlled Synthesis of Heteroatom Co-doped Carbon Nanocages by Wrap-Bake-Sublime Approach for Flexible All-Solid-State-Supercapacitors"

*Advanced Functional Materials*, just accepted

## 3.5 References


[1] J. Zhang, Z. Zhao, Z. Xia, L. Dai, *Nat. Nanotech.* **2015**, *10*, 444.

[2] S. Yang, C. Cao, Y. Sun, P. Huang, F. Wei, W. Song, *Angew. Chem. Int. Ed.* **2015**, *54*, 2661; *Angew. Chem.* **2015**, *127*, 2699.

[3] J. Zhou, L. Meng, X. Feng, X. Zhang, Q. Lu, *Angew. Chem. Int. Ed.* **2010**, *49*, 8476; *Angew. Chem.* **2010**, *122*, 8654.

[4] L. Zhu, Y. Xu, W. Yuan, J. Xi, X. Huang, X. Tang, S. Zheng, *Adv. Mater.* **2006**, *18*, 2997.

[5] A. P. Côté, A. I. Benin, N. W. Ockwig, M. O'Keeffe, A. J. Matzger, O. M. Yaghi, *Science* **2005**, *310*, 1166.

[6] H. M. El-Kaderi, J. R. Hunt, J. L. Mendoza-Cortés, A. P. Côté, R. E. Taylor, M. O'Keeffe, O. M. Yaghi, *Science* **2007**, *316*, 268.

[7] R. R. Salunkhe, J. Tang, Y. Kamachi, T. Nakato, J. H. Kim, Y. Yamauchi, *ACS Nano* **2015**, *9*, 6288.

[8] Q. Wang, J. Yan, Z. Fan, *Energy Environ. Sci.* **2016**, *9*, 729.

[9] D. Sheberla, J. C. Bachman, J. S. Elias, C.-J. Sun, Y. Shao-Horn, M. Dincă, *Nat. Mater.* **2016**, *16*, 220.

[10] P. Simon, Y. Gogotsi, *Nat. Mater.* **2008**, *7*, 845.

[11] S. Kondrat, C. R. Perez, V. Presser, Y. Gogotsi, A. A. Kornyshev, *Energy Environ. Sci.* **2012**, *5*, 6474.

[12] J. Liu, D. Zhu, C. Guo, A. Vasileff, S.-Z. Qiao, *Adv. Energy Mater.* **2017**, *7*, 1700518.

[13] Y. Deng, Y. Xie, K. Zou, X. Ji, *J. Mater. Chem. A* **2016**, *4*, 1144.

[14] X. Fan, C. Yu, J. Yang, Z. Ling, J. Qiu, *Carbon* **2014**, *70*, 130.

[15] M. Mousavi-Khoshdel, E. Targholi, M. J. Momeni, *J. Phys. Chem. C* **2015**, *119*, 26290.

[16] G. Feng, P. T. Cummings, *J. Phys. Chem. Lett.* **2011**, *2*, 2859.

[17] D.-E. Jiang, Z. Jin, J. Wu, *Nano Lett.* **2011**, *11*, 5373.

[18] E. Raymundo-Piñero, K. Kierzek, J. Machnikowski, F. Béguin,

*Carbon* **2006**, *44*, 2498.

[19] J. Chmiola, G. Yushin, Y. Gogotsi, C. Portet, P. Simon, P. L. Taberna, *Science* **2006**, *313*, 1760.

[20] J. Lee, S. Yoon, T. Hyeon, S. M. Oh, K. B. Kim, *Chem. Commun.* **1999**, 2177.

[21] M. Zhi, F. Yang, F. Meng, M. Li, A. Manivannan, N. Wu, *ACS Sustainable Chem. Eng.* **2014**, *2*, 1592.

[22] N. Jäckel, P. Simon, Y. Gogotsi, V. Presser, *ACS Energy Lett.* **2016**, *1*, 1262.

[23] Z.-S. Wu, A. Winter, L. Chen, Y. Sun, A. Turchanin, X. Feng, K. Müllen, *Adv. Mater.* **2012**, *24*, 5130.

[24] J. Wei, C. Yin, H. Wang, Q. Wang, *J. Mater. Chem. A* **2018**, *6*, 58.

[25] J. Qu, C. Geng, S. Lv, G. Shao, S. Ma, M. Wu, *Electrochim. Acta* **2015**, *176*, 982.

[26] M. Li, J. Xue, *J. Phys. Chem. C* **2014**, *118*, 2507.

[27] L.-F. Chen, X.-D. Zhang, H.-W. Liang, M. Kong, Q.-F. Guan, P. Chen, Z.-Y. Wu, S.-H. Yu, *ACS Nano* **2012**, *6*, 7092.

# Bibliography

## 1. International Publications from SNU

### First Author Papers


1) **Vinayak S. Kale**(*co-first author*)[$], Uk Sim[$], Jiwoong Yang, Kyoungsuk Jin, Sue In Chae, Woo Je Chang, Arun Kumar Sinha, Heonjin Ha, Chan-Cuk Hwang, Junghyun An, Hyo-Ki Hong, Zonghoon Lee, Ki Tae Nam*, and Taeghwan Hyeon*

"Sulfur-Modified Graphitic Carbon Nitride Nanostructures as an Efficient Electrocatalyst for Water Oxidation"

*Small*, **2017**, *13(17)*, 1603893

2) **Vinayak S. Kale**(*co-first author*)[$], Minsik Hwang[$], Hogeun Chang, Jeongmin Kang, Sue In Chae, Youngmoo Jeon, Jiwoong Yang, Jonghoon Kim, Yoon-Joo Ko, Yuanzhe Piao*, and Taeghwan Hyeon*

""Microporosity-Controlled Synthesis of Heteroatom Co-doped Carbon Nanocages by Wrap-Bake-Sublime Approach for Flexible All-Solid-State-Supercapacitors"

*Advanced Functional Materials*, **2018**, just accepted

## 2. Co-author Papers

3) Jiwoong Yang, Franziska Muckel, B.-K. Choi, S. Lorenz, I.-Y. Kim, J. Ackermann, H. Chang, T. Priesner, **Vinayak S. Kale**, Seong-Ju Hwang, Gerd Bacher*, Taeghwan Hyeon*

"$Co^{2+}$-Doping of Magic-Sized CdSe Clusters: Structural Insights via Ligand Field Transitions"

*Nano Letters*, Under revision

4) Moon Kee Choi, Jiwoong Yang, Dong Chan Kim, Zhaohe Dai, Junhee Kim, Hyojin Seung, **Vinayak S. Kale**, Sae Jin Sung, Chong Rae Park, Nanshu Lu, Taeghwan Hyeon*, and Dae-Hyeong Kim*

"Extremely Vivid, Highly Transparent, and Ultrathin Quantum Dot Light-Emitting Diodes"

*Advanced Materials*, **2018**, *30(1)*, 1703279

5) Donghee Son, Sue In Chae, Myungbin Kim, Moon Kee Choi, Jiwoong Yang, Kunsu Park, **Vinayak S. Kale**, Ja Hoon Koo, Changsoon Choi, Minbaek Lee, Ji Hoon Kim, Taeghwan Hyeon*, and Dae-Hyeong Kim*

"Colloidal Synthesis of Uniform-Sized Molybdenum Disulfide

Nanosheets for Wafer-Scale Flexible Nonvolatile Memory"

*Advanced Materials*, **2016**, *28(42)*, 9326-9332

## 2. International Publications other than SNU

### First Author Papers

1) **Vinayak S. Kale**, Rajiv Ramanujam Prabhakar, Stevin S. Pramana, Manohar Rao, Chorng-Haur Sow, K. B. Jinesh*, and Subodh G Mhaisalkar

"Enhanced Electron Field Emission Properties of High Aspect Ratio Silicon Nanowire-Zinc Oxide Core-Shell Arrays"

*Physical Chemistry Chemical Physics,* **2012***, 14(13),* 4614-4619

2) **Vinayak S. Kale**, B. R. Sathe, Ajay Kushwaha, Mohammed Aslam, and Manjusha V. Shelke*

"A Novel Catalyst-free Synthesis of Vertically Aligned Silicon Nanowire-Carbon Nanotube Heterojunction Arrays for High Performance Electron Field Emitters"

*Chemical Communications,* **2011***, 47(27),* 7785-7787

### Co-author Papers

3) V. Aravindan*, K. B. Jinesh, Rajiv Ramanujam Prabhakar, **Vinayak S. Kale**, and S. Madhavi*

"Atomic Layer Deposited (ALD) $SnO_2$ Anodes with Exceptional Cycleability for Li-ion Batteries"

*Nano Energy,* **2013***, 2(5),* 720-725

4) Phong D. Tran*, Stevin S. Pramana, **Vinayak S. Kale**, Mai Nguyen, Sing Yang Chiam, Sudip K. Batabyal, Lydia H. Wong*, James Barber, and Joachim Loo*

"Novel Assembly of an $MoS_2$ Electrocatalyst onto a Silicon Nanowire Array Electrode to Construct a Photocathode Composed of Elements Abundant on the Earth for Hydrogen Generation"

*Chemistry - A European Journal,* **2012***, 18(44),* 13994-13999

5) Manash R. Das*, Rupak K. Sarma, Ratul Saikia, **Vinayak S. Kale**, Manjusha V. Shelke, and Pinaki Sengupta

"Synthesis of Silver Nanoparticles in an Aqueous Suspension of Graphene Oxide Sheets and its Antimicrobial Activity"

*Colloids and Surfaces B: Biointerfaces,* **2011***, 83(1),* 16-22

6) Ashvini B. Deshmukh, **Vinayak S. Kale**, Vishal M. Dhavale, K. Sreekumar, K. Vijayamohanan, and Manjusha V. Shelke*

"Direct Transfer of Micro-Molded Electrodes for Enhanced Mass Transport and Water Management in PEMFC"

*Electrochemistry Communications,* **2010***, 12(11),* 1638-1641

7) Santosh L Hire, Manjusha V. Shelke*, **Vinayak S. Kale**, Elisabeth Galopin, Mohan G. Kulkarni, Rabah Boukherroub, and Satishchandra B. Ogale*

"Template Assisted Highly Ordered Novel Self-Assembly of Micro-Reservoirs and its Replication"

*Lab on a Chip,* **2010***, 10(15),* 1092-1906

8) B. K. Balan, **Vinayak S. Kale**, Pradnya P. Aher, Manjusha V. Shelke, Vijayamohanan K. Pillai, and Sreekumar Kurungot*

"High Aspect Ratio Nanoscale Multifunctional Materials Derived from Hollow Carbon Nanofiber by Polymer Insertion and Metal Decoration"

*Chemical Communications,* **2010***, 46(30),* 5590-5592

## 3. Conferences/Presentations/Symposiums from SNU

### International Conferences

1) “Materials Research Society (MRS), Fall 2015 Meeting, Boston, Massachusetts, USA – 29 Nov - 4 Dec 2015”

   POSTER PRESENTATION

**Conferences in South Korea**

2) “2018 KSIEC Spring Meeting – The Korean Society of Industrial and Engineering Chemistry, Daegu, South Korea – 2 - 4 May 2018”

   POSTER PRESENTATION

3) “NANO KOREA 2017 The 15$^{th}$ International Nanotech Symposium and Nano-Convergence Expo Coex, Seoul, South Korea – 12 - 14 Jul 2017”

   ORAL PRESENTATION

4) “The 9$^{th}$ International Conference on Quantum Dots, Jeju, South Korea – 22 - 27 May 2016”

   POSTER PRESENTATION

5) “18$^{th}$ Topical Meeting of The International Society of Electrochemistry, Gwangju, South Korea – 8 - 11 Mar 2016”

   POSTER PRESENTATION

**4. Conferences/Presentations/Symposiums before SNU**

**International Conferences**

6) "ICYRAM 2012 Singapore International Conference of Young Researchers on Adv. Mater. Singapore – 1 - 6 Jul 2012"

   POSTER PRESENTATION

**Conferences in India**

7) "12$^{th}$ CRSI National Symposium in Chemistry and 4$^{th}$ CRSI-RSC Symposium in Chemistry, Indian Institute of Chemical Technology (IICT) and National Institute of Pharmaceutical and Research (NIPER), Hyderabad, India – 4 - 7 Feb 2010"

   POSTER PRESENTATION

8) "International Conference on Materials for the Millennium, MatCon 2010, Cochin University of Science and Technology (CUSAT), Kerala, India – 11 - 13 Jan 2010"

   POSTER PRESENTATION

9) "Indo-German Workshop on Micro-reaction Technology, National

Chemical Laboratory (NCL) Pune, India – 4 - 5 Mar 2009”

POSTER PRESENTATION

# 초 록

탄소 물질은 가격 경쟁력, 쉬운 합성법, 환경 친화성 때문에 기존에 사용되는 금속/금속 산화물의 대안으로 주목을 받고 있다. 탄소 물질은 나노 규모에서 다양한 크기, 모양, 차원을 갖도록 합성함으로써 그 성질을 조절할 수 있다. 더욱이 질소, 인, 황, 붕소와 같은 이원자를 갖도록 탄소 물질을 변형하면 새로운 기능을 더하고, 전하를 재분배하며 새로운 에너지 상태를 도입하여 탄소물질의 성질을 현저히 개선시킨다. 이러한 변형은 도핑 과정, 탄소 물질 내의 이원자 치환 또는 교체를 통해 일어난다. 더욱이, 하나 이상의 이원자가 개질된 탄소 물질은 단일체보다 그 특성을 향상시키는 시너지 효과를 나타낸다. 이원자로 개질된 탄소 나노 물질은 많은 응용 분야에서 잘 정립된 금속/금속 산화물과 비교하여 우수한 성능을 나타낸다. 도입부인 제 1 장에서는 탄소 나노 물질의 이원자-변형을 위해 개발된 다양한 합성 전략을 논의하였다.

제 2 장에서는 황-개질된 그래피틱 카본나이트라이드 나노 구조의 합성에 대해 설명하였다. 자연 정동석에 의해 영감을 얻은 독특한 멜라민 나노 입자를 열수 과정으로 합성하였다. 멜라민 나노 입자와 황의 in-situ 혼합 및 열분해를 통해

황-개질된 그래피틱 카본 나이트라이드 (S-modified g-$CN_x$) 나노 구조가 생성되었다. S-modified g-$CN_x$는 물 산화 전극 촉매로 적용 할 경우, 보고된 금속/금속 산화물 및 잘 정립 된 전극 촉매와 비교할 수 있는 탄소 기반 시스템 중에서 가장 우수한 산소 발생 반응 (OER) 활성을 나타내었다. g-$CN_x$ 구조의 황 개질은 OER에 대한 활성화 에너지의 최소화로 인해 과전압을 낮추었다.

제 3 장에서 질소, 인 (N, P)이 동시에 도핑된 탄소 나노 케이지 (NPHC)의 그램 규모 합성을 위한 wrap-bake-sublime 접근법 개발에 대해 논의하였다. 아연을 함유한 Zeolitic-imidazole-framework (ZIF-8) 나노 입자를 코어로 사용하여 N, P를 포함하고 있는 올리고머인 oligo(cyclotriphosphazene-co-hexahydroxytriphenylene) (OCHT)로 감쌌다. 이 ZIF-8@OCHT 나노 입자의 열분해는 아연을 승화시키고 합성된 NPHC에 다공성을 도입시켰다. NPHC의 미세 다공성은 ZIF-8@OCHT 나노 입자의 합성 과정에서 OCHT 껍질의 두께를 조절한 후 열분해함으로써 정밀하게 조절할 수 있었다. 수퍼 커패시터의 전극으로 미세기공 크기 의존 NPHCs의 응용은 NPHCs의 전기 화학적 성능과 미세 다공성 사이의 우수한 상관 관계가 있습니다.

또한, 전기 화학적 성능은 NPHC에서의 이원자 도핑량 사이의 비와 상관 관계가 있었다. 마지막으로, 대칭적이고 유연한 all-solid-state-수퍼 커패시터를 제작하였으며, 75%의 용량 유지율로 20,000 사이클 동안 높은 에너지 밀도, 전력 밀도 및 우수한 장기 안정성을 보였다.

**주요어:** 이원자, 개질, 도핑, 흑연 그래피틱 카본나이트라이드, 탄소 나노 케이지, 물 산화, 수퍼 커패시터

**학 번:** 2012-31295